AFRL-RX-WP-TR-2022-0037

DAMAGE PROGRESSION IN GENERIC CERAMIC MATRIX COMPOSITE TURBINE AIRFOILS

Larry Zawada
ARCTOS

Eric Jones
AFRL/RXCA

George Jefferson
AFRL/RXCC

Travis Whitlow
Jennifer Pierce
University of Dayton Research Institute

31 JANUARY 2022
Final Report

DISTRIBUTION STATEMENT A.
Approved for public release: distribution is unlimited.

AIR FORCE RESEARCH LABORATORY
MATERIALS AND MANUFACTURING DIRECTORATE
WRIGHT-PATTERSON AIR FORCE BASE, OH 45433-7750
AIR FORCE MATERIEL COMMAND
UNITED STATES AIR FORCE

NOTICE AND SIGNATURE PAGE

AFRL-RX-WP-TR-2022-0037 HAS BEEN REVIEWED AND IS APPROVED FOR PUBLICATION IN ACCORDANCE WITH ASSIGNED DISTRIBUTION STATEMENT.

PRZYBYLA.CRAIG.P.1178234257 Digitally signed by PRZYBYLA.CRAIG.P.1178234257 Date: 2022.02.24 10:04:12 -05'00'	ROGERS.BRET.ZACHARY.1265647924 Digitally signed by ROGERS.BRET.ZACHARY.1265647924 Date: 2022.02.24 12:00:49 -05'00'
CRAIG PRZYBYLA Project Engineer Composite Branch Structural Materials Division Materials and Manufacturing Directorate	BRET ROGERS Section Chief Composite Branch Structural Materials Division Materials and Manufacturing Directorate

REPORT DOCUMENTATION PAGE

PLEASE DO NOT RETURN YOUR FORM TO THE ABOVE ORGANIZATION.

1. REPORT DATE
31 January 2022

2. REPORT TYPE
Final

3. DATES COVERED

START DATE
4 April 2013

END DATE
31 December 2018

4. TITLE AND SUBTITLE
DAMAGE PROGRESSION IN GENERIC CERAMIC MATRIX COMPOSITE TURBINE AIRFOILS

5a. CONTRACT NUMBER
In-House

5b. GRANT NUMBER

5c. PROGRAM ELEMENT NUMBER
62102F

5d. PROJECT NUMBER
4347

5e. TASK NUMBER

5f. WORK UNIT NUMBER
X1Z0

6. AUTHOR(S)

Larry Zawada – Arctos
Eric Jones – AFRL/RXCA
George Jefferson – AFRL/RXCC
Jennifer L. Pierce – UDRI
Travis Witlow – UDRI

7. PERFORMING ORGANIZATION NAME(S) AND ADDRESS(ES)

- Universal Technology Corporation, Dayton Ohio 45432
- AFRL/RXCC, Wright-Patterson AFB, OH 45433
- University of Dayton Research Institute, 300 College Park, Dayton, OH 45469

8. PERFORMING ORGANIZATION REPORT NUMBER

9. SPONSORING/MONITORING AGENCY NAME(S) AND ADDRESS(ES)

Air Force Research Laboratory
Materials and Manufacturing Directorate
Wright-Patterson Air Force Base, OH 45433-7750
Air Force Materiel Command

10. SPONSOR/MONITOR'S ACRONYM(S)
AFRL/RXCCP

11. SPONSOR/MONITOR'S REPORT NUMBER(S)
AFRL-RX-WP-TR-2022-0037

12. DISTRIBUTION/AVAILABILITY STATEMENT
DISTRIBUTION STATEMENT A. Approved for public release: distribution is unlimited.

13. SUPPLEMENTARY NOTES
PA Case Number: AFRL-2022-0787; Clearance Date: 22 February 2022

14. ABSTRACT

A dedicated experimental test program was conducted to characterize the development of damage in generic airfoils manufactured using ceramic matrix composites and to compare those results to FEA predictions. This report describes test results for interlaminar tension, tensile in-plane shear, tensile, fatigue, creep rupture, and subelement testing.

15. SUBJECT TERMS
Silicon Melt Infiltrated, SiC/SiC, Tension, Fatigue, Interlaminar Tension, Interlaminar Shear, Airfoil, Dovetail

16. SECURITY CLASSIFICATION OF:

a. REPORT
Unclassified

b. ABSTRACT
Unclassified

C. THIS PAGE
Unclassified

17. LIMITATION OF ABSTRACT
SAR

18. NUMBER OF PAGES
116

19a. NAME OF RESPONSIBLE PERSON
George Jefferson

19b. PHONE NUMBER *(Include area code)*
(937) 785-1307

TABLE OF CONTENTS

LIST OF FIGURES iii
LIST OF TABLES viii
ABSTRACT ix
1. SUMMARY 1
2. INTRODUCTION 2
  2.1 Background 2
3. MATERIALS DESCRIPTION 6
  3.1 Description of CMC Test Material 6
  3.2 Manufacturing And Inspection Of Flat Panel Material 7
  3.3 Microstructure Studies of CMC 8
  3.4 NDI of Test Specimens From Flat Panel 10
  3.5 NDI of Subelement Panel 12
4. TEST METHODOLOGY AND PROCEDURE 13
  4.1 Test Procedures 13
    4.1.1 Servo-Hydraulic Test Frame 13
    4.1.2 Burner Rig 13
    4.1.3 Burner Rig Temperature Calibration 16
    4.1.4 Burner Rig Heat Flux Calibration Using a Calorimeter 17
    4.1.5 Grip Design For Subelement 21
    4.1.6 Alignment of Gripping Fixture And Load Train 24
    4.1.7 Digital Image Correlation 25
    4.1.8 Acoustic Emission 26
    4.1.9 X-Ray Computed Tomography 27
    4.1.10 Optical Microscopy of Subelement Test Specimen 28
  4.2 Flat Panel Test Matrix 29
  4.3 Flat Panel Specimen Designs 29
  4.4 Test Matrix For Subelements 32
  4.5 Design of Subelement Test Specimen 34
  4.6 Manufacturing Of Subelement Test Specimens 43
5. TEST RESULTS 46
  5.1 Baseline Test Results 46
    5.1.1 DNC 46

5.1.2 ILT 47
5.1.3 Tension 49
5.1.4 Creep Rupture Testing In A Furnace 50
5.1.5 Microscopy of Fracture Surfaces 51
5.2 Subelement Test Results 55
5.2.1 Subelement Tension Test at 23°C (15-543) 55
5.2.2 Subelement Stepped Tension Test at 23°C (15-542) 64
5.2.3 Subelement Stepped Fatigue at 23°C (15-544) 73
5.2.4 Subelement Fatigue at 23°C & 200 MPa (15-545) 81
5.2.5 Subelement Fatigue at 23°C and 210 MPa (15-545a) 83
5.2.6 Subelement Fatigue At 23°C & 200 MPa (15-548) 86
5.2.7 Subelement Stepped Fatigue At 23°C (15-548a) 86
5.2.8 Subelement Fatigue At 23°C & 200 MPa (15-550) 86
5.2.9 Subelement Burner Rig At 800°C & 200 MPa (15-547) 86
5.2.10 Subelement Burner Rig At 600°C & 200 MPa (15-546) 86
5.2.11 Subelement Burner Rig At 600°C & 175 MPa (15-549) 90
5.2.12 Subelement Burner Rig At 1000°C & 175 MPa (15-541) 94
6.0 CONCLUSIONS AND OBSERVATIONS 99
7.0 REFERENCES 103
LIST OF SYMBOLS, ABBREVIATIONS, AND ACRONYMS 104

LIST OF FIGURES

Figure **Page**

Figure 1. Photograph GE Aviation Jet Engine Turbine Blade Made From CMCs (2015 Paris Air Show) 2

Figure 2. Photograph OF CMC Low Pressure Turbine Blades In An F414 Engine 3

Figure 3. Photograph Of Prototype CMC Turbine Blade By SNECMA 3

Figure 4. Previous Studies Of CMC Airfoil Attachments 5

Figure 5. Low Magnification Image of SMI SiC/SiC Showing Large Pores 6

Figure 6. Intermediate Magnification Image of SMI SiC/SiC Showing Large Pores 6

Figure 7. High Magnification Image of SMI SiC/SiC Showing Pores Within Fiber Tows 7

Figure 8. Thermography Scan of SMI SiC/SiC Panel At 0.1 Second 8

Figure 9: Example of VF: Green = Fiber, Yellow = CVI, Red = Matrix, Blue = Inter-tow Porosity, Orange = Intra-tow Porosity 9

Figure 10. Thermography Scan Of Dogbone Test Specimen 11

Figure 11. Thermography Scan Of Double Notch Compression Test Specimen 11

Figure 12. Thermography Scan Of ILT Test Specimen 12

Figure 13. Optical Photographs Of The Highly Instrumented Test Set Up for Subelements 13

Figure 14. Photograph Of Burner Rig Test Frame 14

Figure 15. Expanded View Of Subelement In Burner Rig 15

Figure 16. Photograph Of Burner Rig Showing the HVOF Gun In Operation Heating A CMC Subelement Test Specimen 15

Figure 17. Close-up Photograph Of A Subelement Test Specimen Being Heated In Burner Rig 16

Figure 18. Image From FLIR Camera Of CMC Test Specimen At 1300°C 17

Figure 19. Schematic Of Calorimeter Used to Measure Heat Flux 18

Figure 20. Optical Photograph Of Calorimeter Used To Measure Heat Flux 18

Figure 21. Optical Photograph of Calorimeter In the Burner Rig During Calibration of Heat Flux. 19

Figure 22. Heat Flux Shows a Exponential Relationship With Position Of The HVOF Gun Nozzle 20

Figure 23. Heat Flux Versus SMI SiC/SiC Specimen Surface Temperature 21

Figure 24. A Machining Drawing For The Subelement Test Specimen (mm) 22

Figure 25. Angles Were Measured On Each Subelement Test Specimen 22

Figure 26. Schematic OF Wedge Grip Insert Used To Grip Subelement 23

Figure 27. Photograph Of Wedge Grip Insert Used To Grip Subelement 24
Figure 28. Subelement alignment specimen with strain gages. 24
Figure 29. DIC Image Of Dovetail Section of Subelement With DIC Speckle Pattern 26
Figure 30. a) Photo Showing Focus Areas of The CT Scan, b) Example Slice From The Y-X Orientation, and c) Example Slice From The Z-X Orientation 28
Figure 31. Machining Drawing For Flat Panel of SMI SiC/SiC 30
Figure 32. Machining Drawing For Interlaminar Tension Specimen 30
Figure 33. Photograph of Interlaminar Tension Specimen 31
Figure 34. Machining Drawing For Double Notch Compression Test Specimen 31
Figure 35. Photograph of Double Notch Compression Test Specimen 31
Figure 36. Machining Drawing For Dogbone Specimen Used For Tension and Creep Rupture Testing 32
Figure 37. Photograph of Dogbone Specimen Used For Tension and Creep Rupture Testing ... 32
Figure 38. Finite Element Analysis Mesh Used To Analyze Subelement Test Specimen 35
Figure 39. Schematic Of Dovetail Section of Subelement Test Specimen 35
Figure 40. Schematic Showing Orientation of ILT Stresses (σ_{zz}) 36
Figure 41. Schematic Showing Orientation of In-Plane Stresses (σ_{xx}) 36
Figure 42. ILT Stress (σ_{11}) for a 20° Dovetail Angle And Various Transition Radii 37
Figure 43. In-Plane Stress (σ_{22}) for a 20° Dovetail Angle And Various Transition Radii 37
Figure 44. Interlaminar Tensile Stress (σ_{11}) for Increase Dovetail Angle With Constant Transition radius of R0.75 38
Figure 45. Interlaminar Tensile Stress (S11) For a 30° Dovetail Angle With Various Radii 38
Figure 46. Schematic Drawing of Dovetail Attachment Region Of Subelement Test Specimen 40
Figure 47. Machining Drawing Of Subelement Test Specimen 40
Figure 48. In Plane Tension Stress (σ_{11}) For Subelement Test Specimen 41
Figure 49. Interlaminar Shear Stress (σ_{13}) For Subelement Test Specimen 41
Figure 50. Plot of Interlaminar Shear Stress (σ_{13}) As A Function of Applied Load 42
Figure 51. Interlaminar Tension Stress (σ_{33}) For Subelement Test Specimen 42
Figure 52. Plot of Interlaminar Tensile Stress (σ_{33}) As A Function of Applied Load 43
Figure 53. Schematic Diagram Of How Subelement Panel Was Constructed 44
Figure 54. Schematic Showing How Dovetail of Subelement Test Specimen Was Constructed And Machined 44

Figure 55. Optical Image of Dovetail Section Of Subelement Test Specimen 45

Figure 56. Optical Photograph Of An As-manufactured Subelement Test Specimen 45

Figure 57. Stress Versus Time For A Room Temperature Double-Notch Compression Test On SMI SiC/SiC 46

Figure 58. DIC Strain Maps for DNC Test on SMI SiC/SiC... 47

Figure 59. CMCs Exhibit a 3:1 Ratio of ILS to ILT Strength [14] 48

Figure 60. Photograph of Test Set-up For Room Temperature ILT Test on SMI SiC/SiC.......... 49

Figure 61. Tensile Behavior of SMI SiC/SiC At Three Temperatures....................................... 50

Figure 62. Creep strain vs time for SMI-SiC/SiC made by RRHTC... 51

Figure 63. Stress-Strain Behavior for Loading Portion Of The Creep Rupture Test Compared to Monotonic Tensile Test For SMI SiC/SiC at 1200°C 51

Figure 64. Photographs of Failed SMI-SiC/SiC Test Specimens: a) Tension Tested at 800°C, b) Tension Tested at 1200°C, and c) Creep Tested at 1200°C.. 52

Figure 65. Optical Photographs of Specimen Fractures: a) Tension Tested at 800°C, b) Tension Tested at 1200°C, and c) Creep Tested at 1200°C... 53

Figure 66. SEM Images of Fracture Surfaces for 1200°C Tensile (a) & c)) And Creep (b) & d)) Tested Specimens of SMI-SiC/SiC 54

Figure 67. Temperature Profiles Measured on a SMI-SiC/SiC Dogbone Specimen At 800°C and 1200°C 55

Figure 68. Optical Image Of The Dovetail Edge Of Specimen 15-453...................................... 56

Figure 69. CT Image Of The Dovetail Interior Of Specimen 15-543 56

Figure 70. Tensile Behavior Of A Dogbone And Subelement at 23°C....................................... 57

Figure 71. DIC Strain Map of Subelement Tensile Test Taken at 120 MPa.............................. 58

Figure 72. DIC Strain Map of Subelement Tensile Test Taken at 160 MPa.............................. 59

Figure 73. DIC Strain Map of Subelement Tensile Test Taken at 200 MPa.............................. 59

Figure 74. DIC Strain Map of Subelement Tensile Taken at 220 MPa...................................... 60

Figure 75. DIC Strain Map of Subelement Tensile Test Taken at 240 MPa.............................. 60

Figure 76. DIC Strain Map of Subelement Tensile Test Taken at 263 MPa.............................. 61

Figure 77. a) Instrumented Subelement With Three AE sensors b) Location Density Plot Highlighting Regions of Localized Crack Growth c) Cumulative AE Curve Used to Estimate the Matrix Cracking Stress... 61

Figure 78. Photograph of Failed Subelement Tension Test Specimen (15-543)......................... 62

Figure 79. Micrograph of Polished Dovetail Edge of Subelement Tension Tested, With Cracks Highlighted In Red (15-543.. 63

Figure 80. Optical Micrograph Of Dovetail Edge Of Stepped Tension Specimen 15-542......... 64

Figure 81. CT Scan of Dovetail Region OF Stepped Tension Specimen 15-542........................ 64
Figure 82. Schematic Of Loading Sequence Used For Stepped Tension Test Of Subelement... 65
Figure 83. Stress-Strain Traces For Stepped Tensile Test Of Subelement (15-542)................... 66
Figure 84. Stress-Strain Traces and DIC Strain For Stepped Tensile: Cycle 9 (230 MPa)......... 67
Figure 85. Stress-Strain Traces and DIC Strain For Stepped Tensile: Cycle 9 (240 MPa)......... 67
Figure 86. Stress-Strain Traces and DIC Strain For Stepped Tensile: Cycle 9 (250 MPa)......... 68
Figure 87. Stress-Strain Traces and DIC Strain For Stepped Tensile: Cycle 10 (110 MPa)....... 69
Figure 88. Stress-Strain Traces and DIC Strain For Stepped Tensile: Cycle 10 (160 MPa)....... 69
Figure 89. Stress-Strain Traces and DIC Strain For Stepped Tensile: Cycle 10 (210 MPa)....... 70
Figure 90. Stress-Strain Traces And DIC Strain For Stepped Tensile: Cycle 10 (246 MPa)...... 70
Figure 91. DIC Strain Map For Stepped Tension At 246 MPa (15-542) 71
Figure 92. Cumulative AE Energy Plot for Stepped Tensile Cycles 2-10................................... 71
Figure 93. Optical Photographs Of Failed Stepped Tension Specimen (15-542)........................ 72
Figure 94. Micrograph Of Failed Stepped Subelement Tension Test (15-542) 73
Figure 95. Schematic Showing Sequential Loading Blocks For Stepped Fatigue 74
Figure 96. DIC Images For Stepped Fatigue at 200 MPa 15-544)).. 74
Figure 97. DIC Images For Stepped Fatigue at 225 MPa (15-544).. 75
Figure 98. AE Events For The Stepped Fatigue Test 76
Figure 99. Cumulative AE Events Versus Number of Total Fatigue Cycles 76
Figure 100. Length of Visual Cracks (From DIC) Versus Number Of Fatigue Cycles 77
Figure 101. CT Image of Failed Stepped Fatigue Subelement (15-544)...................................... 77
Figure 102. Photographs of Failed Subelement From Stepped Fatigue (15-544) 79
Figure 103. Photographs of Failed Subelement Dovetail Section For Stepped Fatigue (15-544) 79
Figure 104. Microscopy of Failed Subelement Stepped Fatigue Test At Surface And Center Of Dovetail (15-544).. 80
Figure 105. Diagram Demonstrating That ILT Predictions Match Location of ILT Induced Cracks Identified by DIC and Microscopy 81
Figure 106. Modulus and % Strain Versus Cycles For A Fatigue Test of Subelement Tested at 200 MPa (15-545) 82
Figure 107. DIC Strain Maps At 200 MPa and 1, 1001, and 5001 Cycles (15-545)................... 82
Figure 108. DIC Strain Maps At 200 MPa and 1, 1001, and 5001 Cycles (15-545)................... 83
Figure 109. DIC Strain Maps At 200 MPa and 10,000, 152,000, and 302,005 Cycles (15-545) 83

Figure 110. DIC Strain Maps At 210 MPa and Total Cycle Count Of 312,000 Cycles (15-545a) 84

Figure 111. Cumulative AE Events For Fatigue Test of Subelement (15-545a)........ 84

Figure 112. Damage Length vs Cycles For Subelement Fatigue Test (15-545a)........ 85

Figure 113. Micrograph of Polished Edge of Subelement 15-545a Fatigued at 23°C and 210 MPa, With Cracks Highlighted in White........ 85

Figure 114. Photograph Of Failed Subelement Stem And Dovetail For Burner Rig Tested at 600°C And 200 MPa (15-546)........ 88

Figure 115. Photograph Of Failed Subelement Burner Rig Tested at 600°C And 200 MPa (15-546)........ 89

Figure 116. Micrograph of Polished Surface Edge Micrograph Of Subelement Burner Rig Tested at 600°C And 200 MPa (15-546) 90

Figure 117. Micrograph Of Polished Center Section Of Subelement Burner Rig Tested at 600°C And 200 MPa (15-546)........ 90

Figure 118. Stress-Strain Trace And DIC Strain Map For Prior Exposed Burner Rig Exposed Subelement At A Stress of 75 MPa (15-549)........ 91

Figure 119. Stress-Strain Trace And DIC Strain Map For Prior Exposed Burner Rig Exposed Subelement At A Stress of 100 MPa (15-549)........ 92

Figure 120. Stress-Strain Trace And DIC Strain Map For Prior Exposed Burner Rig Exposed Subelement At A Stress of 125 MPa (15-549)........ 92

Figure 121. Stress-Strain Trace And DIC Strain Map For Prior Exposed Burner Rig Exposed Subelement At A Stress of 75 MPa (15-549)........ 93

Figure 122. Stress-Strain Trace And DIC Strain Map For Prior Exposed Burner Rig Exposed Subelement At A Stress of 175 MPa (15-549)........ 93

Figure 123. Stress-Strain Trace And DIC Strain Map For Prior Exposed Burner Rig Exposed Subelement At A Stress of 75 MPa (15-541)........ 94

Figure 124. Stress-Strain Trace And DIC Strain Map For Prior Exposed Burner Rig Exposed Subelement At A Stress of 100 MPa (15-541)........ 95

Figure 125. Stress-Strain Trace And DIC Strain Map For Prior Exposed Burner Rig Exposed Subelement At A Stress of 125 MPa (15-541)........ 95

Figure 126. Stress-Strain Trace And DIC Strain Map For Prior Exposed Burner Rig Exposed Subelement At A Stress of 150 MPa (15-541)........ 96

Figure 127. Stress-Strain Trace And DIC Strain Map For Prior Exposed Burner Rig Exposed Subelement At A Stress of 175 MPa (15-541)........ 96

Figure 128. Comparison Of Damage Length In Dovetail Versus Applied Stress For The 23°C Tension Test And The Burn Rig Loaded To 175 MPa At 1000°C. 97

Figure 129. Polished Cross-Section of Burner Rig Specimen Tested At 1000°C and 175 MPa For One Cycle (15-541) 98

LIST OF TABLES

Table **Page**

Table 1: Estimated Constitute Volume Fractions 9

Table 2: Porosity Volume Fraction For Dogbone Study 9

Table 3: Matrix Volume Fraction For Dogbone Study... 10

Table 4: Overall Constituent Volume Fraction For Subelement Study........................ 10

Table 5: Porosity Volume Fraction For Subelement Study... 10

Table 6: Matrix Volume Fraction For Subelement Study 10

Table 7. Thermogage 1000-30 Calibration Values.. 19

Table 8. CMC Temperature, Corresponding Heat Flux, And Distance of HVOF Gun From CMC.. 20

Table 9. Baseline Property Test Matrix 29

Table 10. Subelement Test Matrix.. 33

Table 11. Results of Parametric Study of Subelement Test Specimen Design 39

Table 12. Results From the DNC Tests On SMI SiC/SiC 46

Table 13. Results From The ILT tests 47

Table 14. Tensile Properties for SMI SiC/SiC.. 50

ABSTRACT

The work described in this report was performed by the Composite Performance Research Team of the Composites Branch, Structural Materials Division of the Materials & Manufacturing Directorate, Air Force Research Laboratory (AFRL/RXCC). Eric Jones was the principal investigator and program manager. This report describes the results of a study focused on identification of testing variables, test specimen geometry, and environmental effects on the performance of generic airfoil shapes made out of ceramic matrix composites. The objective was to compare testing results to FEA analysis and to generate urgently needed test data for the CMC Lifing community. The in-house testing was performed under contract with the University of Dayton Research Institute (UDRI). Jennifer Pierce was the lead engineer with UDRI and responsible for all in-house experiments.

1. SUMMARY

USAF researchers in AFRL/RXCCP (Composites Performance Research Team) implemented advanced materials characterization methods on a slurry melt-infiltrated SiC/SiC CMC. Using a building block approach, standard flat test specimens were tested at room and elevated temperature to document material properties and to provide needed input for Finite Element Analysis. This baseline testing was followed by FEA analysis and design of a generic shape of the dovetail attachment region of an aerospace turbine engine low pressure turbine blade. In this report the generic shape will be referred to as a subelement test specimen. Information-rich experiments were performed at room temperature, as well as under realistic service conditions in a burner rig at the Air Force Institute of Technology (AFIT). The objective was to identify how damage develops in CMC airfoil dovetail attachment regions and under what loading conditions damage either stabilizes or continues to develop and grow

2. INTRODUCTION

2.1 Background

Over the last decade major advances have been made in advancing the state-of-the-art in ceramic matrix composites (CMCs) for use in aerospace turbine engines. The first commercial CMC components to enter service were shrouds in the LEAP engine on the Boeing 737 MAX Airbus A320neo and Airbus A321neo jets.[1] The LEAP's maker is CFM International, which is a 50/50 joint venture between GE Aviation and Safran Aircraft Engines of France. They have received more than 10,800 orders and commitments for the engines valued at more than $150 billion. [1]

The next step will be to introduce CMCs into rotating aerospace turbine engine components such as low pressure turbine blades. GE Aviation is actively pursuing these components. In 2015 GEA unveiled a CMC turbine blade at the Paris Air Show. A photograph of that CMC turbine blade is presented in Figure 1. This is an example of a fully functional CMC turbine blade with a dovetail attachment arrangement and integral platforms. GEA has also successfully engine tested a complete set of solid CMC low pressure turbine blades in an F414 engine as shown in Figure 2. In addition, IHI in Japan has been actively researching CMC airfoils since 2005. An example of one of their CMC airfoils is presented in Figure 3.[3,4]

Figure 1. Photograph GE Aviation Jet Engine Turbine Blade Made From CMCs (2015 Paris Air Show)

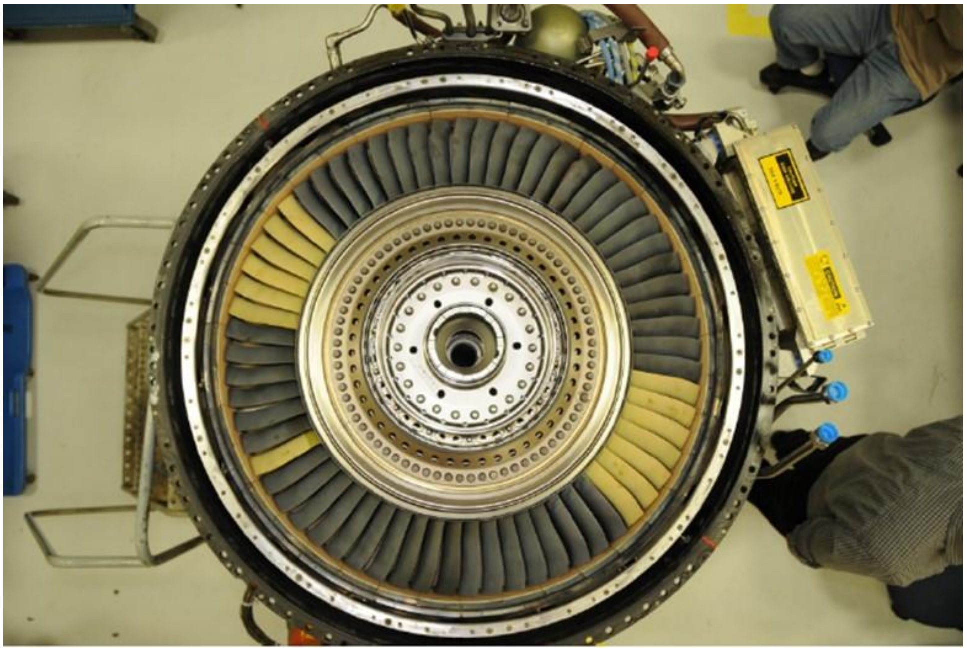

Figure 2. Photograph OF CMC Low Pressure Turbine Blades In An F414 Engine

Figure 3. Photograph Of Prototype CMC Turbine Blade By SNECMA

The majority of the experimental research conducted on CMCs to date have utilized flat panels for experiments. However, for this investigation, the objective was to make the next step and incorporate the shape and stress-state complexities found in the attachment features of aerospace turbine engine turbine blades. There are two studies in the literature that have addressed attachment features for CMC airfoils. Engle [5] has conducted a Small Business Innovative Research (SBIR) Phase I and Phase II program that studied attachments. In addition, attachment features have also been studied by Kumar [6]. Both of these studies were limited to monotonic loading conditions, and the attachment geometries that they studied are presented in Figure 4.

For this investigation the intent was to study the development of damage in the attachment regions of a generic CMC airfoil while being subjected to either monotonic loading as well as fatigue loading. In addition, load and thermal gradients would also be applied at the same time to more closely simulate actual engine environments that airfoils experience.

Finite Element Analysis (FEA) was used to design a generic CMC airfoil test specimen. For this investigation the generic CMC airfoil consisted of a rectangular cross-section that represented the airfoil, and this rectangular section transitioned into the attachment region. The attachment scheme selected for this study was a dovetail, as is shown in the GEA airfoil in Figure 1. This unique test specimen will be referred to as a subelement for the remainder of this report. Considerable time was spend performing FEA parametric studies to optimize the rectangular cross section and the dovetail design to maximize interlaminar stress levels..

FEA predictions of the complex stress state were compared to the actual damage state of subelements tested in tension, stepped loading, fatigue loading, and mechanical loading coupled with thermal gradients. The high temperature thermal gradient tests were performed in a burner rig to simulate the thermal gradients actual aerospace turbine engine airfoils experience in service and will therefore more accurately simulate the true stress state of the CMC blade airfoil. In addition to testing the subelements, traditional flat panel test specimens for tensile, interlaminar tension (ILT), interlaminar shear (ILS), double-notch compression (DNC), and creep rupture (CR) were manufactured. They were tested to provide input into the FEA model and to assist in guiding the durability testing of the subelements. Techniques such as Digital Image Correlation (DIC) and Acoustic Emission (AE), were used to identify cracking in the subelements, and to identify under what loading conditions the cracks arrest or continue to grow. Several subelements were sectioned, polished, and the microstructure photographed to create micrographs to document matrix cracks. This work builds off of the very limited work on CMC airfoils that is in the literature [5,6]. Examples of the attachment features previously studied are presented in Figure 4 and are of similar design to the subelement studied in this investigation. It is anticipated that the data in this report will provide extremely useful test data on a simulated airfoil for modeling teams working on progressive damage models for CMCs.

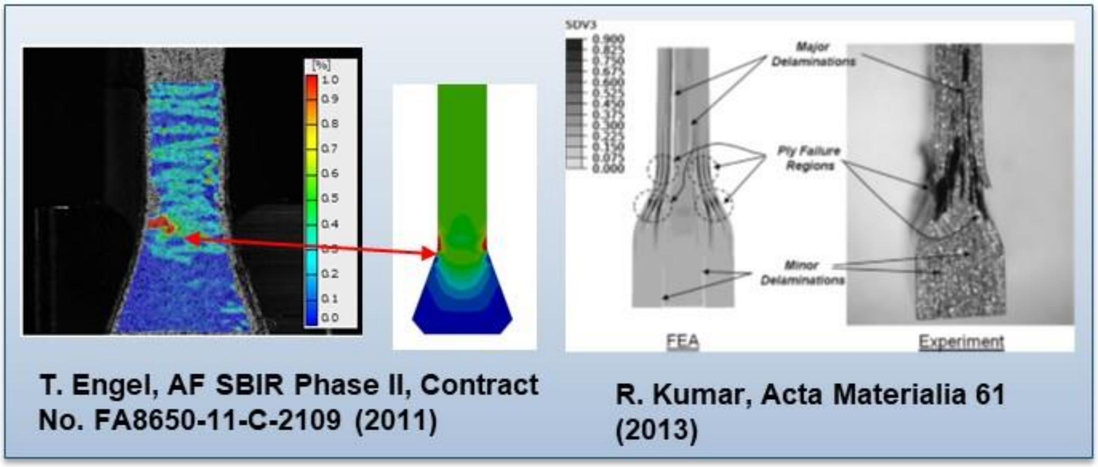

T. Engel, AF SBIR Phase II, Contract No. FA8650-11-C-2109 (2011)

R. Kumar, Acta Materialia 61 (2013)

Figure 4. Previous Studies Of CMC Airfoil Attachments

3. MATERIALS DESCRIPTION

3.1 Description of CMC Test Material

The SiC/SiC material studied in this investigation was manufactured by using plies of Hi-Nicalon^{TM} Five-Harness Satin Weave (5HSW) fabric to create a preform. The fibers in the preform were given a BN containing coating using chemical vapor infiltration (CVI). A silicon carbide matrix was applied over the BN using CVI. The preform was densified using a silicon carbide based slurry casting process followed by silicon melt-infiltration (SMI). The material and subelements were manufactured by Rolls Royce HTC. Examples of typical large pores are shown in Figure 5 for a low magnification image of the entire cross section of a flat panel while Figure 6 shows the large porosity at a slightly higher magnification. Examples of fine porosity typically found within fiber tows is presented in Figure 7.

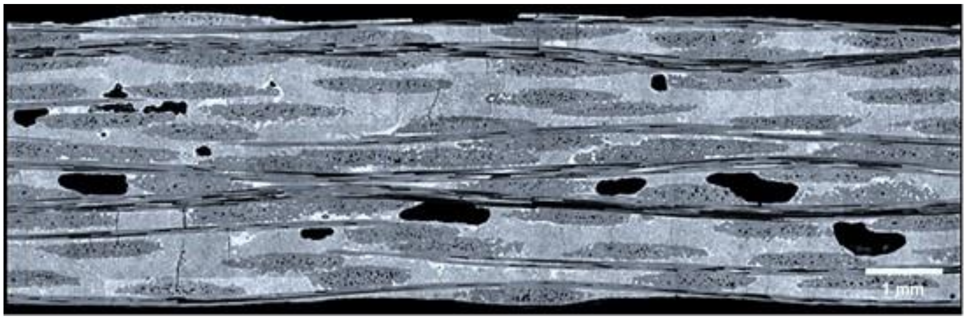

Figure 5. Low Magnification Image of SMI SiC/SiC Showing Large Pores

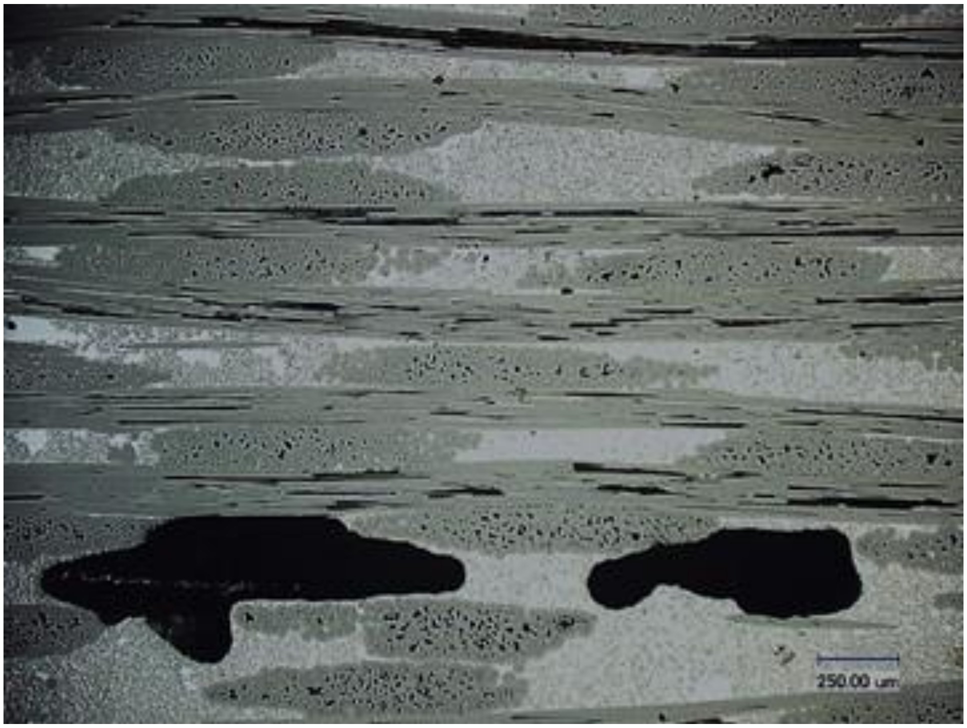

Figure 6. Intermediate Magnification Image of SMI SiC/SiC Showing Large Pores

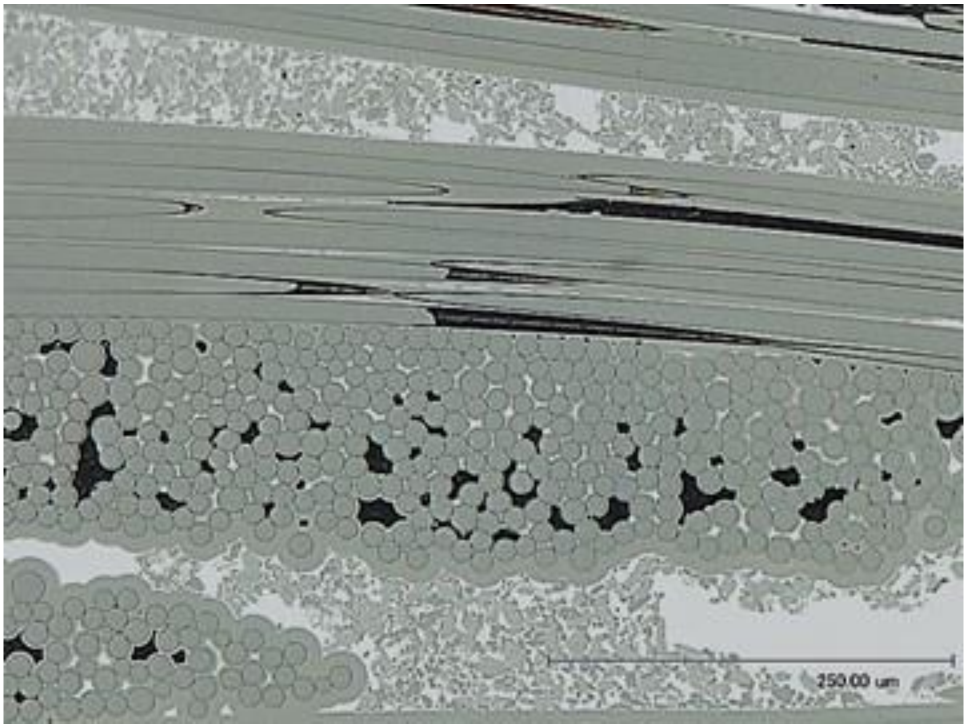

Figure 7. High Magnification Image of SMI SiC/SiC Showing Pores Within Fiber Tows

3.2 Manufacturing And Inspection Of Flat Panel Material

A standard flat panel with dimensions of 178 mm x 178 mm was manufactured for this project so that standard flat test specimens could be manufactured in order to measure basic properties. The panel consisted of 10 plies, resulting in a panel thickness of approximately 2.54 mm. The panel was processed to final density and was then shipped to AFRL/RXCC. After unboxing and visual inspection, the panel was imaged using flash thermography. The conditions for the thermography were Capture Frequency – 60 Hz, TSR Skip Frames – 0, Camera Frequency – 300 Hz. Acquisition Length was 900 frames in 15 seconds. Flash timing was Frame 10 with an offset of 4.2. Both the front and back of the panel were scanned, and the images at a time stamp of 0.100 seconds are presented in Figure 8. The panel appears to be very well consolidated with no sign of any delaminations. There is some spottiness to the images indicating varying degrees of density, but this is common and routine for this type of CMC that has between 10-15% porosity. Overall, the panels looked to be very good and passed inspection. They were then sent to a machine shop to be machined into test specimens.

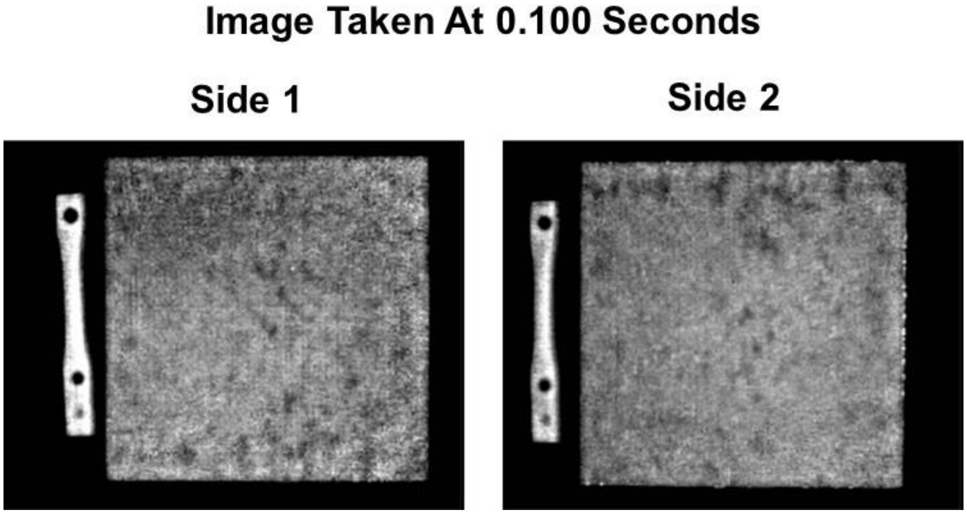

Figure 8. Thermography Scan of SMI SiC/SiC Panel At 0.1 Second

3.3 Microstructure Studies of CMC

The following methods were used to determine CMC constituent volume fractions for the SMI SiC/SiC CMC. Volume fraction was determined from polished cross sections made from material taken from a dogbone tensile specimen. .

A dogbone specimen from the flat panel was sectioned into smaller pieces so that the cross section could be studied using microscopy. The pieces were mounted and polished to a mirror scratch free finish. A total of 10 images were taken on a Keyence upright microscope of the polished cross section. The average fiber diameter was determined by measuring 100 random fiber diameters on the Keyence microscope and generating an average diameter. Photoshop was used to impose a predefined grid size on each of the ten micrographs (from previous grid convergence studies on SiC/SiC CMCS), and five features were classified, including fibers, CVI coating, matrix, inter-tow porosity, and intra-tow porosity.

A subelement was also sectioned so that the cross section could be studied. The pieces were mounted and polished to a mirror scratch free finish. A total of 10 images were taken on the Zeiss inverted AxioImager.Z1 of the polished cross section. The average fiber diameter was determined by measuring 100 random fiber diameters and generating an average diameter. This process was completed using ImageJ. The grid command and CellCounter program were used in ImageJ to find the volume fraction of fibers, CVI coating, intra-tow porosity, inter-tow porosity, and the matrix. The same grid size was used for both the subelement and the dogbone specimen. An example of the grid is shown in Figure 9. The dogbone specimen exhibited an average fiber radius of 7.20 microns with a standard deviation of 0.96 microns. The volume fraction for each constituent in the dogbone study are listed in Tables 1, 2, and 3. The volume fraction for each constituent in the subelement study can be found in Tables 4, 5, and 6.

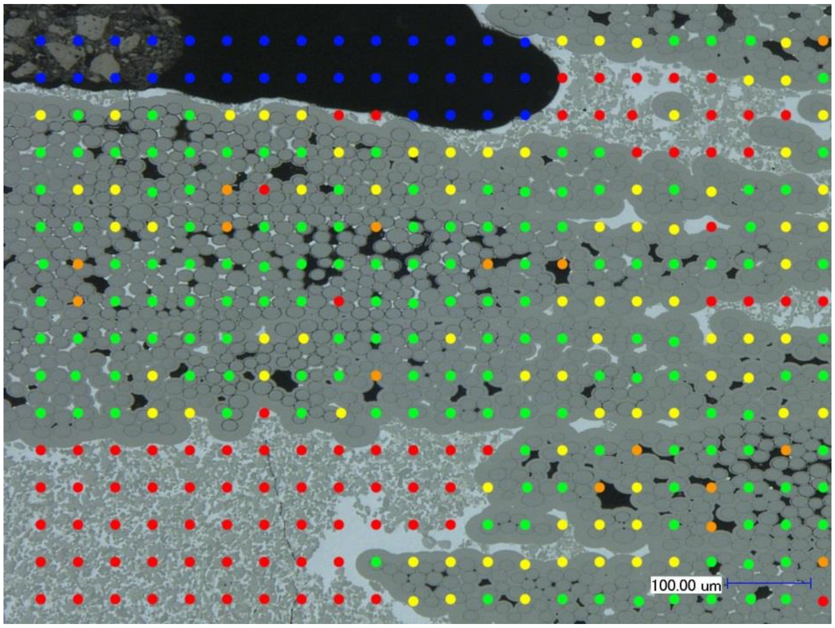

Figure 9: Example of VF: Green = Fiber, Yellow = CVI, Red = Matrix, Blue = Inter-tow Porosity, Orange = Intra-tow Porosity

Table 1: Estimated Constitute Volume Fractions

Constituent	**Volume Fraction**
Fiber	43%
CVI SiC Matrix	22%
Overall Porosity	12%
• Inter-tow Porosity	7%
• Intra-tow Porosity	5%
Silicon Melt Infiltrated Matrix	23%

Table 2: Porosity Volume Fraction For Dogbone Study

Constituent	**Volume Fraction**
Inter-tow Porosity	61%
Intra-tow Porosity	39%

Table 3: Matrix Volume Fraction For Dogbone Study

Constituent	**Volume Fraction**
Matrix Porosity	24%
Matrix Material	76%

Table 4: Overall Constituent Volume Fraction For Subelement Study

Constituent	**Volume Fraction**
Fiber	35%
CVI SiC Matrix	21%
Overall Porosity	13%
• Inter-tow Porosity	9%
• Intra-tow Porosity	4%
Silicon Melt Infiltrated Matrix	31%

Table 5: Porosity Volume Fraction For Subelement Study

Constituent	**Volume Fraction**
Inter-tow Porosity	68%
Intra-tow Porosity	32%

Table 6: Matrix Volume Fraction For Subelement Study

Constituent	**Volume Fraction**
Matrix Porosity	23%
Matrix Material	77%

3.4 NDI of Test Specimens From Flat Panel

Flash thermography was performed on all test specimens machined from the flat panel. The IR Camera settings were capture frequency of 60 Hz, TSR Skip Frames was 0, and Camera Frequency was 300Hz. The acquisition length for frames was 900 and seconds was 15. Flash timing used a frame of 10, an offset of 4.2, and a duration of 4.9. Each Specimen was compared to a similar CMC specimen that had drilled flat bottom holes on the back surface to represent defects. The defects represent 25%, 50%, and 75% of remaining material and were intended to simulate delaminations. The thermograph scan of the dogbone test specimen is shown in Figure 10 , the DNC test specimen scan is shown in Figure 11, and the ILT test specimen scan is shown in Figure 12. All test specimen passed the scans with no indications of delaminations or observable defects being present.

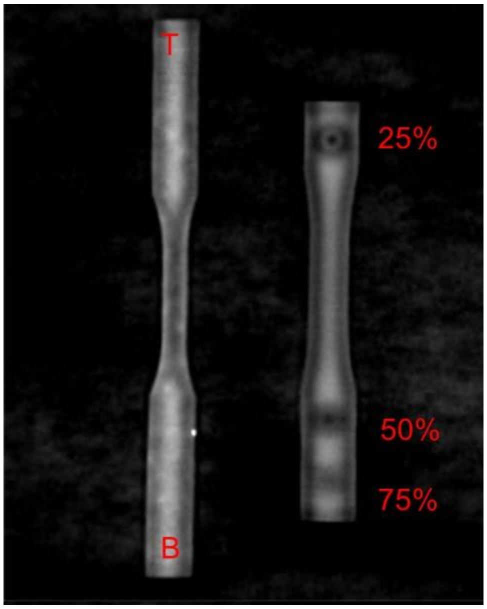

Figure 10. Thermography Scan Of Dogbone Test Specimen

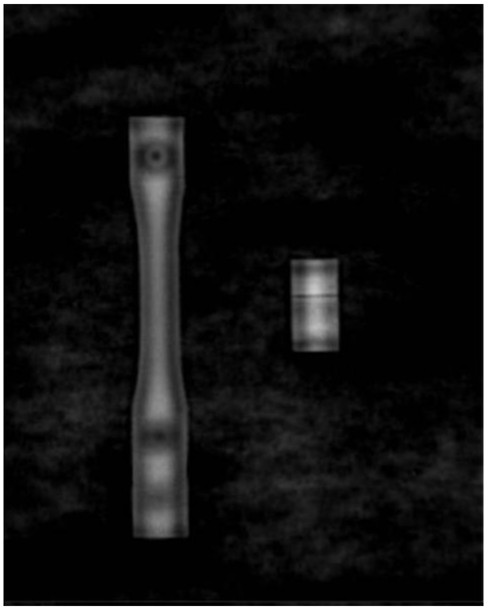

Figure 11. Thermography Scan Of Double Notch Compression Test Specimen

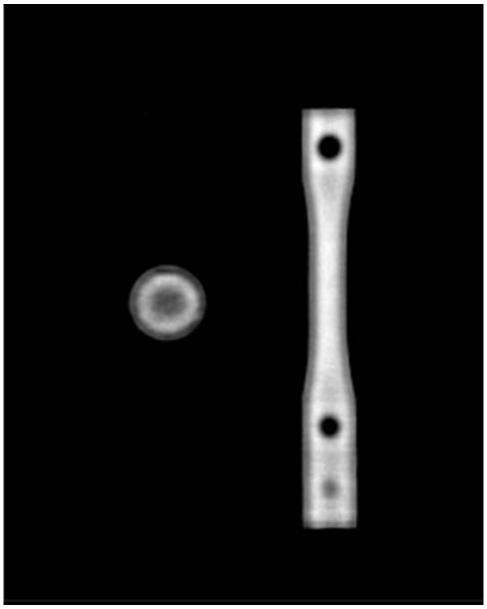

Figure 12. Thermography Scan Of ILT Test Specimen

3.5 NDI of Subelement Panel

Rolls-Royce used IR to study the as-manufactured subelement panel. There were no indications of any delaminations observed in the panel. Therefore, the panel was machined into individual subelement test specimens. A copy of the IR scans was not provided to AFRL/RXCC.

4. TEST METHODOLOGY AND PROCEDURE

Very specific test equipment was used to conduct the testing of the CMC test specimens in this study. Well defined test protocols were used to test both the flat test specimens as well as the subelement test specimens. Each experiment required a separate test plan and data acquisition plan.

4.1 Test Procedures

4.1.1 Servo-Hydraulic Test Frame

Flat panel test specimens as well as the subelements were tested using a standard servo-hydraulic test frame mounted with MTS-645 wedge grips. Elevated temperature tests of the flat specimens were conducted using a resistance heated furnace. Multiple zones of temperature control produced a temperature range that was within 1% of the test temperature across the length of the gage length. The room-temperature experiments utilized an extensometer, digital image correlation, and acoustic emission to monitor damage evolution. Photographs of the test setup for a subelement is shown in Figure 13.

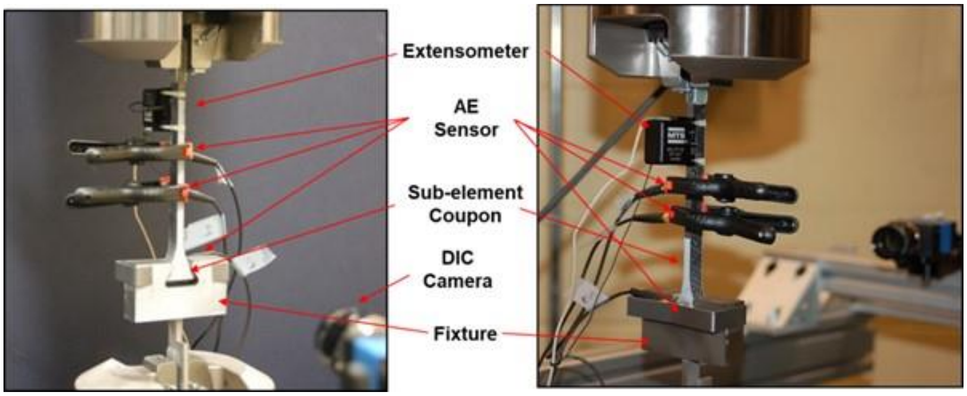

Figure 13. Optical Photographs Of The Highly Instrumented Test Set Up for Subelements

4.1.2 Burner Rig

A high velocity burner rig test facility was used to simulate the thermal conditions a CMC airfoil would experience in a turbine engine.[7,8] The burner rig utilizes a high velocity oxygen fuel (HVOF) gun set up to run with a lean-burn combustion gas mixture that is oxygen, propane, and air controlled to flow rates of 232, 65, and 368 standard cubic feet/hour (scfh), respectively. Temperature on the specimen front surface was measured using a forward looking infrared radiometer (FLIR) camera (Thermacam P640). A photograph of the burner rig test frame is shown in Figure 14. The test facility has been thoroughly described previously.[7,8] The goal was to quantify the effects of a thermal gradient on the initiation and growth of matrix cracking as a function of load compared to room temperature testing.

A photograph of the subelement in the burner rig is presented in Figure 15. MTS wedge grips are shown, along with the HVOF gun, the CMC subelement, and the heat shield. A MTS wedge grip holds the top stem region of the specimen, while the bottom dovetail section of the subelement is held in place by the machined dovetail grip fixture. A closer view of the test setup is presented in Figure 16. In this photograph the HVOF gun can be clearly seen heating the CMC subelement. Insulation is placed on top of the lower machined metal dovetail grip to keep it from getting too hot during testing. The insulation essentially acted as a blade platform and prevented the metallic dovetail grip section from getting too hot. This insulating sheet mimics the actual CMC airfoil design used in aerospace turbine engines as was shown in Figure 1. The result is the dovetail section of the subelement is at a much lower temperature than the stem that is immediately above the insulation.

The HVOF gun produces a flame that is directed directly at one face of the subelement. An expanded view showing a CMC subelement being heated is shown in Figure 17. In this image one can observe that there is uniform heating across the width of the specimen and that the hot zone is approximately as long as the specimen is wide. This very unique heating arrangement does an excellent job of simulating the actual loading and heating environment that a CMC airfoil would experience.

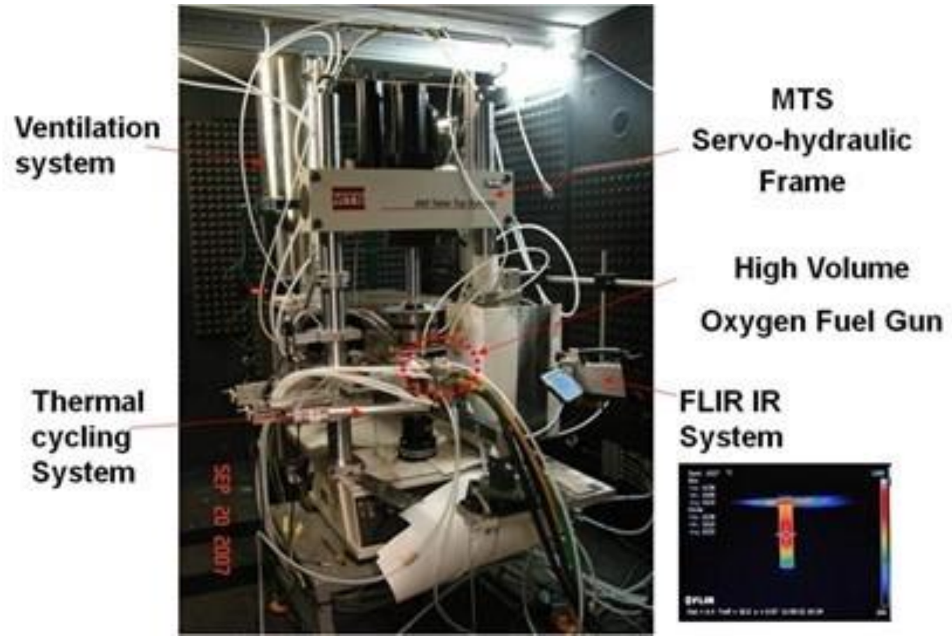

Figure 14. Photograph Of Burner Rig Test Frame

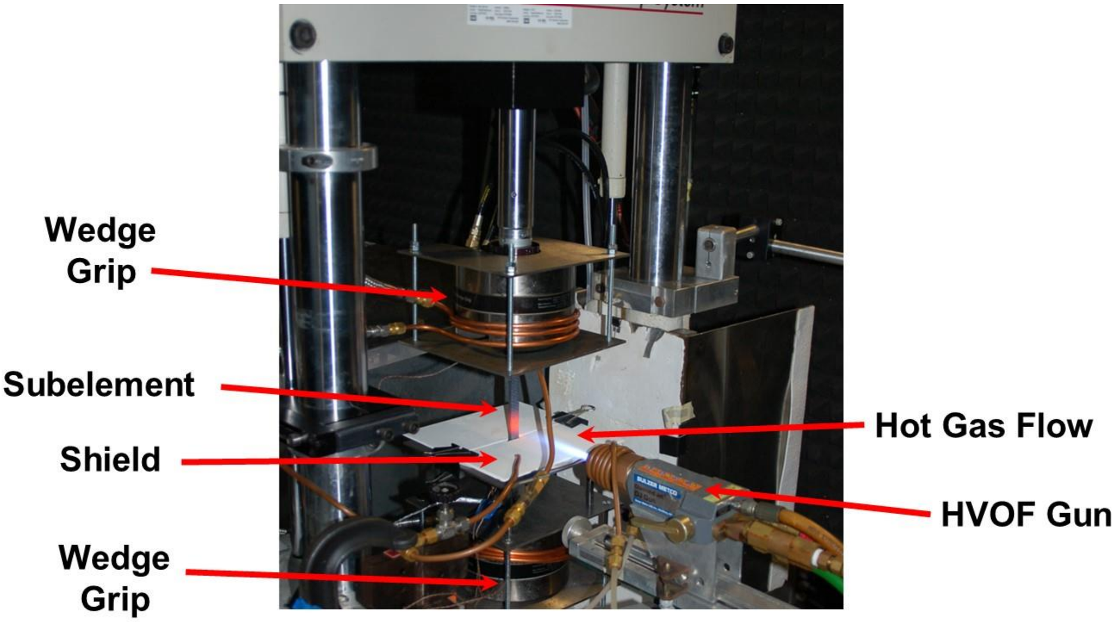

Figure 15. Expanded View Of Subelement In Burner Rig

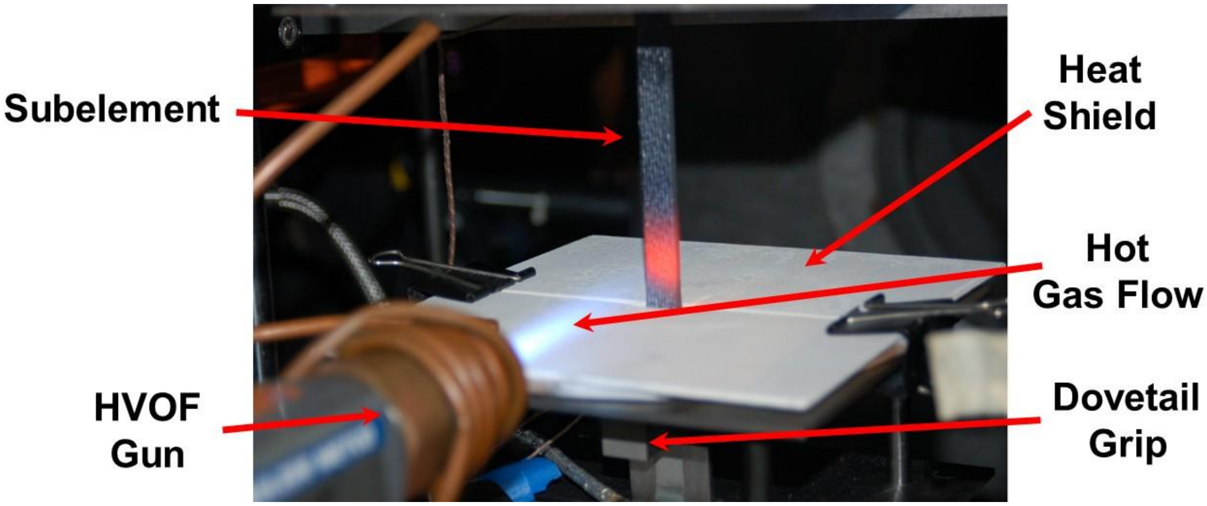

Figure 16. Photograph Of Burner Rig Showing the HVOF Gun In Operation Heating A CMC Subelement Test Specimen

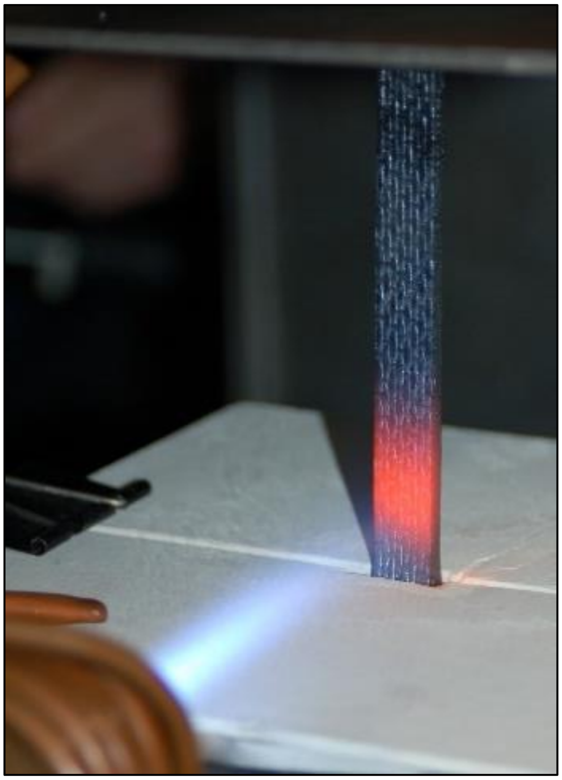

Figure 17. Close-up Photograph Of A Subelement Test Specimen Being Heated In Burner Rig

4.1.3 Burner Rig Temperature Calibration

A temperature calibration experiment was conducted to determine the operating conditions of the HVOF gun as well as the required working distance to achieve the required test temperatures. A Rolls-Royce SMI HI Nicalon/BN/SiC test speicmen was placed in the wedge grips and the parameters were determined and recorded. The actual test temperature had not been determined at the time, so several temperatures were profiled. The test specimen was calibrated at 800°C, 1000°C, and 1200°C as measured by a FLIR infrared camera. The temperature of 1200°C was the recommended maximum temperature for the calibration test CMC. Therefore, a second CMC was used to calibrate at 1300°C. This CMC was a Sylramic iBN/Pyrolitic Carbon/CVI SiC with a 2:1 fiber ratio. A photograph of the IR camera output is shown in Figure 18.

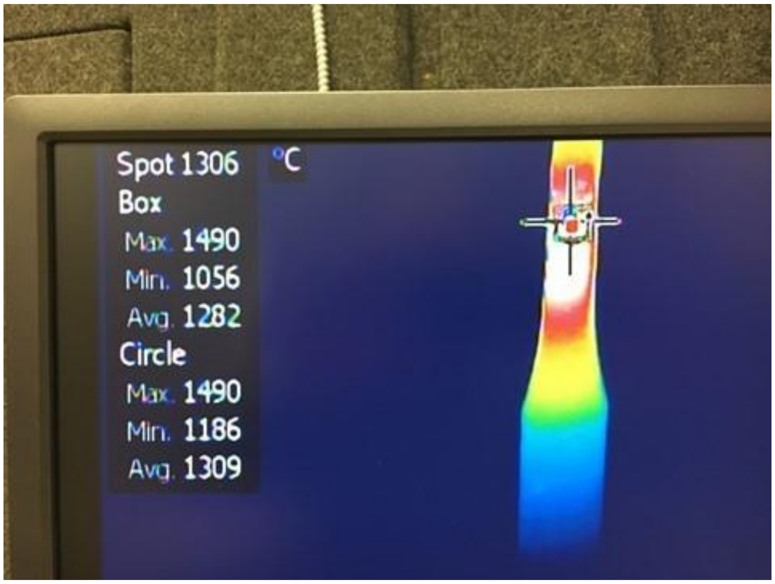

Figure 18. Image From FLIR Camera Of CMC Test Specimen At 1300°C

The values for gas flow through the HVOF gun were set using past experience with the burner rig for optimum flame temperature. Then the HOVF gun was moved to several different distances from the test specimen using a unislide. The distance that produced each required test temperature was recorded.

4.1.4 Burner Rig Heat Flux Calibration Using a Calorimeter

Once the relationship between temperature and distance of the HVOF nozzle was determined, a second calibration run was conducted to determine the heat flux for each temperature that was calibrated. The idea was to accurately measure heat flux, and then this heat flux could be used to perform a detailed thermo-structural analysis of the subelement.

A calorimeter was used to measure heat flux. A schematic of the calorimeter is presented in Figure 19, and a photograph of the calorimeter used is presented in Figure 20. Calibration data for this particular calorimeter is presented in Table 7. This calorimeter was specially ordered with a length of the body of 20” in order to work in the burner rig. Each calorimeter is ordered for a specific maximum flux value. The team was not sure what flux the HVOF gun would generate. Therefore, a calorimeter was ordered that would be able to measure 100 W/mm2 at 10 mV. The manufacturers stated that the calorimeter could be run to more than 50% of that value as long as the cooling water was effective.

The calorimeter was positioned in positioned in front of the calorimeter and the flame was lined up to be centered on the face of the calorimeter. The HVOF gun was then moved to each corresponding distance from the calorimeter and the heat flux was recorded. Figure 21 is a photo of the calorimeter in place during operation of the burner rig during calibration.

The heat fluxes were measured at the same distances that produced the temperatures of 800°C, 1000°C, 1200°C, for the Rolls-Royce SMI Hi-Nicalon/BN/SiC CMC and at the distance that produced a temperature of 1300°C for the Sylramic iBN/Pyrolitic Carbon/CVI SiC 2:1 fiber ratio CMC system. Heat flux values versus distance from the CMC are presented in Table 8, and they are also presented graphically in Figure 22. Heat flux versus CMC temperature is presented in Figure 23. The data suggests there is an exponential relationship between heat flux and temperature for these SiC/SiC CMCs.

It is important to note that the two highest heat flux values were beyond the calibration range of the calorimeter. Therefore, they are presented for reference purposes only. For this program the values of heat flux were only measured to determine the order of magnitude for the heat flux associated with each test temperature. The team did not have the time and resources to perform a detailed thermo-structural analysis. If a detailed thermo-structural analysis were required, then a different calorimeter with a much higher heat flux capacity would need to be utilized.

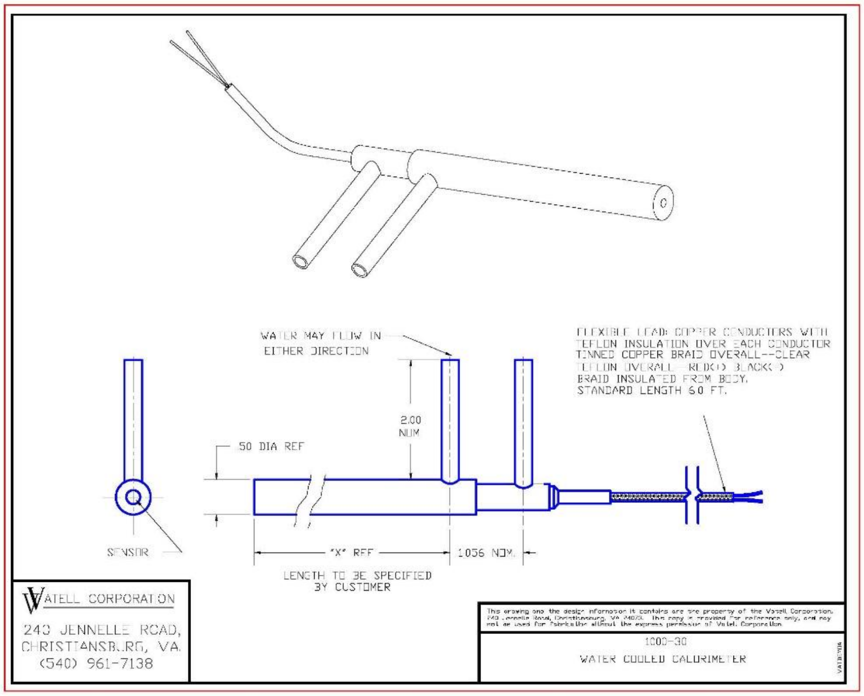

Figure 19. Schematic Of Calorimeter Used to Measure Heat Flux

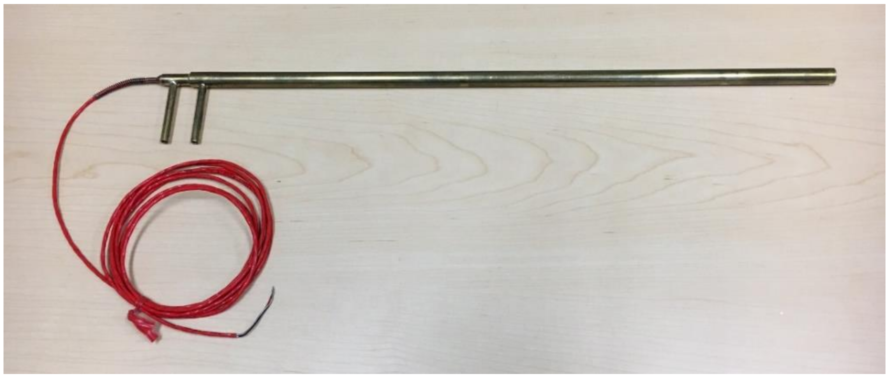

Figure 20. Optical Photograph Of Calorimeter Used To Measure Heat Flux

Table 7. Thermogage 1000-30 Calibration Values

PROPERTY	VALUE
Sensor Scale Factor	10.80 W / cm^2 / mV
Sensor Sensitivity	0.092 mV / W /cm^2
Sensor Range	0 - 108 W / cm^2
Sensor Coating	Promark 1200 (1 mil thick)
Emissivity	0.95
Resistance	1 ohm
Ambient Temperature	23°C
Humidity	29%
Reference Pyrometer	MI60 #5972: Cert. 070914

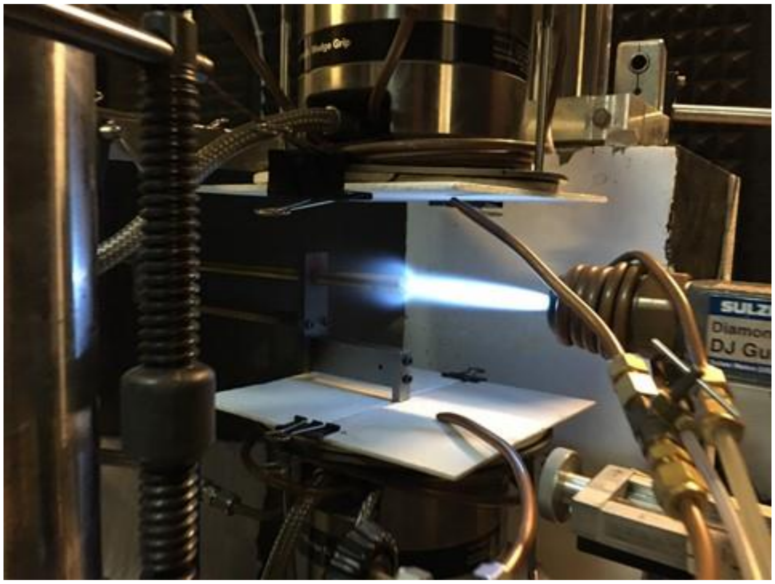

Figure 21. Optical Photograph of Calorimeter In the Burner Rig During Calibration of Heat Flux.

Table 8. CMC Temperature, Corresponding Heat Flux, And Distance of HVOF Gun From CMC

Ceramic Matrix Composite System	CMC Surface Temperature (C)	Heat Flux W/cm^2	Distance From Specimen (mm)
SMI Hi-NiC/BN/SiC	800	90	143
SMI Hi-NiC/BN/SiC	1000	145	112
SMI Hi-NiC/BN/SiC	1200	209	88
*CVI Syl/C/SiC 2:1	1300	350	68

*Sylramic-iBN/PyC/CVI SiC (2:1), Exceeded Calorimeter Linear Output

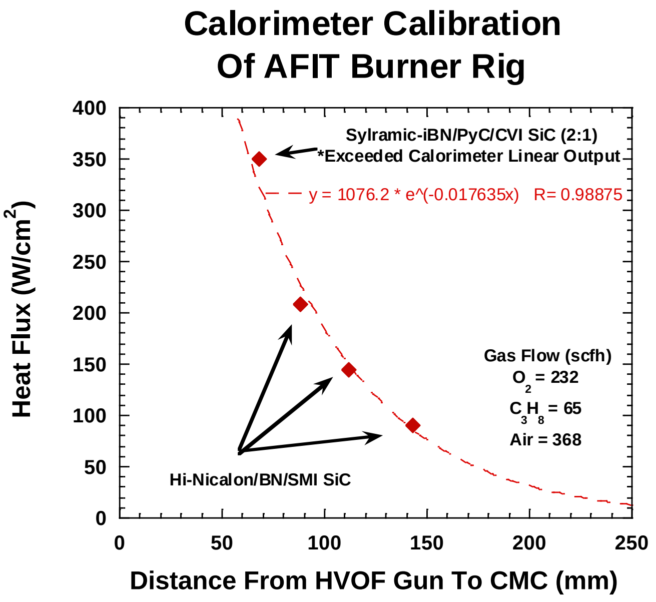

Figure 22. Heat Flux Shows a Exponential Relationship With Position Of The HVOF Gun Nozzle

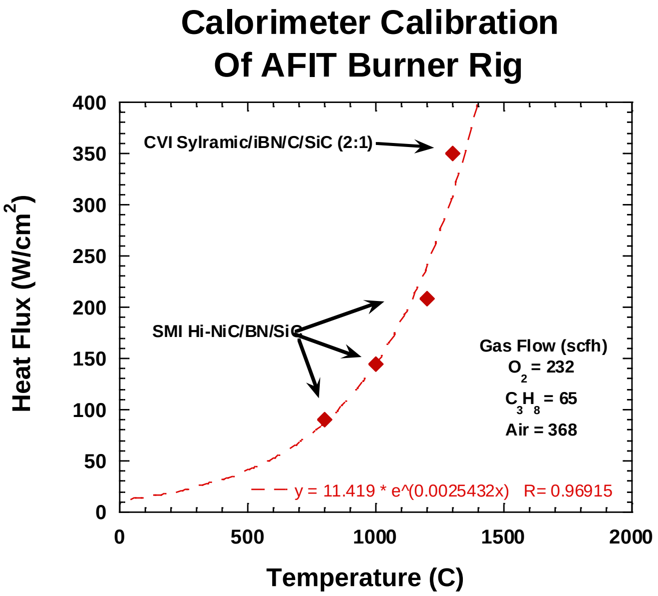

Figure 23. Heat Flux Versus SMI SiC/SiC Specimen Surface Temperature

4.1.5 Grip Design For Subelement

It was critical to develop successful gripping and alignment methods for testing the subelements. A drawing of the subelement test specimen is presented in Figure 24. Both the information-rich servo-hydraulic test frame and the burner rig test systems utilize MTS 647 wedge grips. These grips cannot directly accommodate the dovetail feature of the subelement. A specialized gripping fixture for the dovetail was designed and constructed. The design was based on the inverse of the blade dovetail detail. A 3D SolidWorks model was used to create machining drawings for the gripping fixture. As part of this process, the subelement dovetail detail (contact area flatness and angle with respect to the specimen centerline) was verified on the as-received/as-manufactured specimens as well as the fixture using optical microscopy and optical profilometry. Each specimen was imaged 1:1 and the angle of the grip surfaces with respect to the base surface was verified, as shown in Figure 25. The optical microscopy was done using a Keyence microscope and flatbed scanner. The optical profilometry was done by Casey Holycross o using a Keyence profilometer. Generally, the subelement test speicmen surfaces had very good agreement to the fixture surfaces using both methods. Standard measurements of the stem width and thickness were made to determine the test section cross-sectional area calculation for testing.

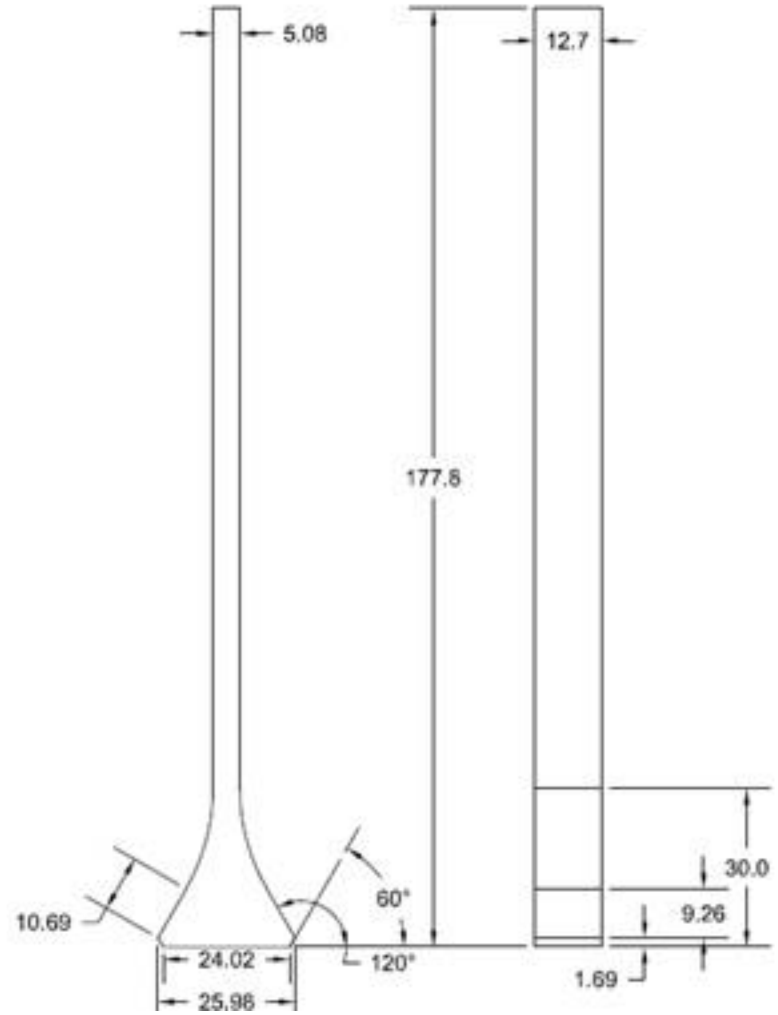

Figure 24. A Machining Drawing For The Subelement Test Specimen (mm)

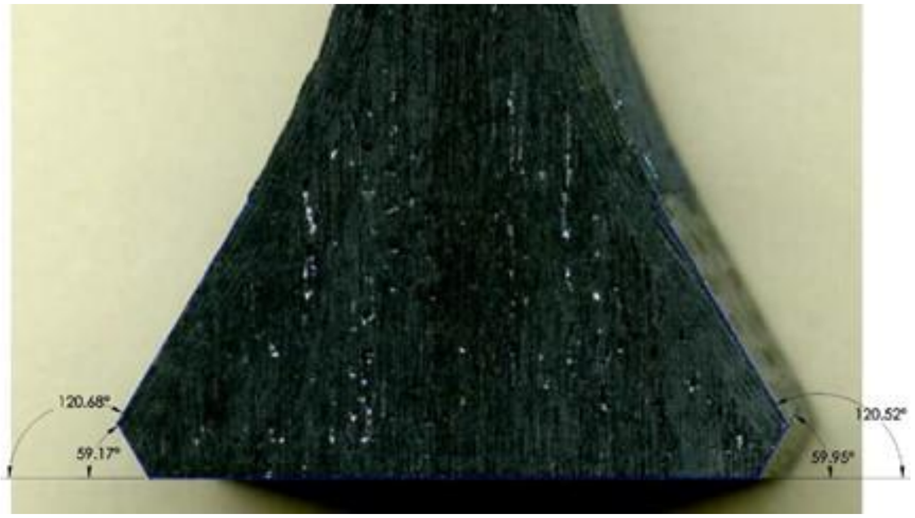

Figure 25. Angles Were Measured On Each Subelement Test Specimen

A prototype grip fixture was first created using a 3-D printing method and it worked perfectly. The grip fixture was then machined out of IN100, which is a high temperature nickel-based superalloy that retains almost all of it's strength up to 815°C and still exhibits reasonable strength up to 1000°C. A schematic of the gipping fixture is shown in Figure 26. The stem of the fixture was gripped in the MTS 647 wedge grips and the specimen is simply slid into the feature cut-out. The straight-side of the subelement was tabbed and gripped by the top 647 wedge grip. A photograph of the actual grip insert used to grip the subelement is shown in Figure 27. It is important to note that for the burn rig testing the stem of the grip was rotated 90° to accommodate how the grips were mounted in the test frame and the orientation of the HVOF gun.

Figure 26. Schematic OF Wedge Grip Insert Used To Grip Subelement

Figure 27. Photograph Of Wedge Grip Insert Used To Grip Subelement

4.1.6 Alignment of Gripping Fixture And Load Train

A preliminary plan was developed to ensure consistent grip alignment between the two different test rigs used for this project. The plan included following normal protocols for ensuring coarse and fine alignment adjustment and verification between the two MTS 647 grips using a round specimen and collet style inserts and then a flat rectangular bar of the appropriate length with strain gages. After the alignment for the wedge grips had been evaluated, the subelement grip fixture was installed in the lower wedge grip. Alignment verification was performed on a specialized alignment subelement test specimen. This alignment specimen was made of precision-ground A2 tool steel, using the same geometry as the CMC subelements. A schematic of the alignment specimen is shown in Figure 28.

The alignment specimen had eight strain gages installed to measure strain according to the procedures identified in ASTM E1012 for thick rectangular specimens. Alignment criteria for CMC testing requires that there be no more than 5% bending strain at an average axial strain of 0.0005 mm/mm. The alignment specimen was placed in and out of the grips multiple times to document repeatability of alignment. After much work the load train was aligned to within the ASTM specifications.

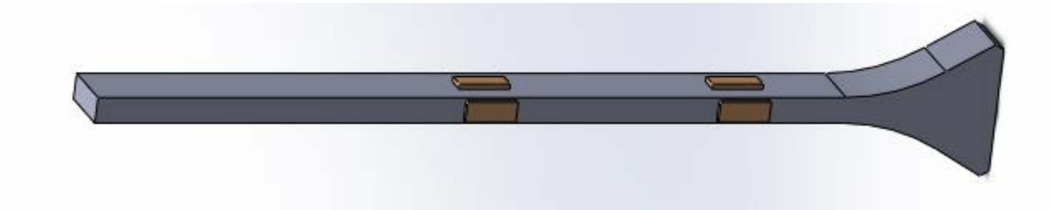

Figure 28. Subelement alignment specimen with strain gages.

4.1.7 Digital Image Correlation

Digital image correlation (DIC) [9,10,11] is an optical method that employs tracking and image registration techniques for accurate 2D and 3D measurements of changes in images. This method is often used to measure full-field surface displacements, and it is widely applied in many areas of science and engineering. Compared to strain gages and extensometers, the amount of information gathered about the fine details of deformation during mechanical tests is increased significantly due to the ability to provide both local and average displacement and strain data over the entire surface.

To improve tracking of the DIC Camera, an aerosol spray paint was used to apply a random speckle pattern to each specimen pre-test via an airbrush to create a random speckle pattern with appropriate size, distribution, and high-temperature capable characteristics for digital image correlation. After paint application, specimens were allowed to dry for 24 hours and then placed in a furnace at 93.3°C overnight to ensure complete curing. Post cure analysis using a high-magnification optical microscope showed an average speckle size of 100 µm. Two blue high intensity LED lamps (450 nm wavelength) illuminated the specimen and were focused on the gage section. Two Grasshopper 5.0 megapixel cameras with 2/3" Sony ICX625 CCD sensors were used for optical imaging and were outfitted with 25 mm fixed focal length Micro-Nikkor lenses. Bandpass filters were placed in front of the cameras to isolate the wavelength of blue light (450-495 nm) reflected from the specimen. The actively illuminated monochromatic light passes through the filter, improving the signal to-noise ratio of the LED light to the ambient light. Vic-Snap and Vic-3D (Correlated Solutions) data acquisition and post-test analysis strain measurements based on DIC were verified against a calibration standard with strain gages prior to testing of the CMC samples [20]. A photograph of a subelement with the DIC speckle pattern applied to one edge is shown in Figure 29.

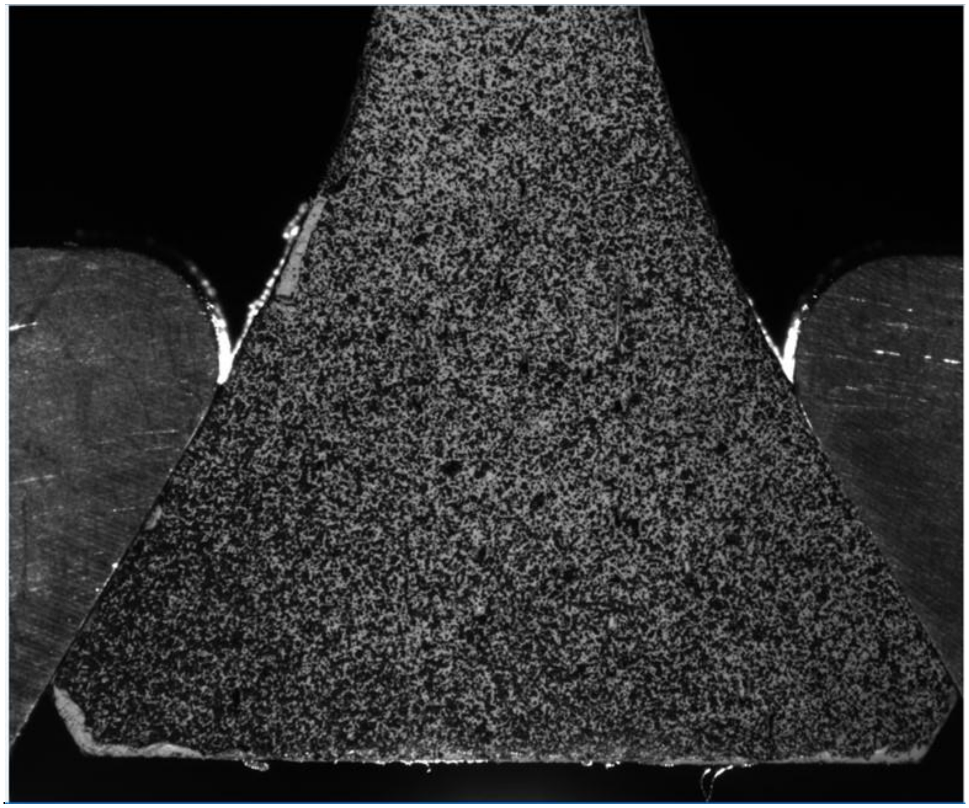

Figure 29. DIC Image Of Dovetail Section of Subelement With DIC Speckle Pattern

4.1.8 Acoustic Emission

Acoustic emission (AE) [12, 13] is the phenomenon of radiation of acoustic (elastic) waves in solids that occurs when a material undergoes irreversible changes in its internal structure, for example as a result of crack formation or plastic deformation due to aging, temperature gradients or external mechanical forces. In particular, AE is occurring during the processes of mechanical loading of materials and structures accompanied by structural changes that generate local sources of elastic waves. This results in small surface displacements of a material produced by elastic or stress waves generated when the accumulated elastic energy in a material or on its surface is released rapidly. The waves generated by sources of AE are of practical interest in structural health monitoring (SHM), quality control, system feedback, process monitoring and other fields. In SHM applications, AE is typically used to detect, locate and characterize damage

For subelement testing, high-fidelity, wide-band (B1025, 50 kHz-1.5 MHz) AE sensors (10 mm diameter) were used to record crack related events. Acoustic coupling media and custom sensor holders were used to attach the sensors to the specimen. An 8-channel Digital Wave FM-1 system was used to record acoustic emission waveforms. Each signal passed through a 20 dB pre-amplifier before entering the FM-1 system for signal conditioning. The Wave Explorer™ software was capable of continuously measuring the load as well as taking discrete load measurements whenever an AE event occurred. The sensors were between the grips along the side of the subelement. The edge mounted configuration showed a lower sensitivity to lead breaks than conventional surface mounted sensors and required +1dB amplification. Therefore, amplification of the filtered signal was increased from 2 dB when surface-mounted to 3dB when edge mounted. For location of AE events, the Akaike Information Criterion (AIC) was used to determine the time-of-flight of each waveform from all channels. AIC uses a minimization process to distinguish between noise and the actual signal. The time at which this algorithm is at a minimum is chosen as the time of flight for the given signal. This technique has been successfully applied to location of crack signals in thin plates.

4.1.9 X-Ray Computed Tomography

In Addition to IR, X-Ray Computed Tomography (CT) was performed on selected subelements to document the amount of porosity in the attachment region as well as in the stem and to check for delaminations. A Zeiss Xradia Versa XRM-520 was used with a 4x magnification which required scanning two overlapping regions to encompass the desired area, which is shown in Figure 30a. Slices were reconstructed in different orientations (y-x, z-y, and z-x). Examples of a slice from the CT data in the y-x and the z-x orientations are shown in Figure 30b) and Figure 30c), respectively. The data were used to determine if there are large pockets of connected porosity or other defects in the z and y directions. This information was being used to rank the test specimens in test priority and to potentially be used to feed the predictive model.

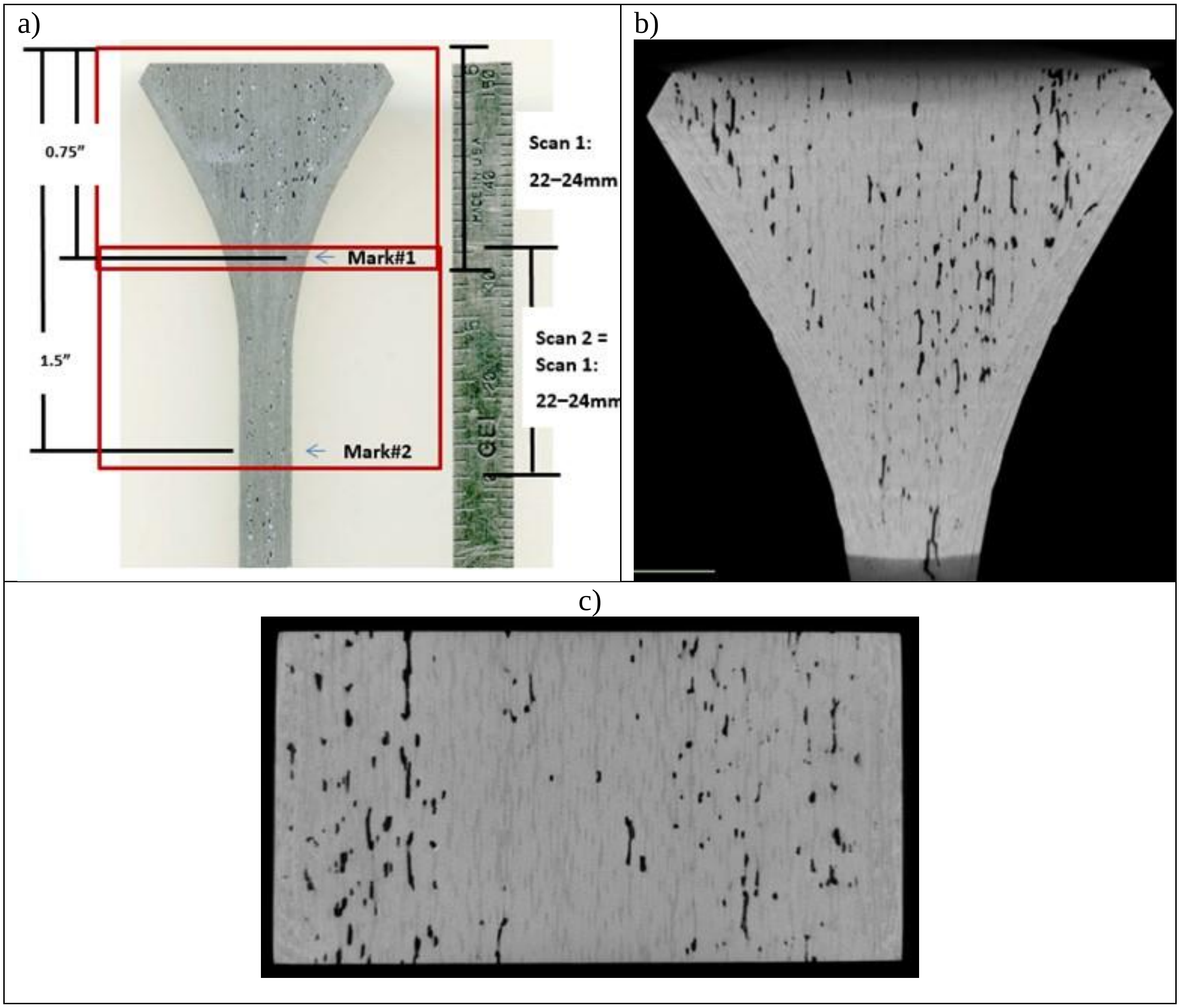

Figure 30. a) Photo Showing Focus Areas of The CT Scan, b) Example Slice From The Y-X Orientation, and c) Example Slice From The Z-X Orientation

4.1.10 Optical Microscopy of Subelement Test Specimen

Failed subelement test specimens were studied using optical microscopy to document the fracture behavior. In addition, detailed microscopy was performed to document actual matrix cracks along the edge of the attachment region of the subelement test specimen. In some cases, both the surface edge and center of the attachment region of the subelement test specimen were studied. In order to do this characterization the dovetail section of the subelement was first sectioned into two pieces. The sectioning cut was down the centerline of the test specimen. For one half the centerline face was polished. The second half had the surface edge face polished that had the DIC speckle pattern applied to it. The two halves were mounted and polished using standard ceramography techniques. After polishing, high resolution optical images were recorded for each half. The images were then stitched together to create a montage of the entire polished cross section. By using high resolution images, it was possible to zoom in and identify any matrix cracks that were present. The cracks in the images were traced over using bold white lines to highlight the cracks. This technique was performed on subelement test specimens that failed as well as for subelement test specimens where the tests were interrupted and stopped.

4.2 Flat Panel Test Matrix

The flat panel was used to generate basic material mechanical behavior data. A test matrix was developed, specimen drawing generated, and specimens machined. The test matrix for all the flat panel test specimens is shown in Table 9. It was determined that testing would include monotonic and creep rupture testing using dogbone specimens at room and elevated temperature, interlaminar tension of 1" round button test specimens, and interlaminar shear using double notch compression (DNC) test specimens.

Table 9. Baseline Property Test Matrix

Test Type	Temperature	# of Tests	Instrumentation
Tension	RT	1	DIC, AE, extensometer
Stepped Tension	RT	1	DIC, AE
Tension	800 C	1	AE, extensometer
Tension	1200 C	1	AE, extensometer
Creep	1200 C	1	extensometer
ILS/DNS	RT	3	DIC
ILT	RT	2	DIC, extensometer

4.3 Flat Panel Specimen Designs

The flat panel was machined into four ILT specimens, nine DNC specimens, and eight dogbone specimens. The dogbone test specimens were designed to be used for both tension testing as well as elevated temperature creep rupture testing. Specimens were machined from the panel using diamond tooling following established practices identified by ASTM. A schematic of how the panel was machined from the flat panel is shown in Figure 31. The drawing for the ILT specimen is shown in Figure 32 while an optical photograph of the ILT specimens is shown in Figure 33. The DNC specimen drawing is presented in Figure 34 while an optical image of the DNC specimen is presented in Figure 35. The dogbone specimen drawing is shown in Figure 36 while an optical image of one of the test specimens is presented in Figure 37.

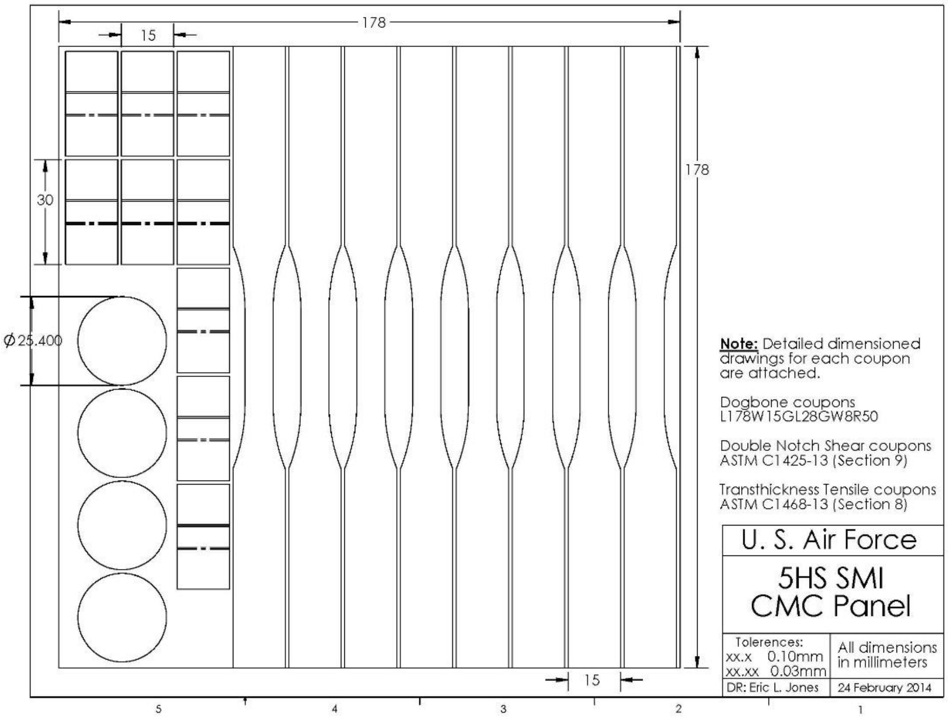

Note: Detailed dimensioned drawings for each coupon are attached.

Dogbone coupons
L178W15GL28GW8R50

Double Notch Shear coupons
ASTM C1425-13 (Section 9)

Transthickness Tensile coupons
ASTM C1468-13 (Section 8)

U. S. Air Force

5HS SMI
CMC Panel

Tolerences: xx.x 0.10mm xx.xx 0.03mm	All dimensions in millimeters
DR: Eric L. Jones	24 February 2014

Figure 31. Machining Drawing For Flat Panel of SMI SiC/SiC

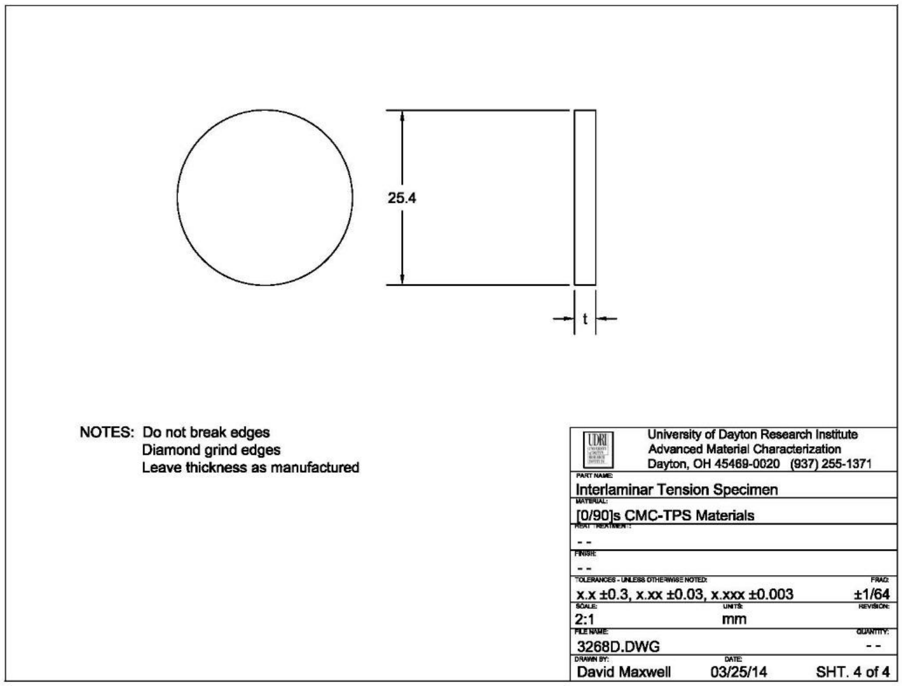

NOTES: Do not break edges
Diamond grind edges
Leave thickness as manufactured

University of Dayton Research Institute
Advanced Material Characterization
Dayton, OH 45469-0020 (937) 255-1371

PART NAME: Interlaminar Tension Specimen
MATERIAL: [0/90]s CMC-TPS Materials
HEAT TREATMENT: - -
FINISH: - -
TOLERANCES - UNLESS OTHERWISE NOTED: x.x ±0.3, x.xx ±0.03, x.xxx ±0.003 FRAC: ±1/64
SCALE: 2:1 UNITS: mm REVISION:
FILE NAME: 3268D.DWG QUANTITY: - -
DRAWN BY: David Maxwell DATE: 03/25/14 SHT. 4 of 4

Figure 32. Machining Drawing For Interlaminar Tension Specimen

Figure 33. Photograph of Interlaminar Tension Specimen

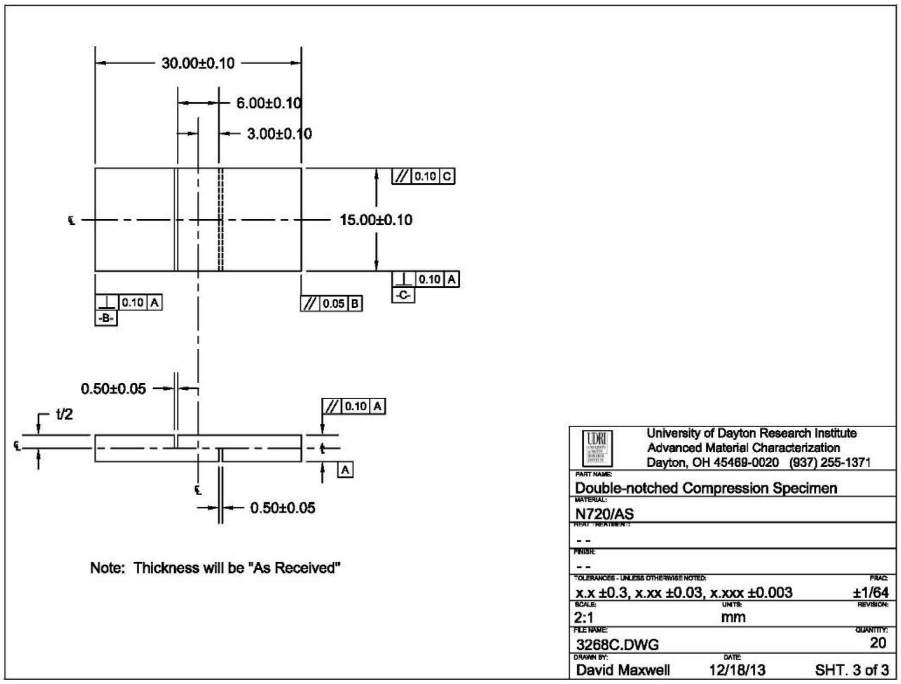

Note: Thickness will be "As Received"

University of Dayton Research Institute
Advanced Material Characterization
Dayton, OH 45469-0020   (937) 255-1371

PART NAME: Double-notched Compression Specimen
MATERIAL: N720/AS
HEAT TREATMENT: - -
FINISH: - -
TOLERANCES - UNLESS OTHERWISE NOTED: x.x ±0.3, x.xx ±0.03, x.xxx ±0.003
FRAC: ±1/64
SCALE: 2:1
UNITS: mm
REVISION:
FILE NAME: 3268C.DWG
QUANTITY: 20
DRAWN BY: David Maxwell
DATE: 12/18/13
SHT. 3 of 3

Figure 34. Machining Drawing For Double Notch Compression Test Specimen

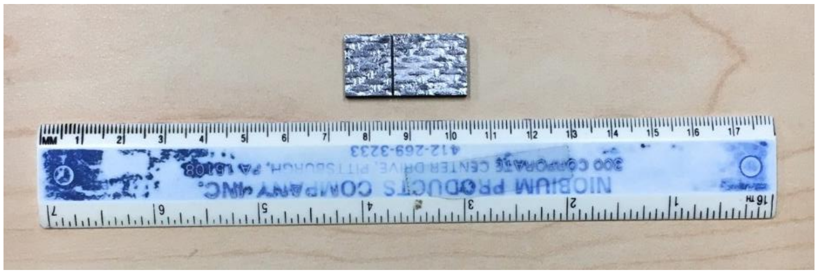

Figure 35. Photograph of Double Notch Compression Test Specimen

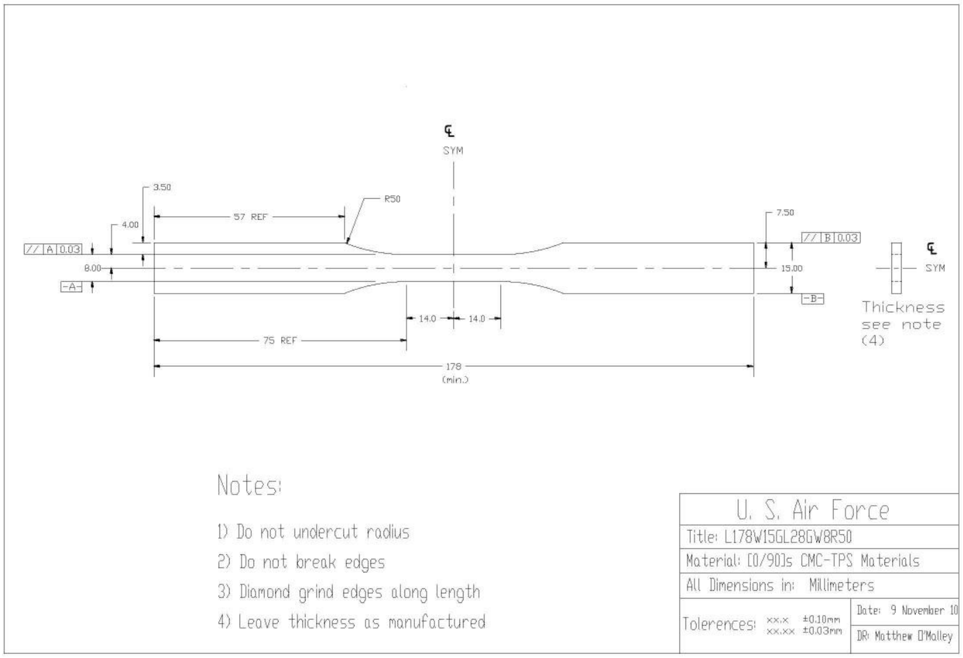

Figure 36. Machining Drawing For Dogbone Specimen Used For Tension and Creep Rupture Testing

Figure 37. Photograph of Dogbone Specimen Used For Tension and Creep Rupture Testing

4.4 Test Matrix For Subelements

In order to investigate and scope out the nature of damage initiate and growth in the dovetail attachment section, it was decided that the test matrix would incorporate multiple load profiles. These loading profiles would include monotonic tension, stepped tension, stepped fatigue, fatigue, and fatigue in a burner rig. The test matrix is summarized in Table 8. It is acknowledged that there are essentially no repeats. Therefore, this study was intended to scope out the types of damage that occurs under different types of loading conditions, and if warranted, future studies could focus more on specific loading conditions and conduct many more repeat tests.

Table 10. Subelement Test Matrix

Test Type	Temperature	Number of Tests	Instrumentation
Tension	RT	1 (15-543)	DIC, AE, extensometer
Stepped Tension	RT	1 (15-542)	DIC, AE, extensometer
Stepped Fatigue	RT	1 (15-544)	DIC, AE, extensometer
Fatigue	RT	3 (15-545, 15-548, 15-550)	DIC, AE, extensometer
Fatigue, Burner Rig	600°C, 800°C, 1000°C	4 (15-547. 15-541. 15-546. 15-457)	FLIR, DIC, Extensometer

Each test was selected to produce a specific type of information about how damage progresses in the subelement with respect to a specific type of loading. Often, it was only after each test was completed that the next test was fully identified. The rational for each of the tests will now be described.

The first test selected was a monotonic tension test. This test would be run to failure at room temperature while recording DIC, AE, and axial strain using an extensometer that was mounted on the straight sided stem of the subelement. The objective would be to identify at what stress levels damage initiated in the attachment area, and when damage initiated in the stem. The primary damage was projected to be interlaminar cracks. Once damage was initiated, it would be critical to track the development and growth of interlaminar cracks, and document how they grew and coalesced. In addition, it was important to document the failure process as well as the fracture path morphology

The monotonic tension test was followed by a stepped tensile test at room temperature where the specimen was sequentially loaded and unloaded to higher and higher loads until the subelement failed. The unloading was very important as it provided a record of permanent deformation. It also allowed for the documentation of both elastic and inelastic deformation.

The next test was a stepped fatigue test at room temperature. This test started at a relatively low stress level that was predicted to be well below the PL stress for the stem as well as well below the ILS and ILT strengths in the attachment region. The subelement would be fatigue loaded at 5 Hz for a block of 10,000 cycles. If the specimen survived the 10,000 cycles, the stress level would be increased and another block of 10,000 cycles would be applied. This process was repeated until the subelement failed. The objective was to identify at what stress level damage first initiated during fatigue loading, and if this damage quickly stabilized or continued to grow during the block of 10,000 cycles. Damage development was monitored using AE and DIC. Stress levels that produced damage would be compared back to the monotonic tension test to see how fatigue loading influenced damage initiation and growth. Equally important was to document the fatigue failure mode and fracture morphology and compare that to the failure mode identified during the monotonic loading test.

Stepped fatigue data was used to select a stress level for continual fatigue loading at room temperature. A stress level was identified that was high enough to initiate ILT damage in the dovetail of the subelement. The goal was to fatigue the specimen for several hundred thousand cycles and track both the attachment area and the stem and monitor for damage accumulation and growth. A total of three room temperature fatigue tests were performed.

Burner rig testing at elevated temperature followed the room temperature testing. The first test were conducted at a temperature of 800°C and 200 MPa. This temperature was selected as it represents the projected temperature the attachment region would see when the airfoil was at the highest temperature. However, this specimen failed in the straight sided shank region of the subelement because of intermediate temperature embrittlement (ITE

Because of the ITE induced failure, the next test was conducted at 600°C and the stress level was kept at 200 MPa. This specimen ran fine and failed in the attachment region.

The third test was also conducted at 600°C and the applied stress level was reduced to175 MPa. The goal was to run longer than the first test at 600°C, and interrupt the test at 1000 cycles. From prior testing it had been determined that 1000 cycles was a sufficient amount of cycles to stabilize any matrix cracking. This test ran fine and was stopped at 1000 cycles. The subelement was taken back to the servo-hydraulic test laboratory, coated with a DIC speckle pattern, and loaded at room temperature to 175 MPa for one cycle to document matrix damage. The specimen was then sectioned and mounted, polished, and imaged to document matrix cracking.

The fourth and final burner rig test was conducted at 1000°C and 175 MPa, and the specimen was loaded for only one cycle. The goal was to introduce the most severe thermal gradient possible, and only loading for one loading cycle resulted in the subelement to remaining intact. The subelement taken back to the servo-hydraulic test laboratory, coated with a DIC speckle pattern, and loaded and unloaded to 175 MPa at room temperature to document matrix damage. The specimen was then sectioned, mounted, polished, and imaged to document cracking compared to the specimen that was tested at 600°C for 1000 cycles.

4.5 Design of Subelement Test Specimen

Considerable effort went into designing the subelement test specimen for this investigation. The primary requirement was to balance the required load to introduce interlaminar cracks to the maximum extent possible in the dovetail attachment region with the strength (and fatigue limit) of the straight sided stem. The UTS of this CMC is approximately 280 MPa, so design of the straight sided stem of the subelement test specimen was dictated by this value. In addition, the required axial load should not exceed the capabilities of the servo-hydraulic test frame as well as the limits of the wedge grips. The objective was to minimize in-plane stresses while maximizing interlaminar stresses in the dovetail.

A python script was used to perform parametric study on key subelement test specimen dimensions in Abacus. The exact layup of the plies was taken into account and modeled in the FEA analysis as is shown in Figure 38. As shown in the figure, the continuous plies were individually meshed as were the CMC inserts used to create the dovetail section of the subelement test specimen. A schematic of the dovetail attachment region of the subelement test specimen is shown in Figure 39 and identifies the location of the dovetail contact region, the transition radius, and the dovetail angle.

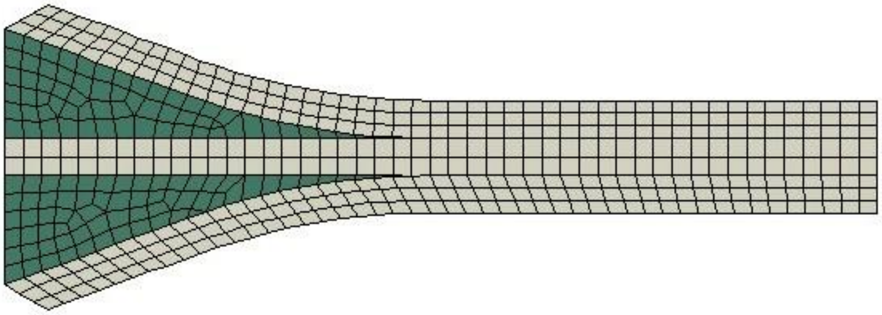

Figure 38. Finite Element Analysis Mesh Used To Analyze Subelement Test Specimen

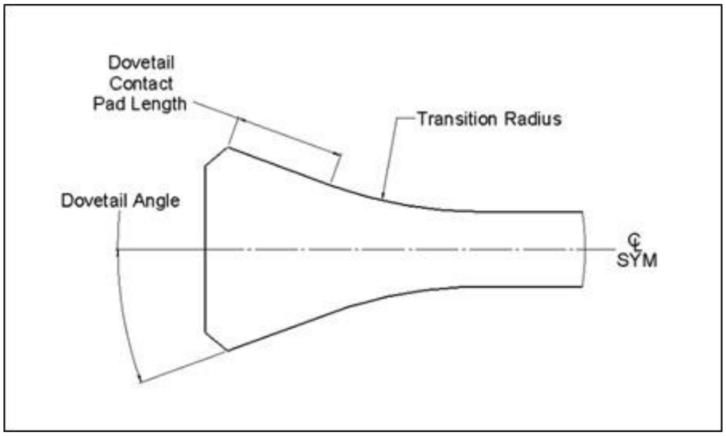

Figure 39. Schematic Of Dovetail Section of Subelement Test Specimen

The parameters that were changed were the transition radius and angle of the dovetail attachment, along with the thickness and width of the stem. The first step was to fix the dovetail angle at 20° and change the transition radius from 1.5 to 0.125. The σ_{11} stresses for a radius of 1.5 inches and 0.125 inches is shown in Figure 40 while the in-plane stresses are shown in Figure 41. A total of six different radius values were analyzed, and the resulting ILT stresses are shown in Figure 42. As the radius decreases, the ILT stresses in the dovetail section of the subelement test specimen increase and emanate from the inside the subelement test specimen at the interface between the 10 outer continuous plies and the wedge insert.

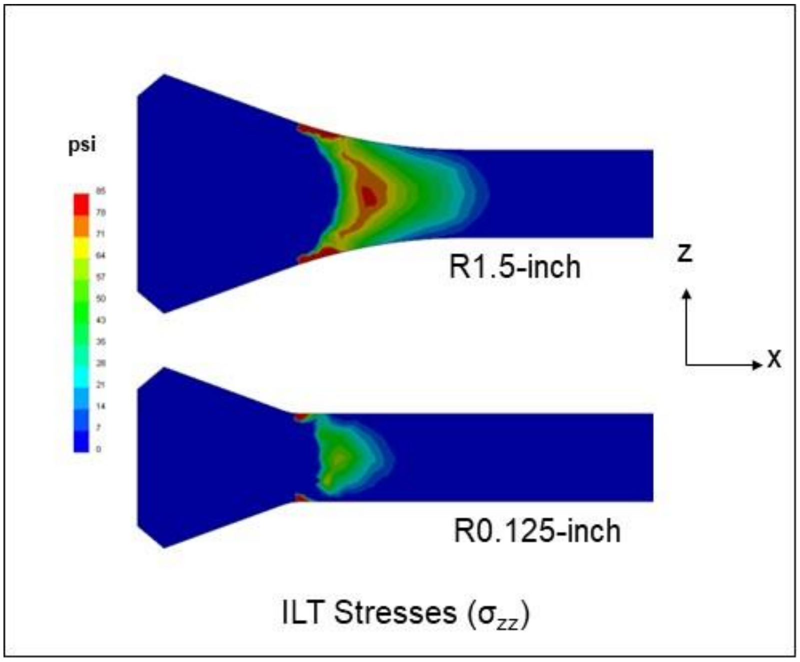

Figure 40. Schematic Showing Orientation of ILT Stresses (σ_{zz})

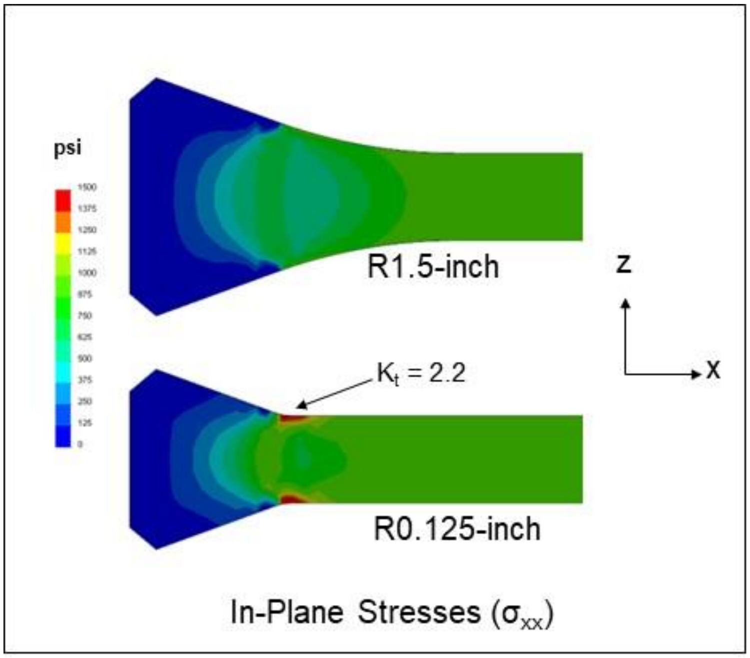

Figure 41. Schematic Showing Orientation of In-Plane Stresses (σ_{xx})

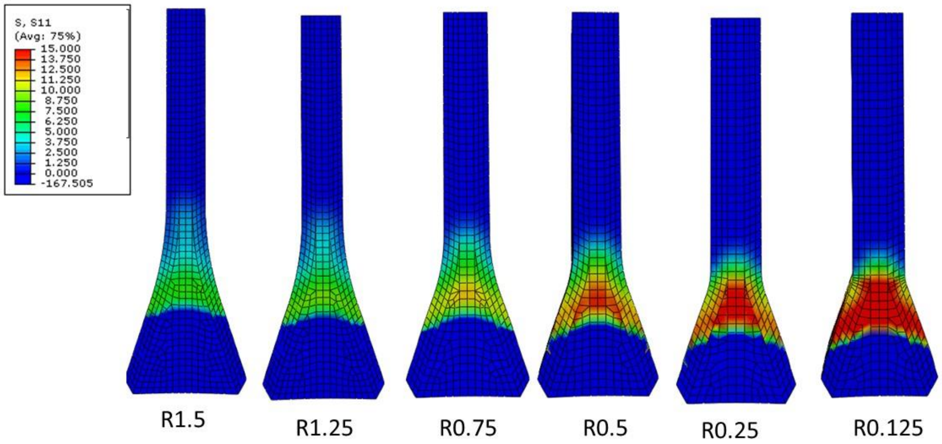

Figure 42. ILT Stress (σ_{11}) for a 20° Dovetail Angle And Various Transition Radii

The σ_{22} values for in-plane stress were also predicted for the six radius values and are shown in Figure 43. In this figure one can see that as the transition radius decreases, the higher stresses appear to emanate from both the transition radius and fixture contact.

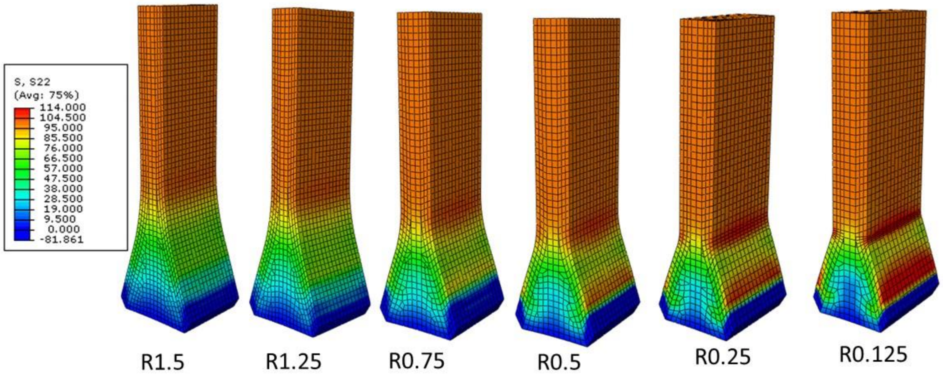

Figure 43. In-Plane Stress (σ_{22}) for a 20° Dovetail Angle And Various Transition Radii

The next step was to study angles between 20° and 35° while keeping the radius at 0.75. The analysis showing the ILT stresses (σ_{11}) for six different angles is shown in Figure 44. As the angle increases, the higher stresses appear to emanate from the outside near the fixture contact.

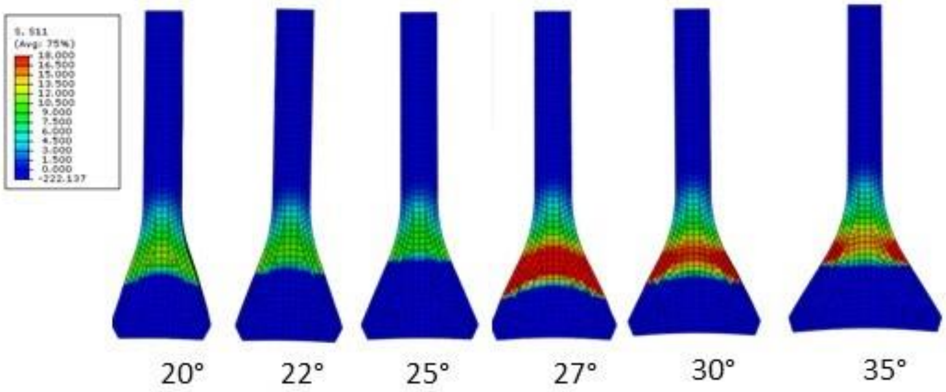

Figure 44. Interlaminar Tensile Stress (σ_{11}) for Increase Dovetail Angle With Constant Transition radius of R0.75

Analysis was performed keeping the angle constant and varying the radius. Figure 45 shows how the ILT stresses (σ_{11}) change as the radius is changed from 1.5 inches down to 0.125 inches. Increasing the radius increases the stress in the region near the transition region where the dovetail and straight sided stem meet.

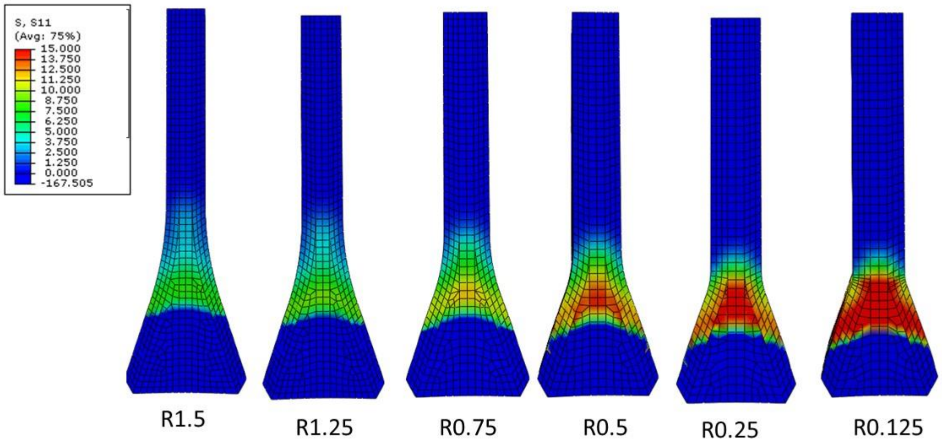

Figure 45. Interlaminar Tensile Stress (S11) For a 30° Dovetail Angle With Various Radii

A substantial amount of analysis was performed to optimize the transition radius and dovetail angle of the subelement test specimen. These multiple analysis runs indicated that when the dovetail angle is greater than 20°, the highest stress levels appear to emanate from the fixture contact point. A decrease in the transition radius generates a stress concentration in the transition radius region. A dovetail angle of 30° with a transition radius of 0.5 or 0.25 seems to be the best options. The results from multiple analysis runs are presented in Table 9.

Table 11. Results of Parametric Study of Subelement Test Specimen Design

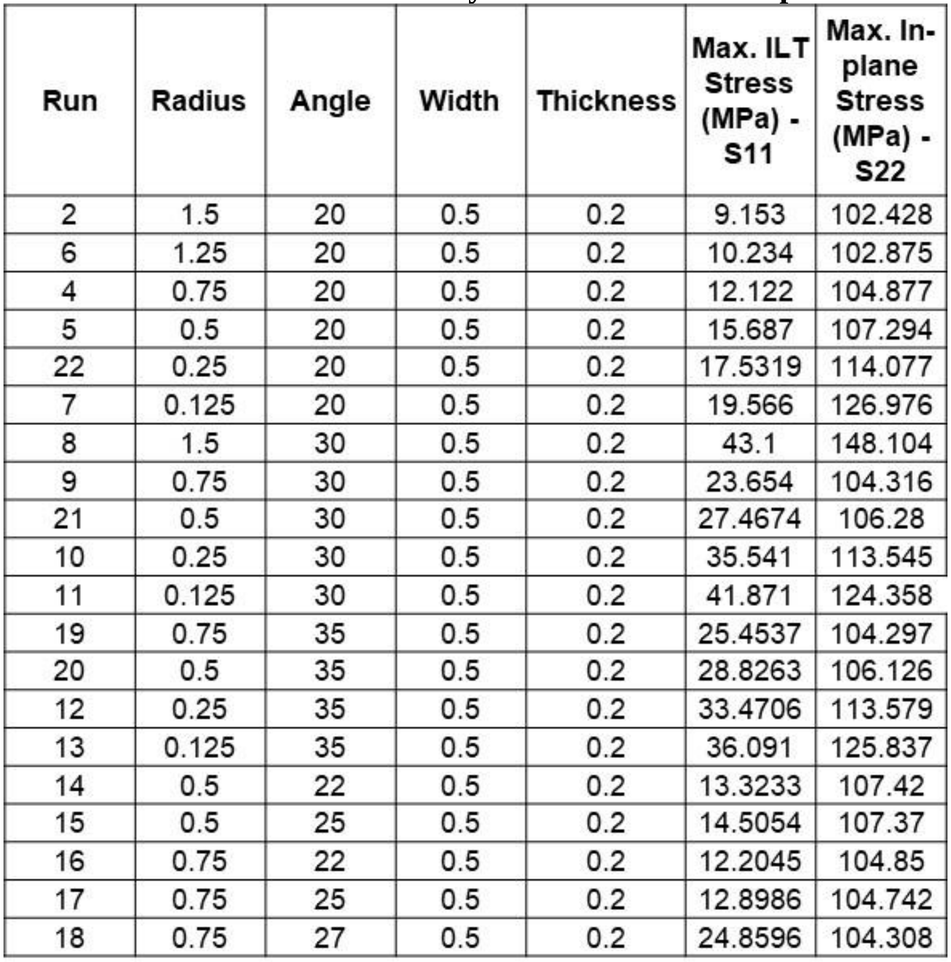

Run	Radius	Angle	Width	Thickness	Max. ILT Stress (MPa) - S11	Max. In-plane Stress (MPa) - S22
2	1.5	20	0.5	0.2	9.153	102.428
6	1.25	20	0.5	0.2	10.234	102.875
4	0.75	20	0.5	0.2	12.122	104.877
5	0.5	20	0.5	0.2	15.687	107.294
22	0.25	20	0.5	0.2	17.5319	114.077
7	0.125	20	0.5	0.2	19.566	126.976
8	1.5	30	0.5	0.2	43.1	148.104
9	0.75	30	0.5	0.2	23.654	104.316
21	0.5	30	0.5	0.2	27.4674	106.28
10	0.25	30	0.5	0.2	35.541	113.545
11	0.125	30	0.5	0.2	41.871	124.358
19	0.75	35	0.5	0.2	25.4537	104.297
20	0.5	35	0.5	0.2	28.8263	106.126
12	0.25	35	0.5	0.2	33.4706	113.579
13	0.125	35	0.5	0.2	36.091	125.837
14	0.5	22	0.5	0.2	13.3233	107.42
15	0.5	25	0.5	0.2	14.5054	107.37
16	0.75	22	0.5	0.2	12.2045	104.85
17	0.75	25	0.5	0.2	12.8986	104.742
18	0.75	27	0.5	0.2	24.8596	104.308

The following dimensions were selected for the subelement test specimen after completing multiple analysis runs in order to maximize ILT stresses in the dovetail section of the subelement test specimen. The transition radius was set at 38.1 mm (1.5”) while the dovetail angle was selected to be 30°. For the stem region of the subelement test specimen the width was selected to be 12.7 mm (0.5”) while the thickness was 5.08 mm (0.2”). A schematic drawing of the attachment region is shown in Figure 46 and a detailed machining drawing of the subelement test specimen is shown in Figure 47.

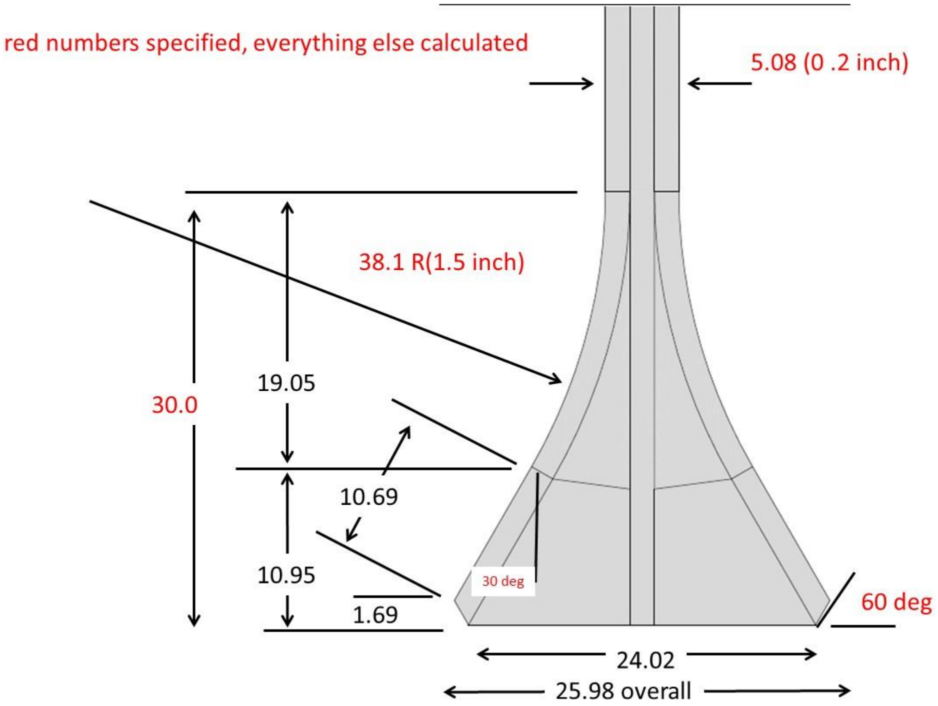

Figure 46. Schematic Drawing of Dovetail Attachment Region Of Subelement Test Specimen

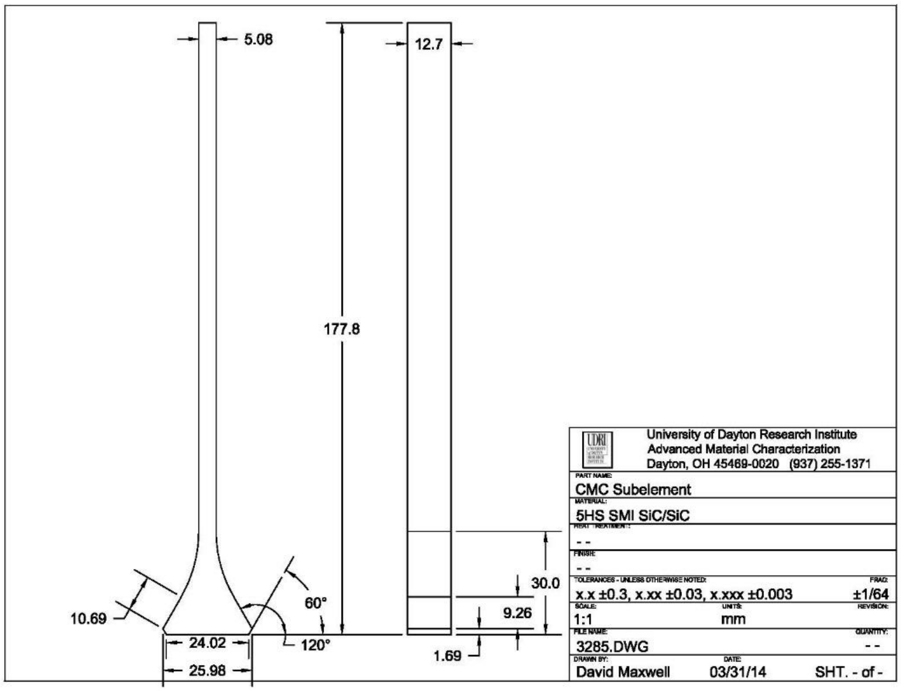

University of Dayton Research Institute
Advanced Material Characterization
Dayton, OH 45469-0020 (937) 255-1371

PART NAME: CMC Subelement
MATERIAL: 5HS SMI SiC/SiC
HEAT TREATMENT: - -
FINISH: - -
TOLERANCES - UNLESS OTHERWISE NOTED: x.x ±0.3, x.xx ±0.03, x.xxx ±0.003
FRAC: ±1/64
SCALE: 1:1
UNITS: mm
REVISION:
FILE NAME: 3285.DWG
QUANTITY: - -
DRAWN BY: David Maxwell
DATE: 03/31/14
SHT. - of -

Figure 47. Machining Drawing Of Subelement Test Specimen

Once the dimensions were selected and finalized, the complete analysis was run for that specific design. The in-plane stress (σ_{11}) analysis is shown in Figure 48. The interlaminar shear stress (σ_{13}) analysis is shown in Figure 49 and appear to be highest at the surface contact region of the dovetail section of the subelement test specimen. A plot of shear stress versus applied stress is shown in Figure 50. Also shown on the plot is the actual measured shear strength for this CMC as measured using DNC test specimens. From the figure one can observe that the specimen should never experience shear failure. The interlaminar tensile stress analysis (σ_{33}) is shown in Figure 51. One can clearly observe that there are high ILT stress values in the dovetail and these originate between the 10 continuous outer plies and the wedge insert. A plot of interlaminar tensile stress as a function of applied load as shown in Figure 52. Also shown on this plot is the measured ILT strength for this CMC as measured using round ILT test specimens. It is clear that ILT cracking should initiate once an applied stress of 90 MPa reached.

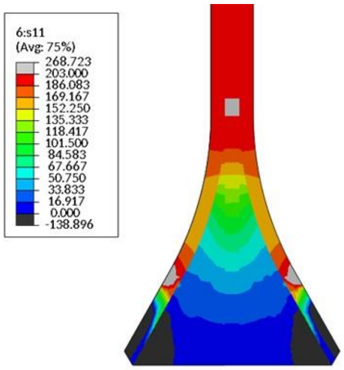

Figure 48. In Plane Tension Stress (σ_{11}) For Subelement Test Specimen

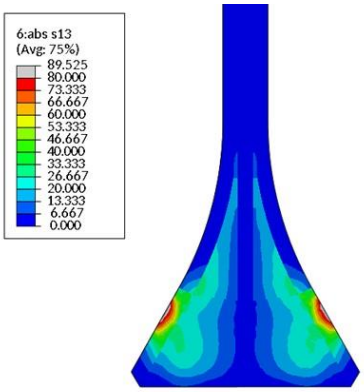

Figure 49. Interlaminar Shear Stress (σ_{13}) For Subelement Test Specimen

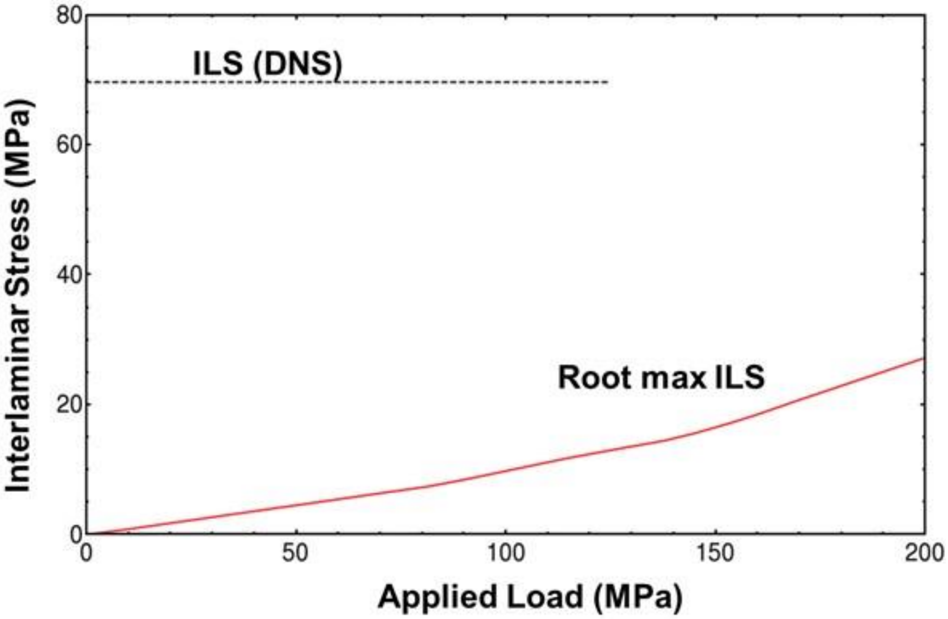

Figure 50. Plot of Interlaminar Shear Stress (σ_{13}) As A Function of Applied Load

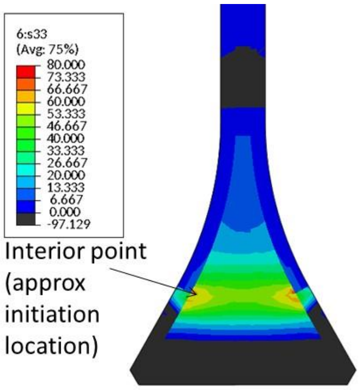

Figure 51. Interlaminar Tension Stress (σ_{33}) For Subelement Test Specimen

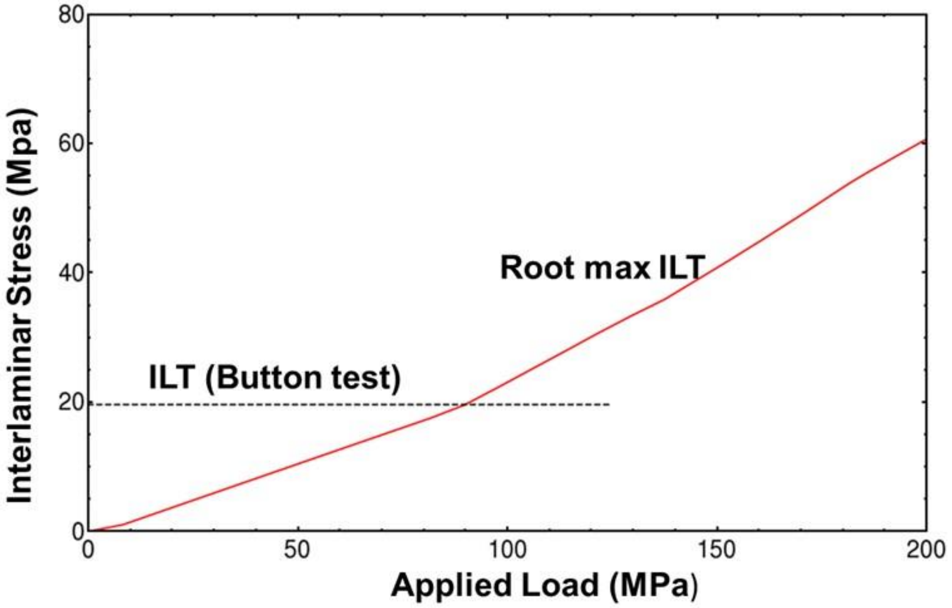

Figure 52. Plot of Interlaminar Tensile Stress (σ_{33}) As A Function of Applied Load

4.6 Manufacturing Of Subelement Test Specimens

As stated above, a generic turbine blade subelement test specimen featuring a dovetail attachment was specifically designed for this study by the testing team. This subelement utilized continuous plies that transitioned from a thick dovetail attachment section to the thinner stem section of the subelement and was specifically designed to develop high ILT stresses in the dovetail section

The subelement panel preform was made using a symmetric layup. Ten continuous plies make up the outer layer on the top and bottom of the panel, while ten continuous plies transverse straight from the stem section of the subelement into the dovetail section. Pre-machined wedge inserts were placed between the middle and top plies, and between the middle and lower plies to create the dovetail section of the subelements. These wedge inserts were made by stacking up a large number of plies. This preform what then partially densified by CVI first with the fiber coating and then with SiC. The wedges were then machined to shape. A schematic of how the plies in the panel were distributed along with the location of the filler wedge is shown in Figure 53. The panel was then densified using standard processing. As stated earlier, the finished panel passed NDI with no sign of any delaminations in the scans. After final processing, the panel was machined down the centerline as shown in Figure 53, and then each half was machined into five 12.7 mm wide subelement test specimens. A total of 10 subelement test specimens were manufactured. A schematic showing the finished dovetail section of the subelement test specimen is presented in Figure 54.

The finished subelement test specimen contained 30 continuous plies in the stem region. These plies ran the continuous length of the subelement test specimen. At the beginning of the dovetail attachment region, 10 plies curved and formed the contact area on each side of the dovetail attachment region, and the 10 center plies continued straight down into the center of the dovetail attachment region. The remaining area of the attachment region was made up of the wedge inserts that were added to the stack-up of plies. An optical micrograph showing the edge of the dovetail attachment region of an as-manufactured subelement test specimen is shown in Figure 55, while a photograph of an as-manufactured subelement test specimen is shown in Figure 56. It is important to note that the complexity of the subelement dovetail attachment architecture (i.e. ply drops, curved plies, etc.) did not contribute to additional porosity. It is also important to again specify that this is a generic design intended to promote high ILT stress levels in the dovetail section of the subelement test specimen and does not represent any actual CMC airfoil fiber architecture.

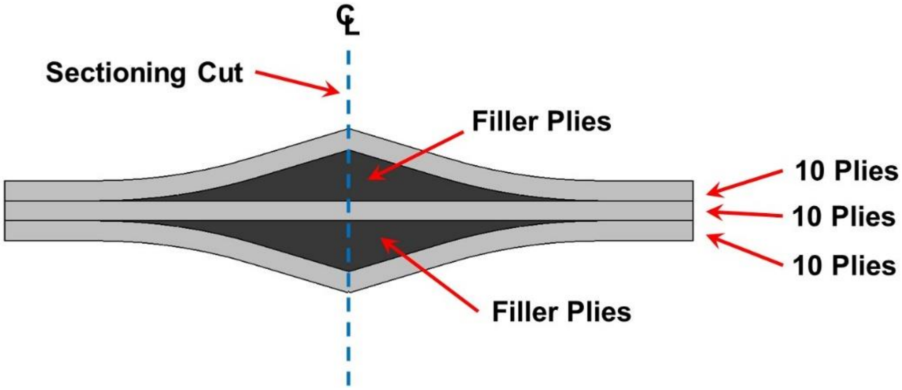

Figure 53. Schematic Diagram Of How Subelement Panel Was Constructed

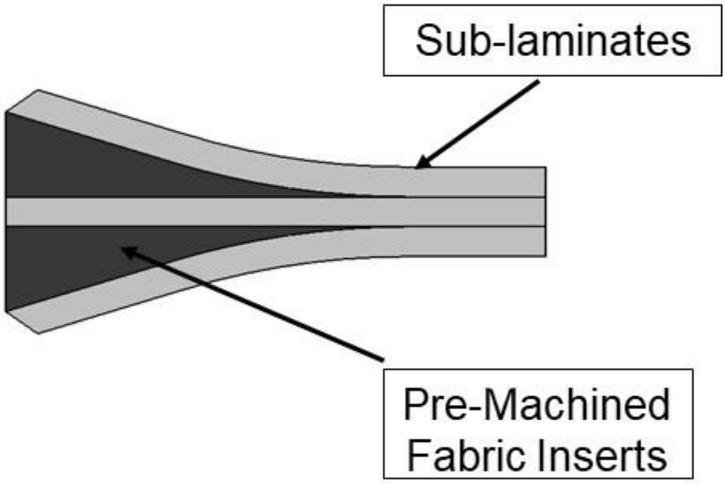

Figure 54. Schematic Showing How Dovetail of Subelement Test Specimen Was Constructed And Machined

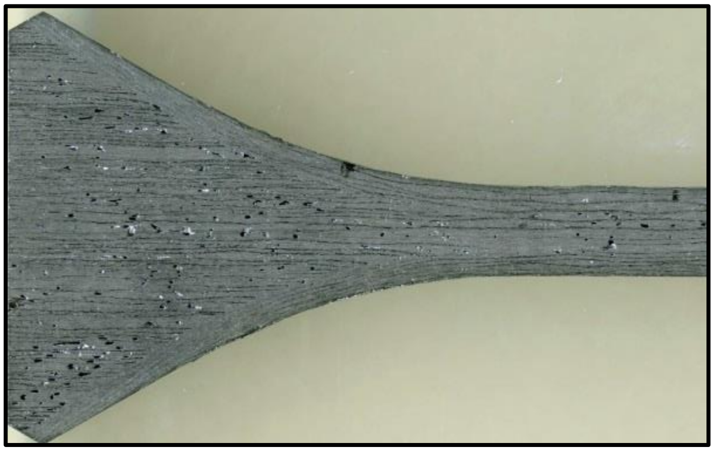

Figure 55. Optical Image of Dovetail Section Of Subelement Test Specimen

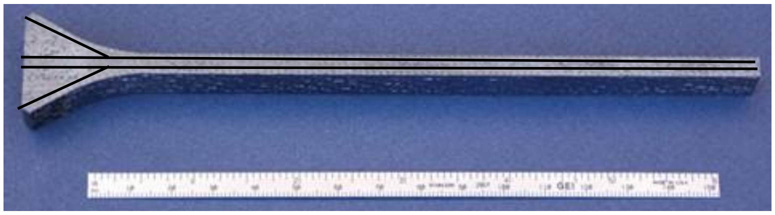

Figure 56. Optical Photograph Of An As-manufactured Subelement Test Specimen

5. TEST RESULTS

5.1 Baseline Test Results

5.1.1 DNC

DNC shear tests were conducted on specimens machined from the flat panel. The tests were conducted at room-temperature to measure the interlaminar shear (ILS) strength of the CMC material. Only three tests were conducted, and the results are listed in Table 10. The average shear strength was measured to be 69.6 MPa and ranged from a high of 72.68 MPa to a low of 60.63 MPa. A stress vs time trace for specimen 15-396 is shown in Figure 57.

Table 12. Results From the DNC Tests On SMI SiC/SiC

AFRL Specimen ID	Test Type	Test System	Test Date	Gage Width (mm)	Gage Thick (mm)	Area (mm^2)	P_{max} (N)	S_{max} (MPa)	Ex (GPa)	ef (%)	Temp (°C)	Time (hr)	Cycle Count	Failure LC/ACT mm
DNS TESTS														
15-395	DNS	SH44	12/30/15	15.015	2.677	90.090	-6548	-72.68	---	---	RT	---	---	between notches
15-396	DNS	SH44	12/30/15	15.013	2.688	90.078	-6811	-75.62	---	---	RT	---	---	between notches
15-397	DNS	SH44	12/30/15	15.013	2.751	90.078	-5453	-60.63	---	---	RT	---	---	between notches

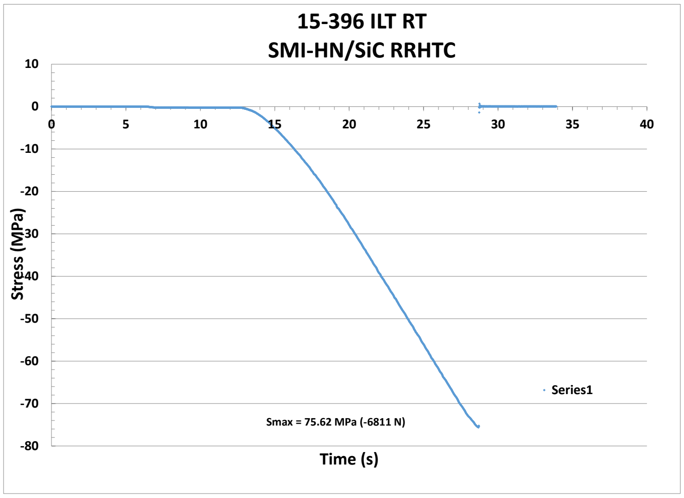

Figure 57. Stress Versus Time For A Room Temperature Double-Notch Compression Test On SMI SiC/SiC

DIC was used to measure surface strain on the specimen to so strains between the notches. High magnification images were recorded from the 2-D DIC. The DIC strain maps also confirmed that failure initiated at the notches and progressed along the centerline of the DNC test specimen. Several strain maps that were generated for different load levels during one of the tests are shown in Figure 58. Not much could be learned from those strain maps because of the limited resolution

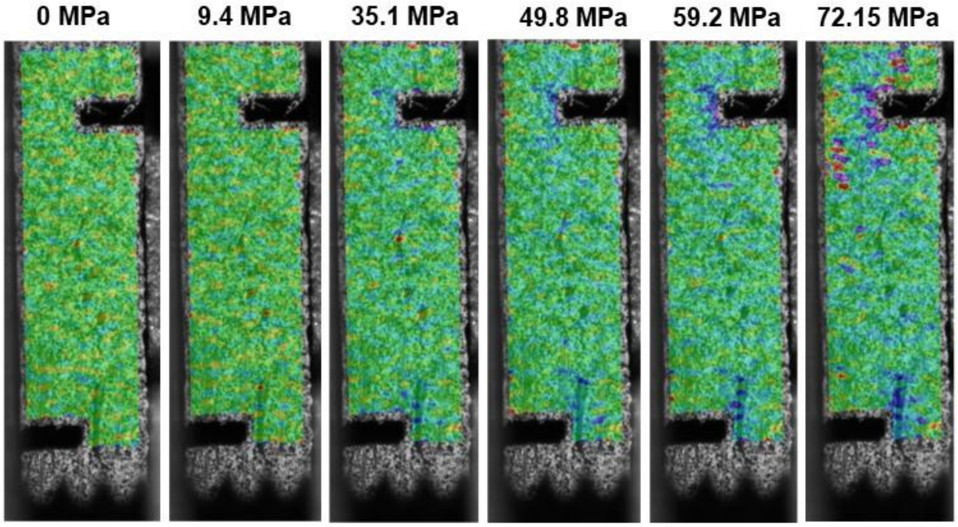

Figure 58. DIC Strain Maps for DNC Test on SMI SiC/SiC

5.1.2 ILT

ILT tests were run on test specimens machined from the flat panel. The specimens were 25.4 mm in diameter and the tests were run at room-temperature to measure the interlaminar tensile strength of the material. The results are listed in Table 11. The ILT strength values obtained were 18 and 21 MPa, for an average of 19.5 MPa.

Choi [14] has reported that after analyzing ILS and ILT test results from many different CMC systems that they exhibit a ration of approximately 3:1. The data from this research is plotted in a plot of ILS versus ILT alongside data that Choi has gathered from a large number of other CMC systems. The plot is presented in Figure 59 and shows that the current CMC system used in this study also exhibits the same ration. It was reassuring that the ILT and ILS data generated during this study followed the same ration as so many other CMC systems.

Table 13. Results From The ILT tests

AFRL Specimen ID	Test Type	Test System	Test Date	Gage Width (mm)	Gage Thick (mm)	Area (mm^2)	P_{max} (N)	S_{max} (MPa)	Ex (GPa)	ef (%)	Temp (°C)	Time (hr)	Cycle Count	Failure LC/ACT mm	Comments
ILT TESTS															
15-404	ILT	SH44	11/4/16	25.465	2.762	509.304	9173	18.01	51.14	~0.0382	RT	---	---	1/15 plys	with 0.5" extemsometer & DIC
15-405	ILT	SH44	11/4/16	25.455	2.731	508.904	10807	21.24	65.55	~0.0333	RT	---	---	1/15 plys	with 0.5" extemsometer & DIC

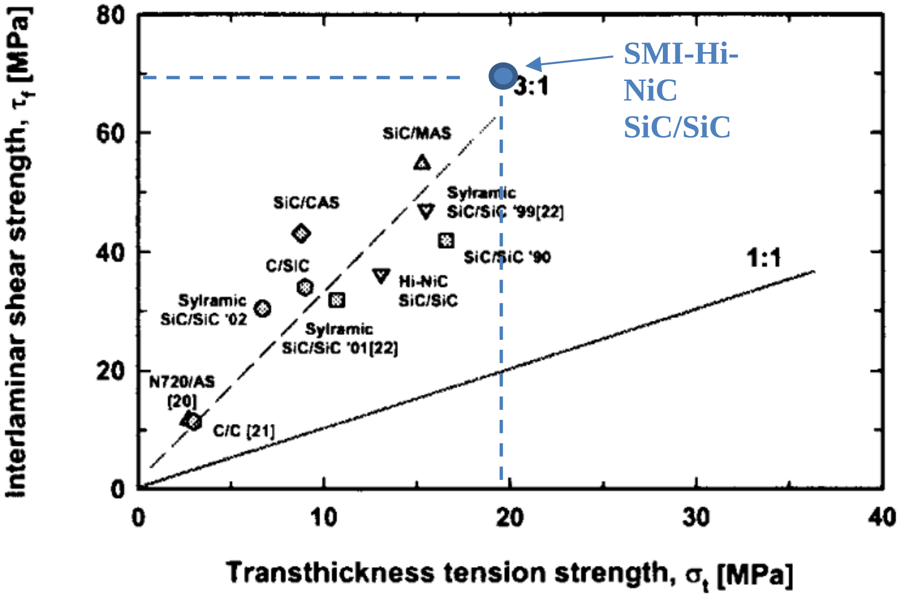

Figure 59. CMCs Exhibit a 3:1 Ratio of ILS to ILT Strength [14]

As part of an experiment, these tests were set up with a MTS knife edge extensometer as well as with a speckle pattern and a camera for DIC analysis to demonstrate if strain data could effectively be captured during an ILT test. Figure 60 shows an optical photograph of the ILT test setup. A 12.7 mm” gage length extensometer was used to measure displacement in an attempt to determine if a through thickness modulus value could be calculated. However, even this short 12.7 mm gage length included the CMC test specimen, two layers of the FM1000 adhesive used to bond the button specimen to the steel pull-fixtures, and a few mm of the steel fixtures. Calculation of an ILT modulus using this strain data was therefore not possible as the strain versus load data was not usable. The DIC data was also very difficult to interpret, as the noise in the data was of equal magnitude to the displacements being measured. This was further complicated by the small field of view in focus (due to the round specimen) and the relatively large size of the speckle pattern. Therefore, no useful data was generated by the DIC measurement technique.

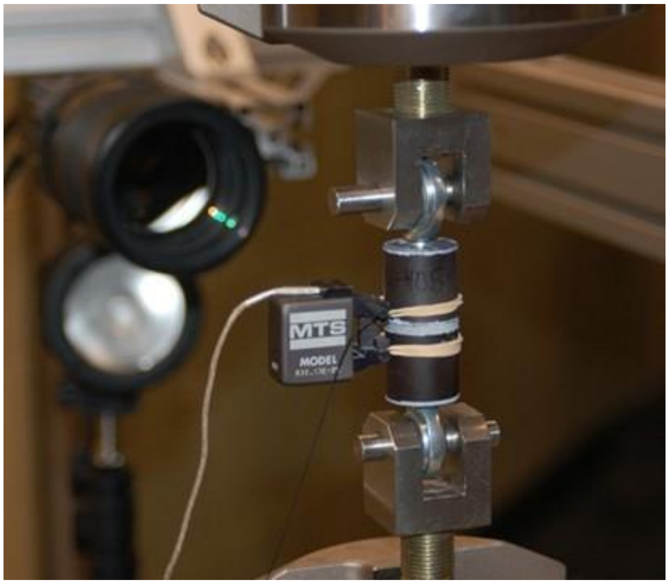

Figure 60. Photograph of Test Set-up For Room Temperature ILT Test on SMI SiC/SiC

5.1.3 Tension

Tensile properties were measured on dogbone specimens at room-temperature, 800°C, and 1200°C. Only one test was conducted at each temperature. The results are listed in Table 14, and a plot of stress versus strain for all three temperatures is presented in Figure 61. It is acknowledged that only one test at each temperature limits what can be interpreted from the results. However, some general observations in mechanical behavior as related to test temperature can be made even with this limited data set.

The Ultimate Tensile Strength (UTS) rose approximately 12 % at 800°C and then basically decreased back to the room temperature strength. There was no measurable change in stiffness as a function of temperature for the three temperatures investigated. The proportional limit rose only slightly at 800°C and then decreased 19% at 1200°C. Strain to failure also remained constant at 800°C and decreased 37% at 1200°C.

It is suggested that the increase in the UTS at 800°C may be attributed to a reduction in the residual stress state in the CMC that remains after high temperature processing. This is often observed in SiC/SiC CMCs. No change in stiffness at 800°C is typical of this class of CMCs and is attributed to the constituents that make up the CMC. Neither the fiber nor the matrix soften at these temperatures. It is important to note that at 1200°C both the PL and strain to failure did decrease significantly. The drop in PL suggests that changes in the residual stress state have now significantly relaxed resulting in matrix cracking at much lower stress levels. The loss in strain to failure indicates a loss in toughness, which is a clear indication that oxidative degradation has influenced failure even for such a short term test. Fracture surfaces will be discussed after the creep rupture data is presented.

Table 14. Tensile Properties for SMI SiC/SiC

Sample ID	Temperature (°C)	UTS (MPa)	Modulus (GPa)	PL (MPa)	ef (%)
15-387	RT	286	249	134	1.010
15-392	800	320	235	140	1.117
15-390	1200	274	254	113	0.693

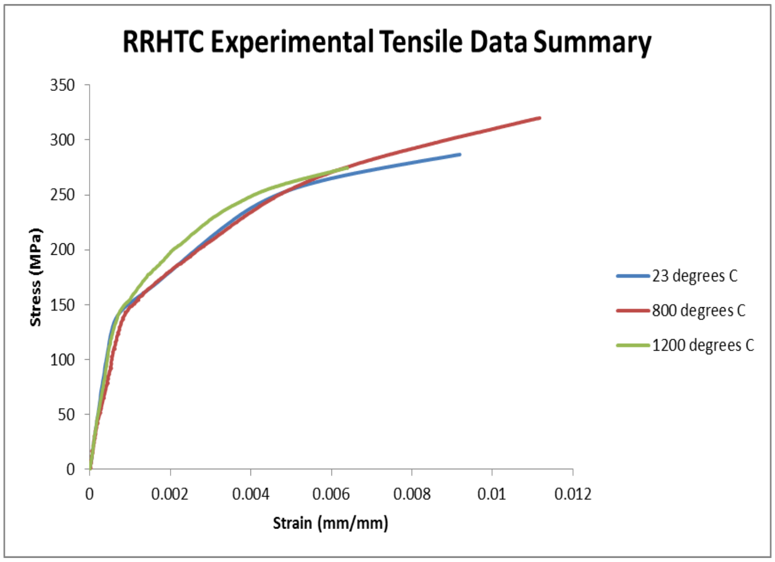

Figure 61. Tensile Behavior of SMI SiC/SiC At Three Temperatures

5.1.4 Creep Rupture Testing In A Furnace

A single creep test was performed on a dogbone specimen at a temperature of 1200°C and a stress of 175 MPa using a standard box furnace and servo-hydraulic test frame. The specimen failed after only 39 minutes of sustained load after accumulating roughly 0.22% strain. The strain to failure is significantly less than the tension test, and indicates that severe oxidative degradation has occurred. A plot of the total creep strain versus time is presented in Figure 62. Stress versus strain was recorded during the initial load-up to 175 MPa. A comparison of strain during loading to 175 MPa for the creep rupture test is compared to the tension test at 1200°C in Figure 63. Both tests were loaded at 10 MPa/s and they display identical behavior up to the stress of 175 MPa. Modulus and proportional limit values were nearly identical between the creep rupture test and the tension test indicating excellent reproducibility in stress-strain behavior at 1200°C.

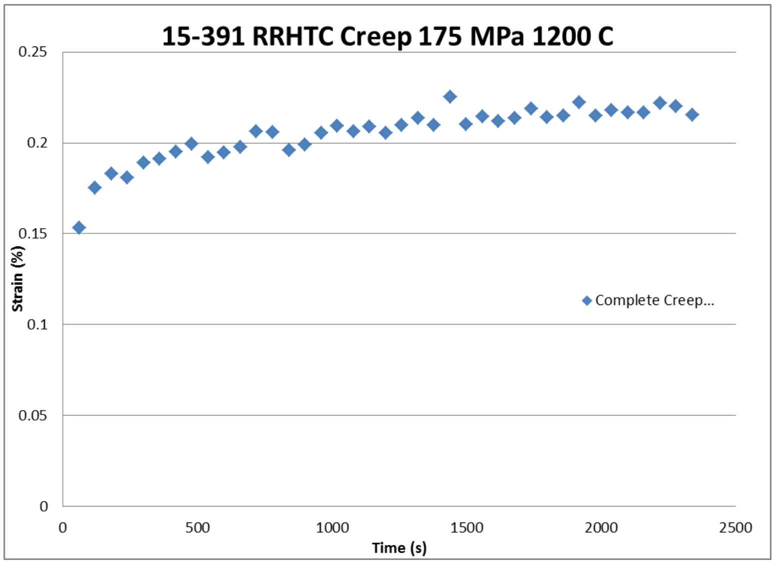

Figure 62. Creep strain vs time for SMI-SiC/SiC made by RRHTC

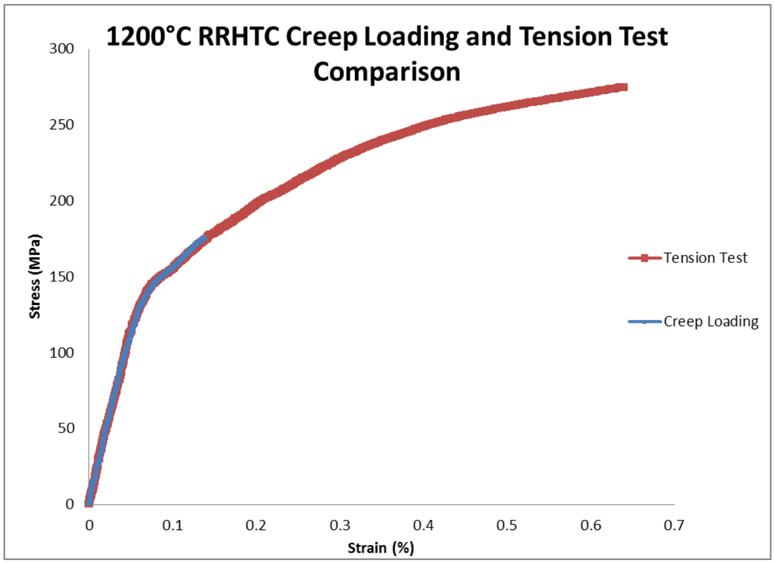

Figure 63. Stress-Strain Behavior for Loading Portion Of The Creep Rupture Test Compared to Monotonic Tensile Test For SMI SiC/SiC at 1200°C

5.1.5 Microscopy of Fracture Surfaces

The creep rupture tested specimen failed in a very short period of time, and this early failure was likely the result of rapid oxidation embrittlement. Optical photographs of the failed test specimens for the two elevated temperature tension tests and the creep rupture test are presented in Figure 64. High higher magnification optical images of the failure region are presented in Figure 65. The specimen tension tested at 800°C shows slight discoloration in the heated zone, failure within the gage section, and evidence of fiber and fiber tow pull out. The specimen tension tested at 1200°C also shows evidence of fiber pull out, but has more discoloration (oxidation) on the surface in the hot zone of the specimen and its failure occurred right at the transition from the gage section to the radius. The specimen tested under sustained load creep rupture at 1200°C (at ~ 60% of its UTS at that temperature) shows a more enhanced oxide layer on the surface in the heated zone and failure occurred well into the radius section of the dogbone test specimen. In comparison, the fracture surface is very flat, with little fiber pull out, indicative of oxidation embrittlement. A Scanning Electron Microscope (SEM) was used to study the fracture surfaces of the 1200°C tensile a creep rupture fracture surfaces. SEM mages of the fracture surfaces are presented in Figure 66. The images clearly show at low and high magnification that there is fiber pullout on the fracture surface of the two tensile specimens, but very little on the fracture surface of the creep rupture specimen. This is conclusive evidence that the creep rupture specimen experienced severe embrittlement throughout the cross section in only 39 minutes at load.

Temperature profiles for the furnace and dogbone test specimen were made before testing began and are shown in Figure 67. The temperature of the dogbone specimen is shown as a function of length from the centerline of the test specimen. One can use the failure location to identify the temperature at the location of failure. The thermal profile data shows that the creep rupture specimen failed in region where the test specimen was at a temperature of approximately 1150°C. The specimen likely failed at the transition region because of two damage mechanisms interacting together. The first is that at the beginning of the radius there are cut longitudinal fibers. These fibers create a region of shear induced matrix damage. Secondly, the entire hot section of the test specimen has severely embrittled in only 39 minutes. It is suggested that these two factors combined to cause failure at the radius in the short time period.

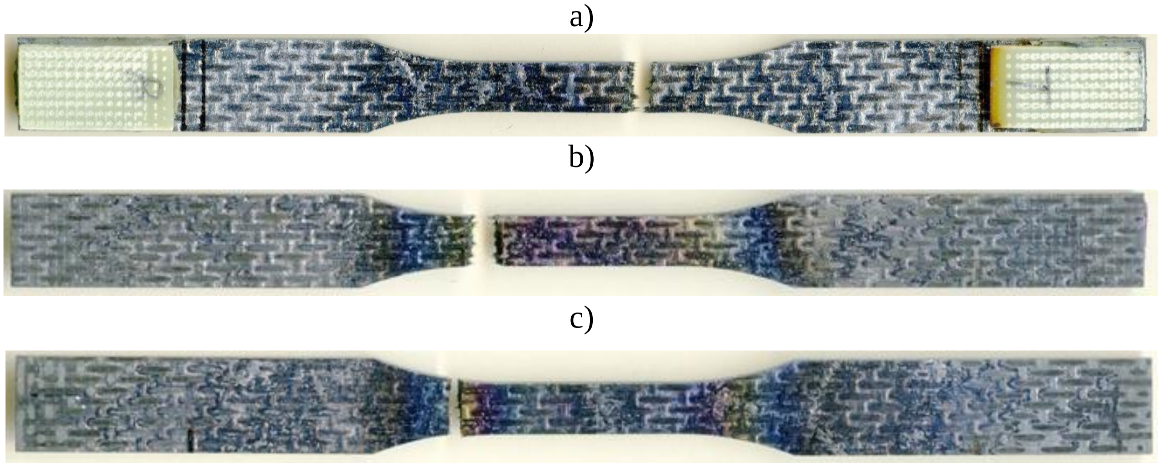

Figure 64. Photographs of Failed SMI-SiC/SiC Test Specimens: a) Tension Tested at 800°C, b) Tension Tested at 1200°C, and c) Creep Tested at 1200°C

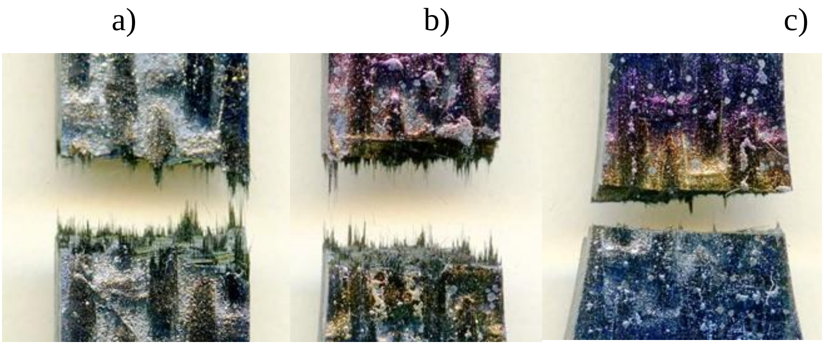

Figure 65. Optical Photographs of Specimen Fractures: a) Tension Tested at 800°C, b) Tension Tested at 1200°C, and c) Creep Tested at 1200°C

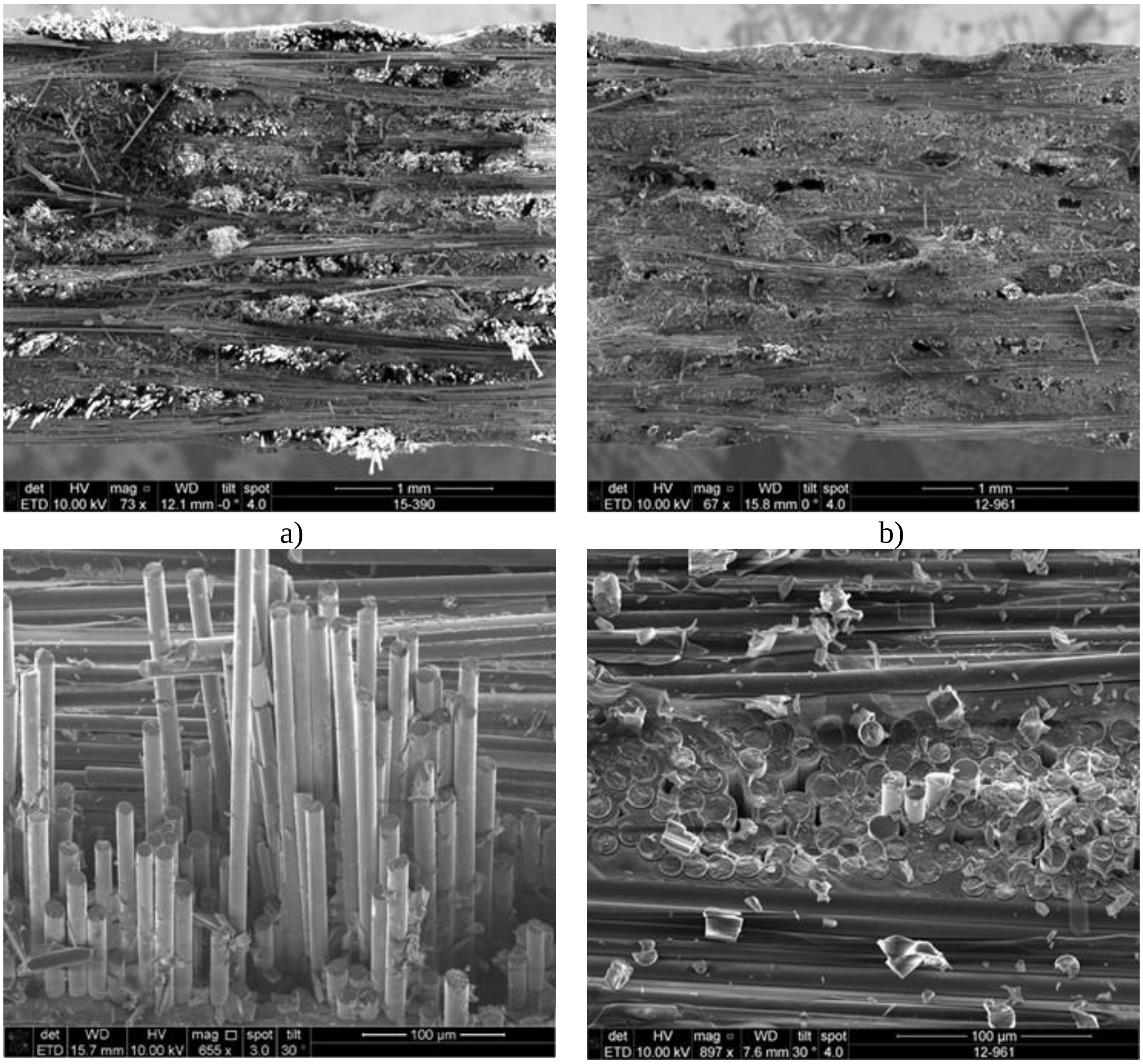

a) b)

c) d)

Figure 66. SEM Images of Fracture Surfaces for 1200°C Tensile (a) & c)) And Creep (b) & d)) Tested Specimens of SMI-SiC/SiC

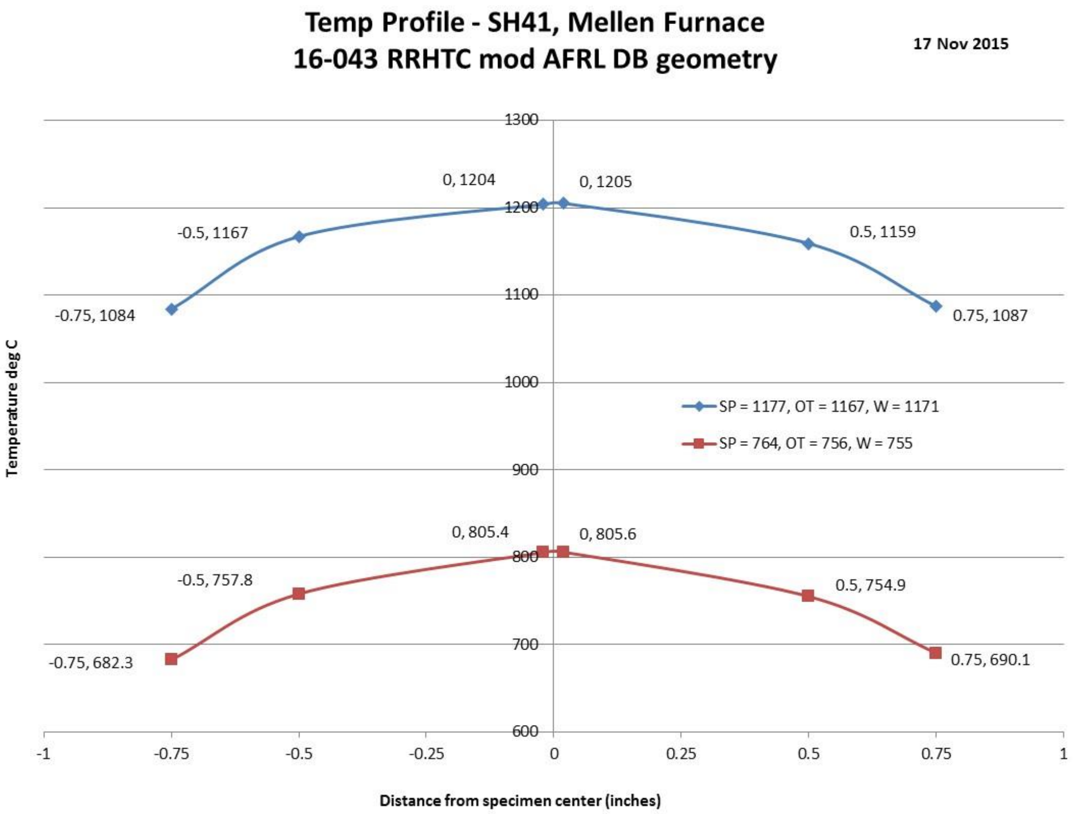

Figure 67. Temperature Profiles Measured on a SMI-SiC/SiC Dogbone Specimen At 800°C and 1200°C

5.2 Subelement Test Results

The subelements experienced complex stress states in the dovetail attachment region similar to those that would occur in actual CMC turbine blades. In addition, the dovetail section of the subelements simulated the attachment design that would be used for real CMC airfoils. These features involve continuous plies as well as ply drops. Having such features also then results in features as matrix rich regions, porosity, and regions were continuous and discontinuous plies interact. As discussed earlier, the stress values reported for subelements in the follow discussion are always the far field stresses and were calculated using the cross-sectional area of the stem section of the subelement. The resulting stress state in the dovetail region of the subelement produced a high interlaminar tensile component. For subelement testing, loading consisted of monotonic tension, stepped tension, stepped fatigue, fatigue loading, and burner rig testing.

5.2.1 Subelement Tension Test at 23°C (15-543)

To begin the study, a monotonic tension test was performed on subelement test specimen 15-543. The intent was to document stress-strain response and establish the failure mechanism. Each subelement was carefully inspected before being tested. Examples of how each subelement was inspected will now be provided. Figure 68 is an optical photograph of the subelement showing the edge of the dovetail region. There is some small porosity present and it is very small (< 0.1 mm) and well distributed. This observed porosity is of the size and distribution to the porosity that was observed in the flat panel test specimens. There no sign of any large groups of porosity, and no long stringer types of porosity. The stem of the subelement was also inspected for large scale porosity.

As stated earlier, each test specimen was CT scanned. A typical CT image of the interior of the subelement is presented in Figure 69. This CT image looks remarkably similar to the optical image taken of the edge of the test specimen. The CT scans did not reveal any large voids or delamination’s in the interior of the subelement. Of particular importance was the absence of any delamination type cracks or voids between the outer 10 continuous plies and the wedge inserts, or between the 10 middle continuous plies and the wedge inserts.

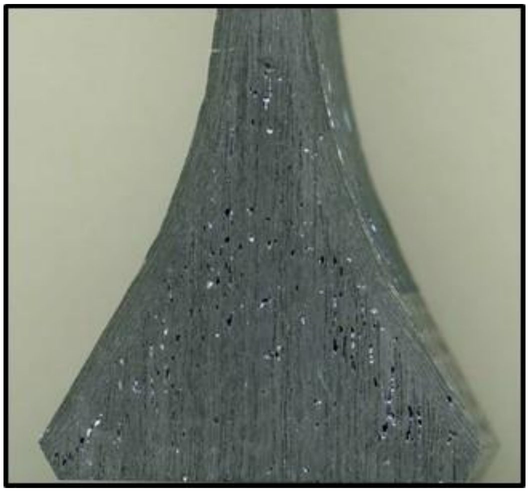

Figure 68. Optical Image Of The Dovetail Edge Of Specimen 15-453

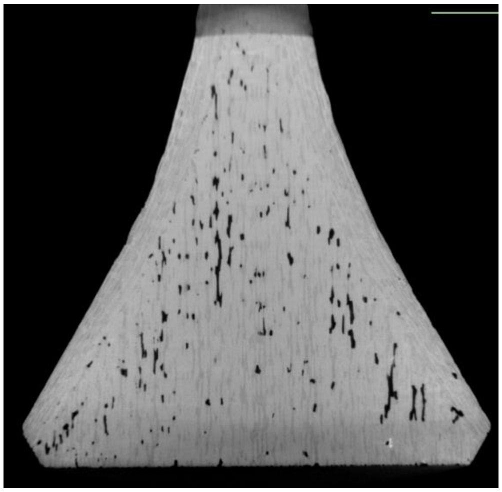

Figure 69. CT Image Of The Dovetail Interior Of Specimen 15-543

A fast fracture tension test of a subelement was performed at room temperature to fully document the stress versus strain response and to identify the failure mechanism associated with fast fracture. A plot of stress versus strain to failure for the subelement tension test specimen are presented in Figure 70. In this figure the results from the subelement tension test are compared to the stress versus strain trace from the flat dogbone tension test specimen tested at 23°C. The measured modulus of the of the subelement was measured to be 291 GPa, which is approximately 15% higher than the modulus measured in the room temperature dogbone tensile test (253 GPa). Likewise, the proportional limit for the subelement of 160 MPa was noticeably higher that the value of 134 MPa measured on the dogbone tensile specimen. The ultimate tensile strengths (UTS) of 263 MPa (subelement) and 286 MPa (dogbone) are within 10%. This is an interesting finding and likely a coincidence, as the subelement exhibited a slightly different failure mechanism compared to the dogbone test specimen. The subelement developed significant interlaminar tensile cracks in the dovetail attachment region and failed by propagation of these cracks. A significant reduction in the failure strain was seen in the subelement (0.34 %) compared to the dogbone (0.94 %) and is attributed to the different failure mechanisms.

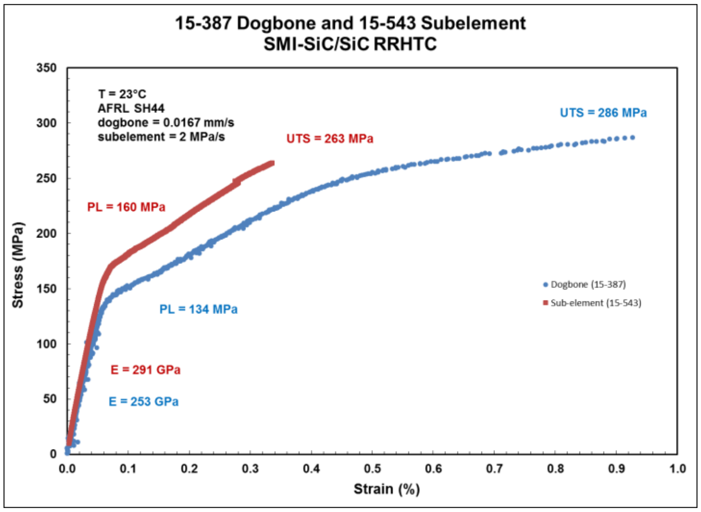

Figure 70. Tensile Behavior Of A Dogbone And Subelement at 23°C

DIC was used to monitor full field surface strain, which is sensitive to surface/near surface cracks. DIC images were continually recorded throughout the entire tension test of the subelement. These images were used to generate strain maps. Figure 71 shows a plot of the complete stress stain trace and a DIC strain map taken when the stress was at only 120 MPa, which is well below the proportional limit stress level of 160 MPa. There were no signs in the DIC strain map of any cracks. This was a bit surprising as the FEA analysis identified that the ILT stress in the dovetail would exceed the measured ILT strength of 19.6 MPa once the applied tensile stress exceeded 90 MPa. Figure 72 show the same plot and the DIC strain map taken when the applied stress was equal to the proportional limit stress of 160 MPa. There are no signs of any cracks in the DIC strain map. Figure 73 shows the same plot and the DIC strain map taken at 200 MPa. There are still no ILT cracks evident even though this stress level is substantially above the proportional limit and approximately twice the stress predicted by FEA to initiate ILT cracks (90 MPa). Figure 74 shows the tensile plot and the DIC strain map taken at 220 MPa. In this DIC strain map one can clearly see that ILT cracks have formed precisely where the FEA predicted. This location is exactly between the 10 outer continuous plies and the wedge insert. Figure 75 shows the tensile plot and the DIC strain map taken when the applied stress was 240 MPa. The initial ILT crack has grown substantially, and there appears to be a second crack that has formed. Finally, Figure 76 shows the tensile plot and the DIC strain map taken just before failure at 263 MPa. In the DIC strain map one can clearly see that the two cracks that were visible at 240 MPa have gown and that there appear to be four distinct cracks that can be identified in the image. This is the last DIC image taken before the subelement failed.

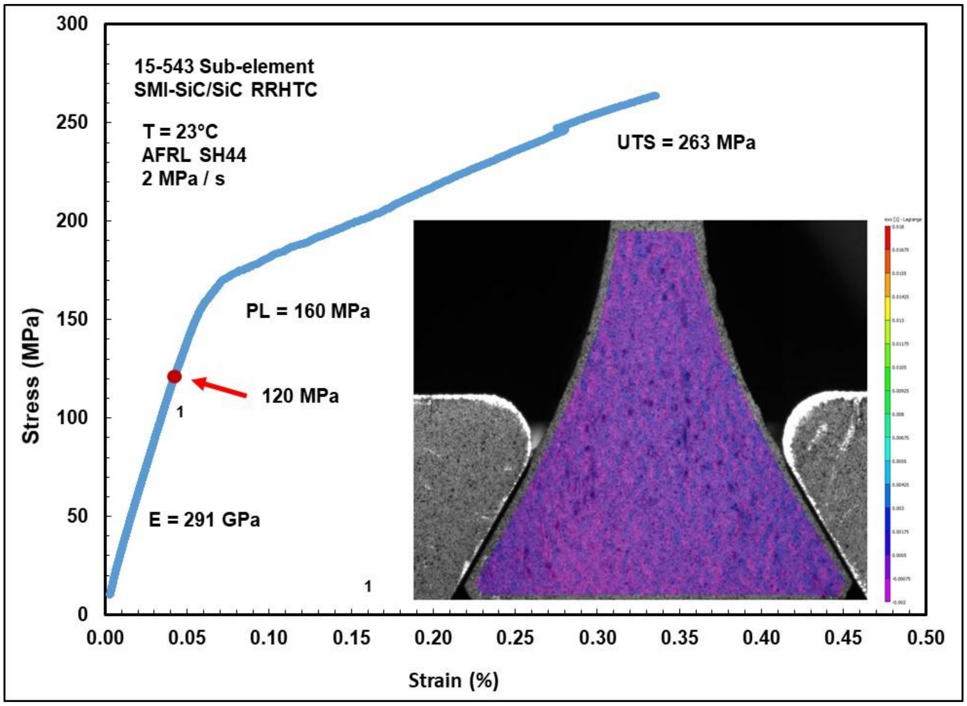

Figure 71. DIC Strain Map of Subelement Tensile Test Taken at 120 MPa

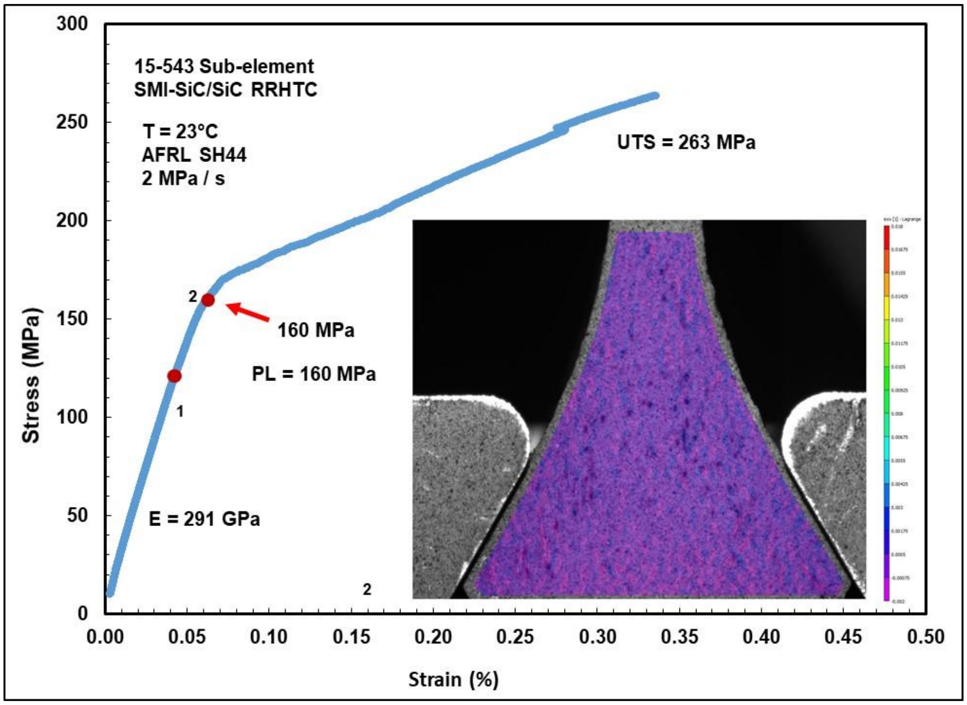

Figure 72. DIC Strain Map of Subelement Tensile Test Taken at 160 MPa

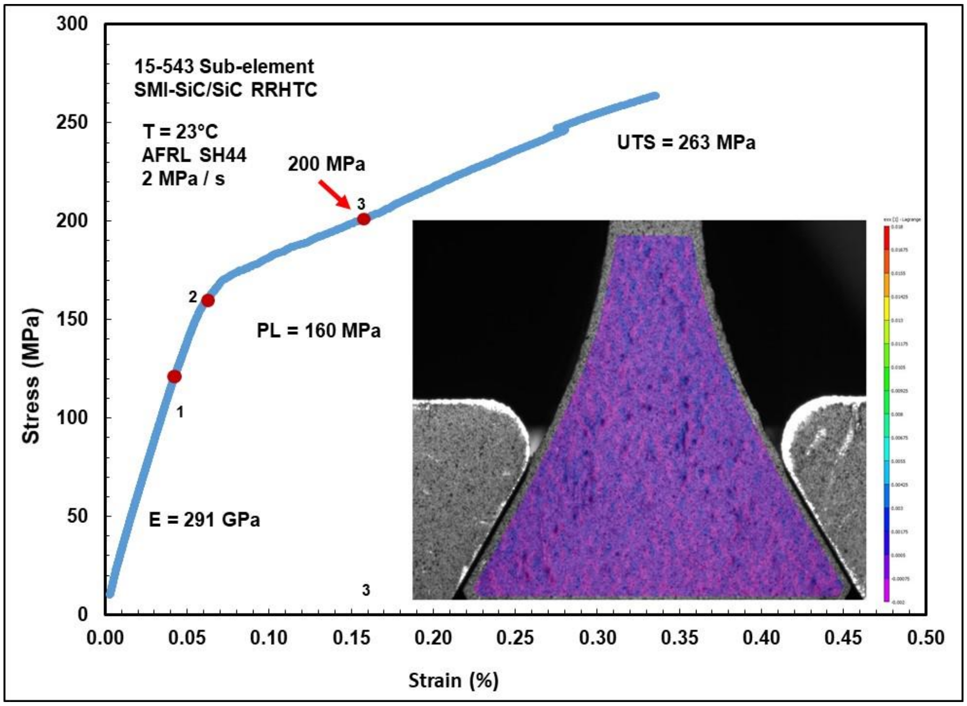

Figure 73. DIC Strain Map of Subelement Tensile Test Taken at 200 MPa

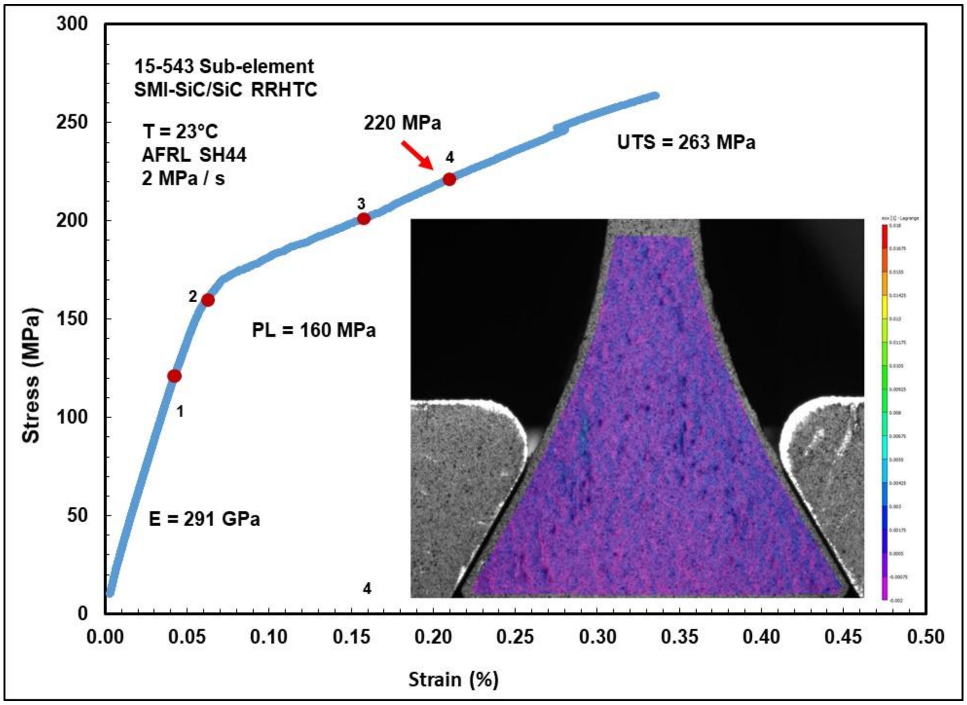

Figure 74. DIC Strain Map of Subelement Tensile Taken at 220 MPa

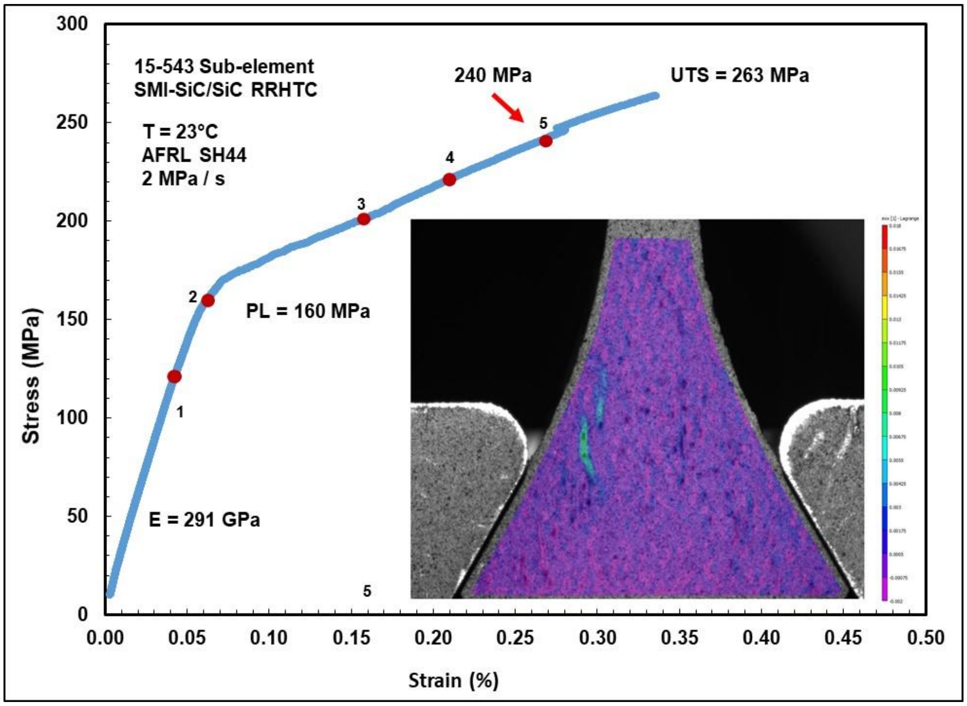

Figure 75. DIC Strain Map of Subelement Tensile Test Taken at 240 MPa

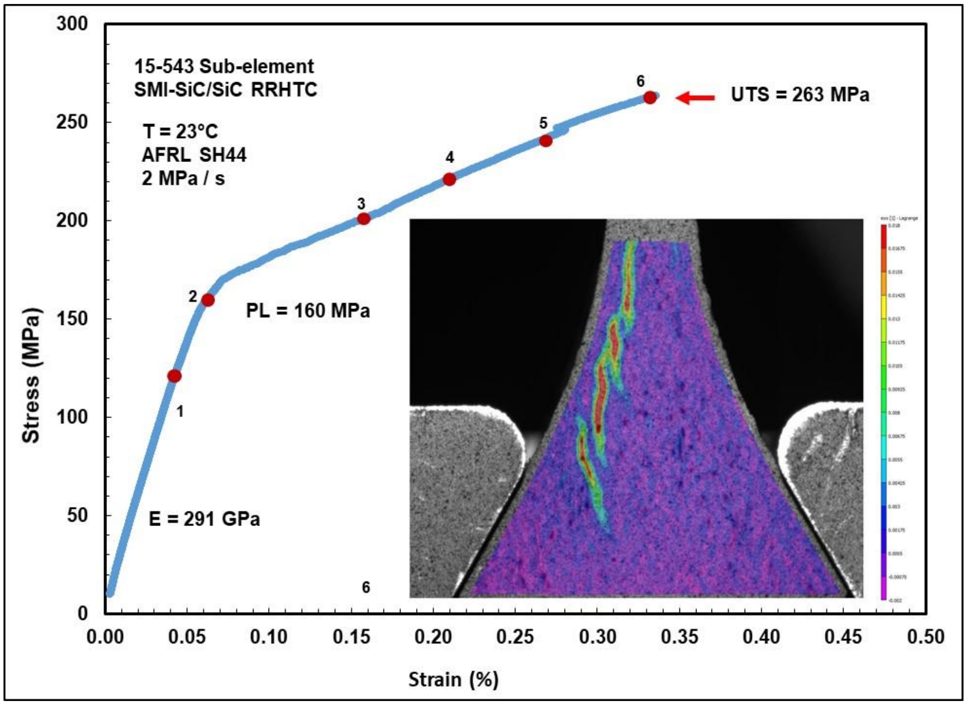

Figure 76. DIC Strain Map of Subelement Tensile Test Taken at 263 MPa

Damage growth was monitored using acoustic emission (AE), which captures acoustic waveforms that are generated when damaged occurs. AE data was measured by attaching three ultrasonic transducers at the locations shown in Figure 77a. A location density plot is shown in Figure 77b that highlights areas of high (red) crack growth as the subelement was loaded. Figure 77c shows the cumulative AE data that was used to estimate the onset stress. The AE onset stress is synonomous with the matrix cracking stress and is typically lower that the PL; indicating crack initiation occurs before the proportional limit is reached.

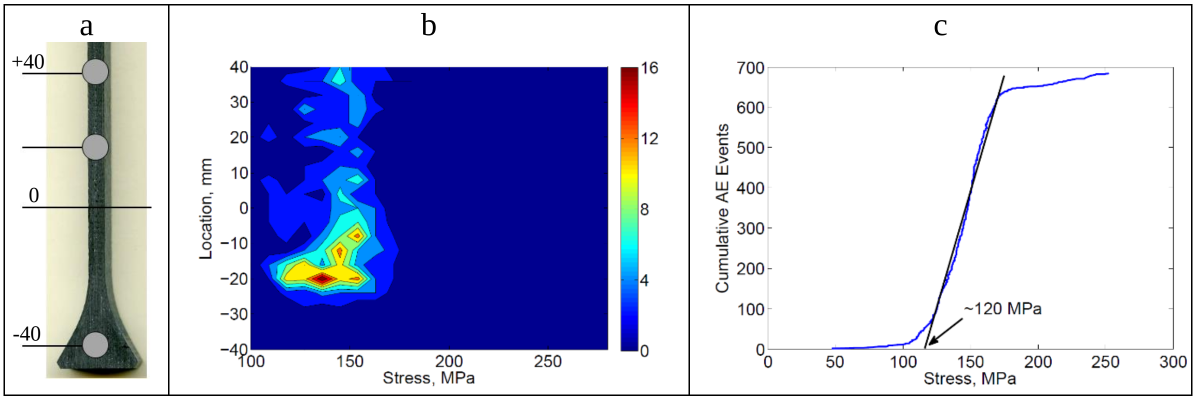

Figure 77. a) Instrumented Subelement With Three AE sensors b) Location Density Plot Highlighting Regions of Localized Crack Growth c) Cumulative AE Curve Used to Estimate the Matrix Cracking Stress

After the tension test was over, the fracture path and fracture behavior where documented using optical microscopy. The failed specimen is shown in Figure 78. It was noted that there was limited fiber pullout in the failed portion of the subelement stem. The fracture mechanism appears to be that the multiple ILT cracks in the dovetail coalesced and became one long ILT crack that formed between the 10 continuous plies and the wedge insert. This crack propagated both down and out to the surface, as well as up to the beginning of the radius and further, eventually penetrating the 10 outer plies and reaching the surface. Once the crack propagated to the radius between the dovetail and the stem, the cross-sectional area of the stem was greatly reduced and the specimen failed across the stem section of the subelement.

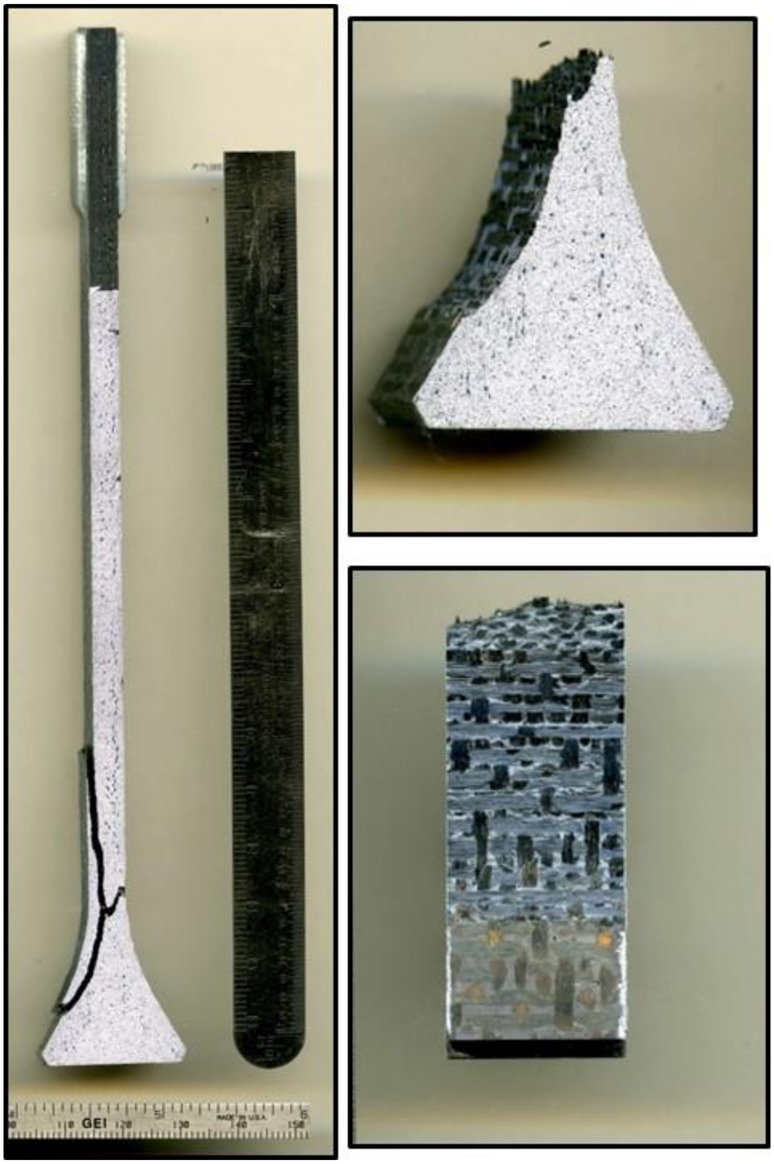

Figure 78. Photograph of Failed Subelement Tension Test Specimen (15-543)

The dovetail section was studied further using detailed microscopy. The dovetail was mounted and the DIC face polished using standard ceramography techniques. After polishing, very high resolution optical images were recorded. The images were then stitched together to create a montage of the entire polished cross section. By using high resolution images, it was possible to zoom in and identify matrix cracks. To highlight the cracks, they were traced over using bold red lines. The resulting image is also shown in Figure 79. Cracking in the stem is dominated by short delamination type cracks. In the transition region, cracks are concentrated at the sub-laminate/insert interface. These cracks appear to originate at the interface and propagate downward into the wedge insert. It is very important to highlight that the crack pattern closely matches what is observed from the DIC strain maps. The DIC maps indicated that all of the cracking was on one side of the dovetail, and the micrographs documented that there were indeed only crack on only one side of the subelement. There were not matrix cracks on the other side. This was a puzzling result and may suggest that once ILT cracks initiate, there is a shift in the stress state such that existing cracks grow, and no new cracks occur on the other side of the subelement. The low ILT values for cracking would have been expected to produce cracking on both sides of the dovetail, but this was not observed. During the testing, cracks developed on either one side of the dovetail or the other. Therefore, alignment issues are not thought to be the cause of cracking on only one side of the dovetail. Much more work would be required to understand this observed cracking behavior. .

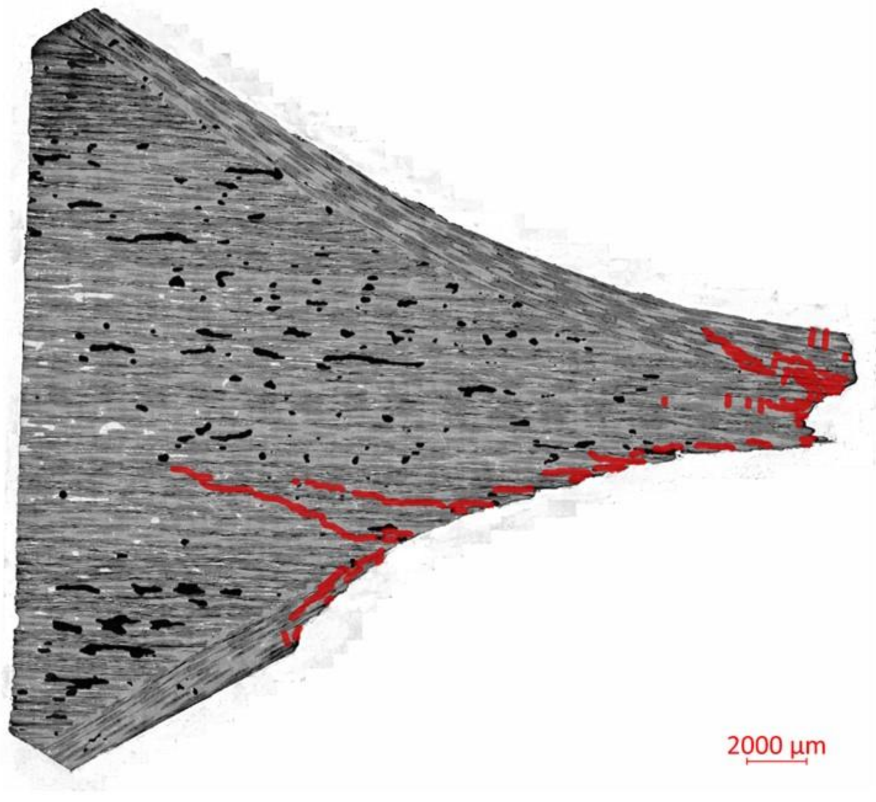

Figure 79. Micrograph of Polished Dovetail Edge of Subelement Tension Tested, With Cracks Highlighted In Red (15-543

5.2.2 Subelement Stepped Tension Test at 23°C (15-542)

The monotonic tensile test was followed by a stepped tension test at 23°C. The subelement was 15-542 and it was first characterized using optical microscopy and CT. An optical image of the edge of the subelement is shown in Figure 80. The specimen looks to be very good with only very minimal small round porosity observable in the image. There appear to be no abnormalities or large scale porosity. The CT image is presented in Figure 81 and shows a slice of the dovetail section of the subelement approximately at the center of the thickness. This image mirrors the optical photograph and documents that the interior of the dovetail section of the subelement was free of any significant amounts of porosity or delamination’s.

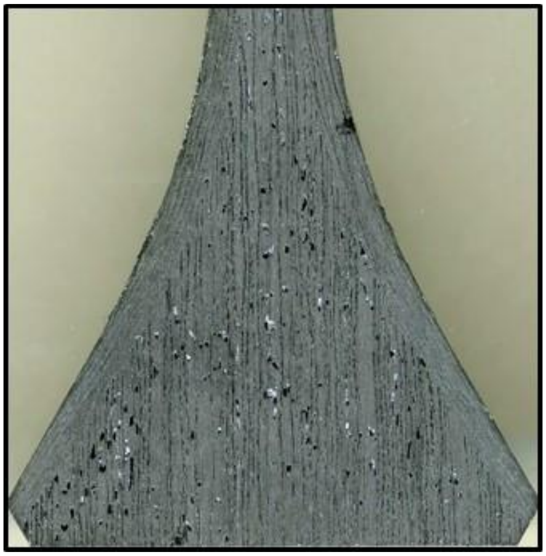

Figure 80. Optical Micrograph Of Dovetail Edge Of Stepped Tension Specimen 15-542

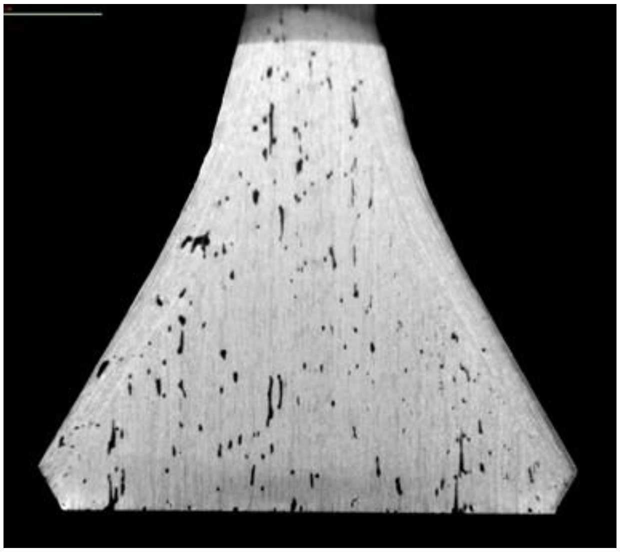

Figure 81. CT Scan of Dovetail Region OF Stepped Tension Specimen 15-542

The stepped tensile test was conducted to document the loading and unloading strain behavior as a function of applied load. This information is valuable to the modeling community, as any permanent strain measured is a good indication as to the amount of damage to stem section of the CMC. The test was run where the specimen was sequentially loaded and unloaded several times using increasing stress levels. The initial stress level was selected to be 50 MPa as this was substantially below the PL and would provide a nice baseline for the DIC strain map images. Stress levels were increased in 25 MPa increments, with the goal of reaching the monotonic tensile UTS of approximately 265 MPa.

A schematic of the loading sequence is presented in Figure 82 . Loading was slower than normal so that a sufficient number of DIC images could be recorded. Figure 83 shows the load and unload traces on a plot of stress versus strain for cycles 1, 2, 3, 4, 5, 6, 7, 9, and 10. The first five stepped tensile loading cycles increased the stress level from 50 MPa to 150 MPa. For each of these loading steps the stress versus strain behavior was completely linear. For the sixth loading step to 175 MPa the PL was exceeded and one can observe that there was nonlinear stress-strain behavior between 160 MPa and 175 MPa. However, during unloading the strain essentially went back to zero. During loading step 7, the stress was increased to 200 MPa and there was extensive nonlinear stress-strain exhibited, with strain reaching 0.16%. During unloading, one can observe that there was permanent strain of ~0.018% and indicates significant damage has been introduced into the stem section of the subelement. The ninth loading step went to 250 MPa and again the specimen exhibited substantial nonlinear strain accumulation during loading and approximately 0.045% permanent strain during unloading. The tenth loading step was to be to a maximum stress level of 275 MPa. However, the specimen failed during loading at 246 MPa and ~0.32% strain. It is important to note that each subsequent loading cycle about the PL exhibited essentially linear behavior up to the stress level of the previous loading cycle.

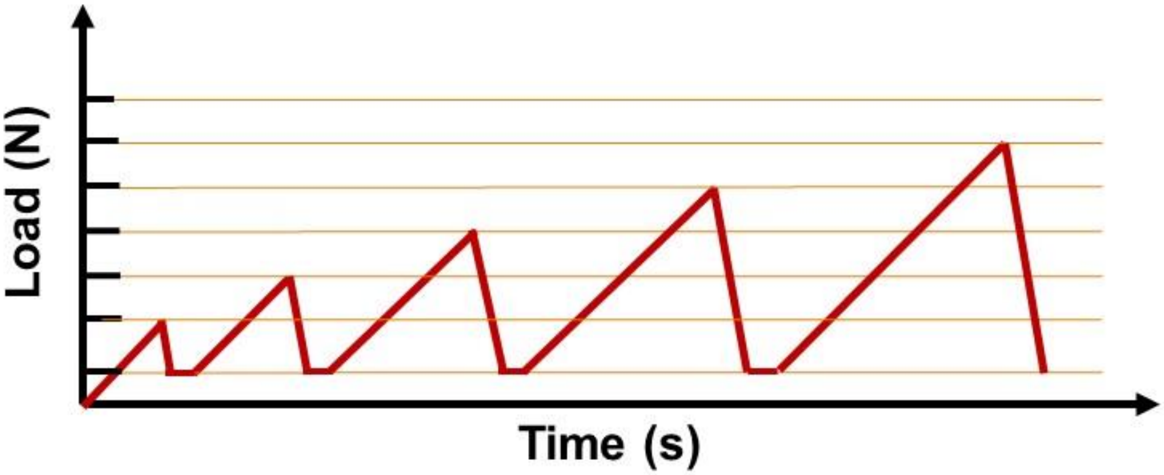

Figure 82. Schematic Of Loading Sequence Used For Stepped Tension Test Of Subelement

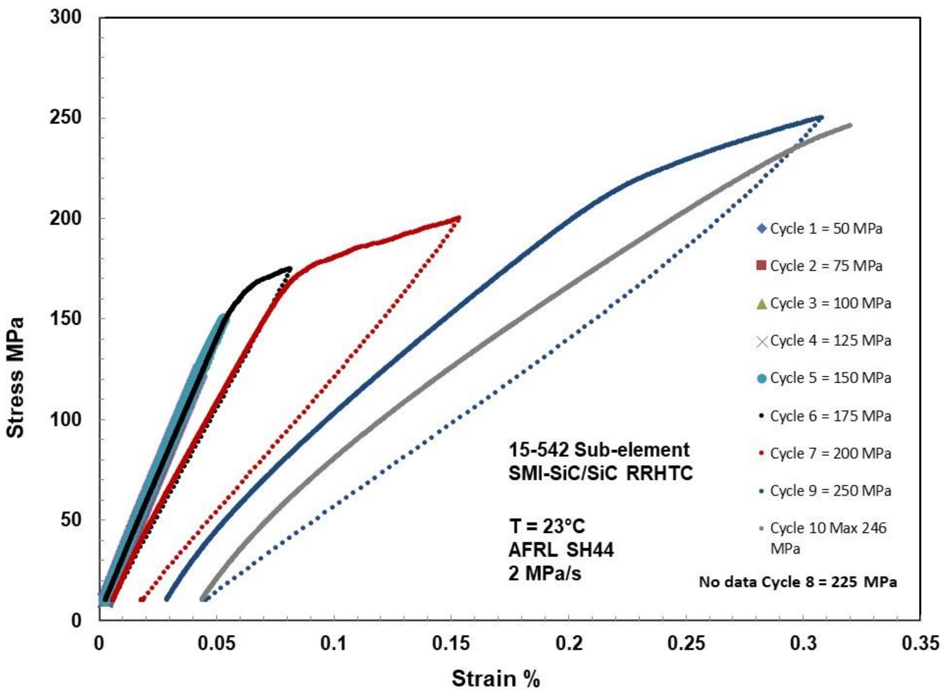

Figure 83. Stress-Strain Traces For Stepped Tensile Test Of Subelement (15-542)

The last two loading steps can be further investigated by studying the DIC strain maps at specific loads. Figure 84 shows the DIC strain map for step 9 and for a stress of 230 MPa. It is at this point that the first sign of ILT cracks could be determined from the DIC strain map images. Figure 85 shows the DIC image for loading step 9 and a stress level of 240 MPa. In this image there now appears to be two ILT formed cracks in the dovetail. Figure 86 shows the DIC strain map for loading step 9 and at maximum applied stress of 250 MPa. All of the existing cracks have exhibited crack extension, and there now appear to be four major ILT cracks.

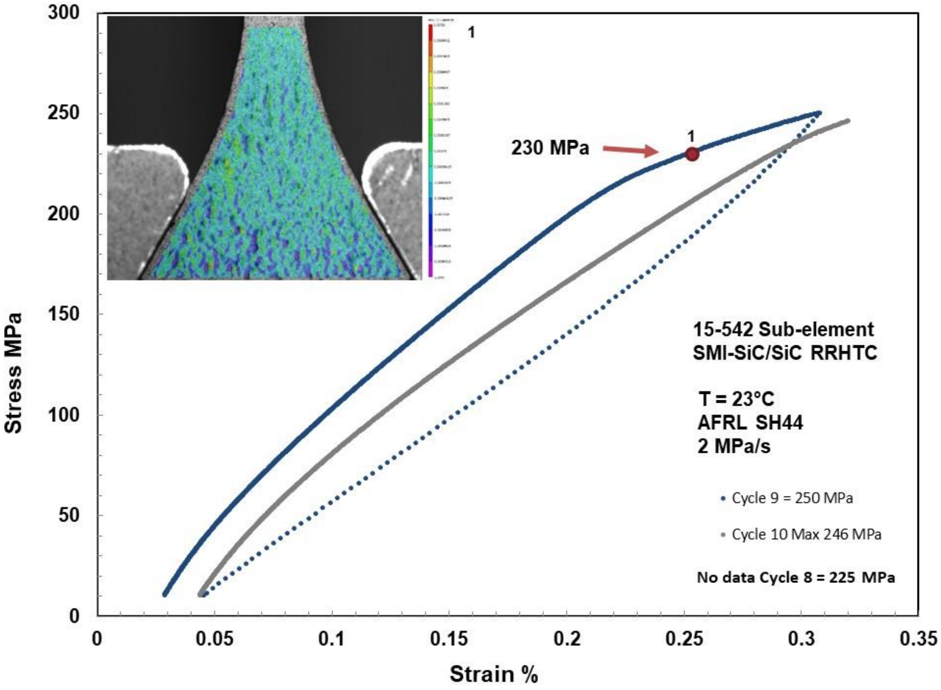

Figure 84. Stress-Strain Traces and DIC Strain For Stepped Tensile: Cycle 9 (230 MPa)

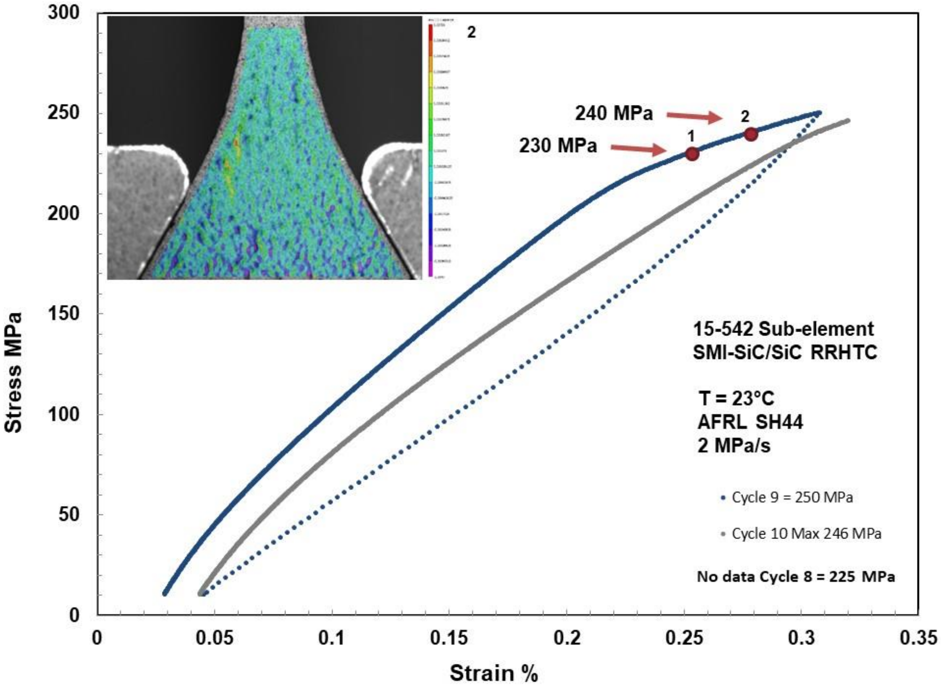

Figure 85. Stress-Strain Traces and DIC Strain For Stepped Tensile: Cycle 9 (240 MPa)

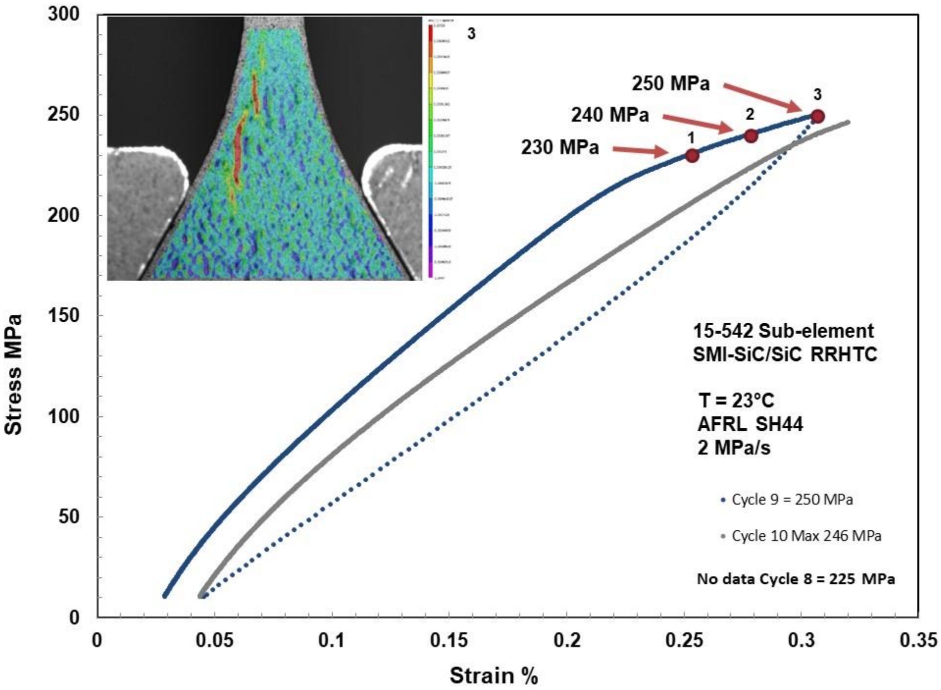

Figure 86. Stress-Strain Traces and DIC Strain For Stepped Tensile: Cycle 9 (250 MPa)

The subelement was then unloaded and reload for step 10 with the intent to reach 275 MPa, but the subelement failed at 246 MPa. Figure 87 shows the DIC strain map during loading when the stress level was 110 MPa. What is surprising is that there are no ILT cracks present in this image. We know they are there from the previous loading cycle, but they do not appear in the DIC strain map indicating that they have not started to open up. Figure 88 shows the DIC strain map for loading step 10 and a stress of 160 MPa. In the strain map one can see one small ILT crack. Figure 89 shows the DIC strain map for loading step 10 and a stress of 210 MPa. In the DIC strain map there are 2 cracks, and the first crack has grown considerably. Figure 90 presents the DIC strain map for loading step 10 and a stress level of ~266 MPa and was the last DIC image recorded before failure. This was just before failure. In the DIC strain map image one can observe 3 very large ILT cracks, and the two existing cracks from the previous DIC strain map at 210 MPa have grown significantly. Figure 91 shows an expanded view of the DIC strain map just before failure. In this expanded view one can observe that there are many cracks, and they are almost completely linked up. It was immediately after this image was taken that the subelement failed.

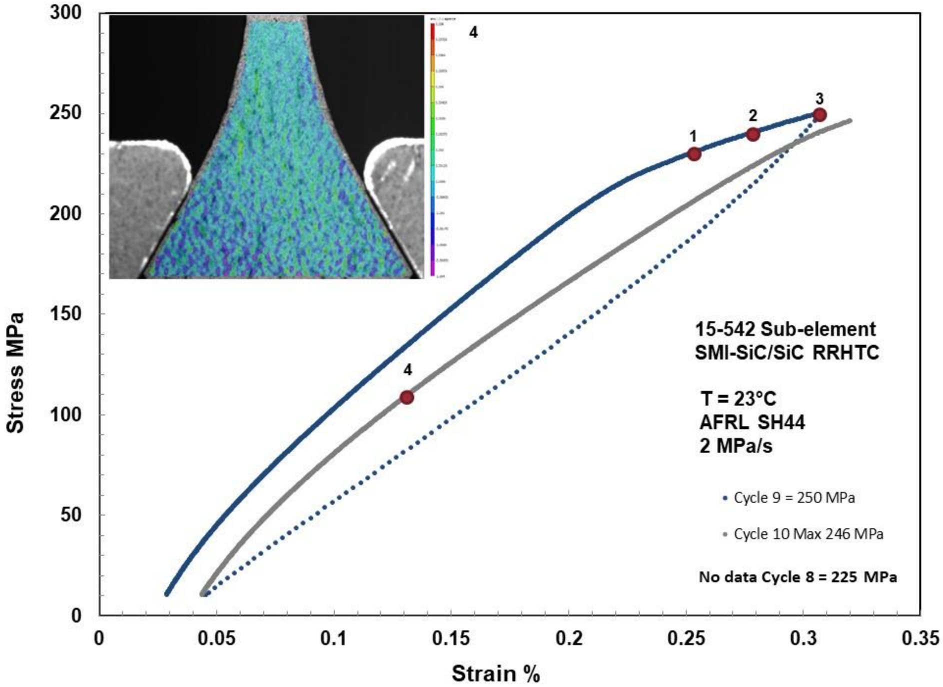

Figure 87. Stress-Strain Traces and DIC Strain For Stepped Tensile: Cycle 10 (110 MPa)

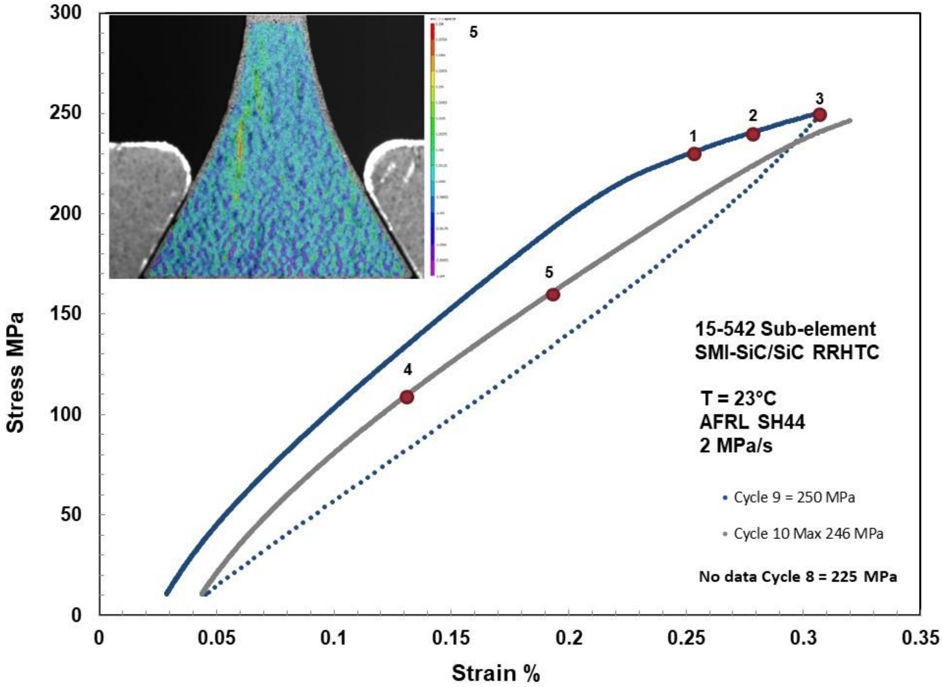

Figure 88. Stress-Strain Traces and DIC Strain For Stepped Tensile: Cycle 10 (160 MPa)

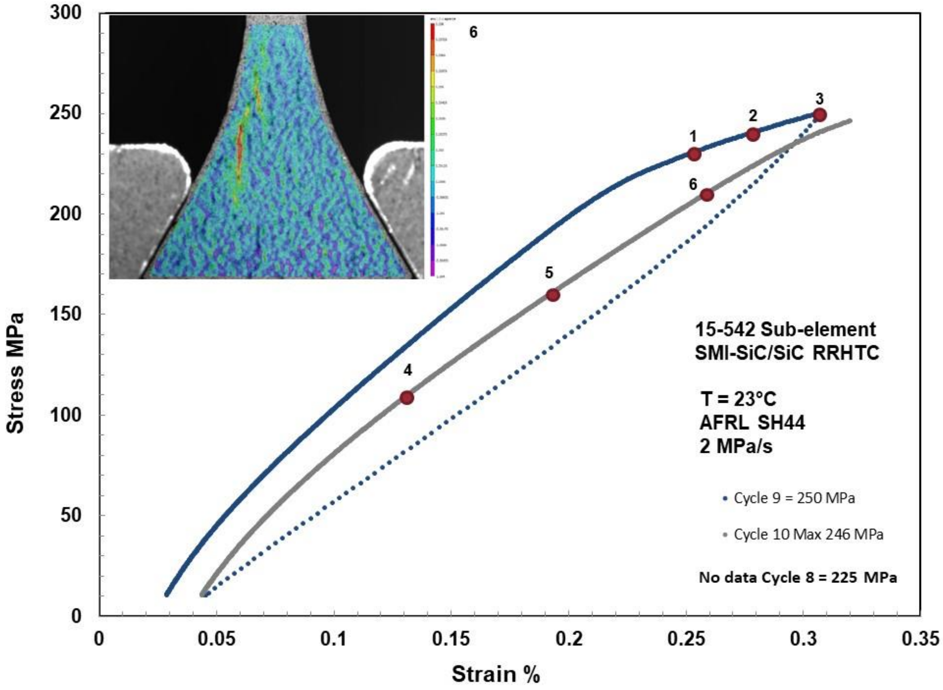

Figure 89. Stress-Strain Traces and DIC Strain For Stepped Tensile: Cycle 10 (210 MPa)

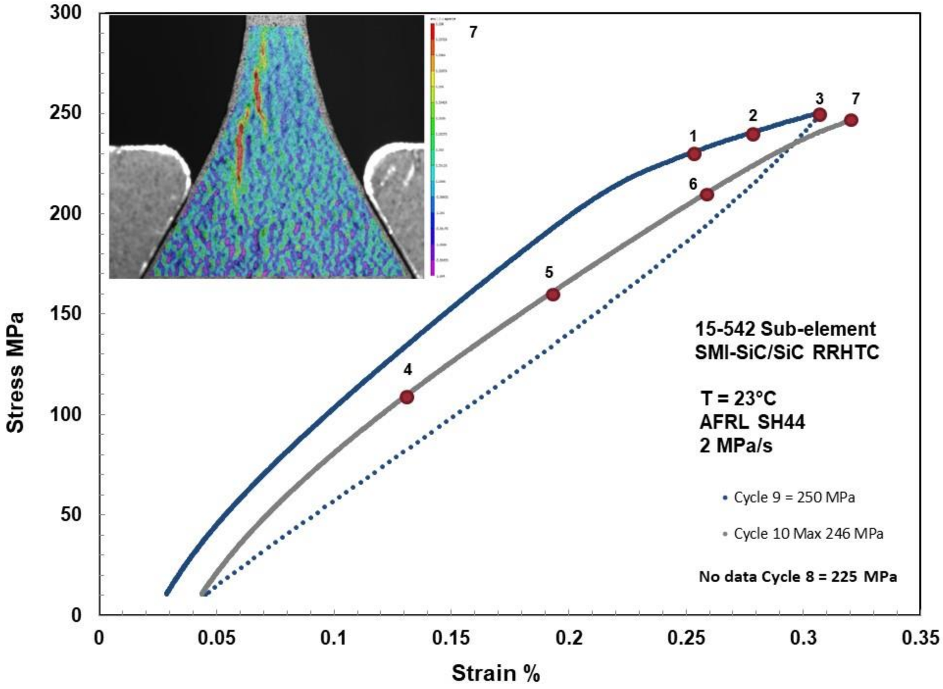

Figure 90. Stress-Strain Traces And DIC Strain For Stepped Tensile: Cycle 10 (246 MPa)

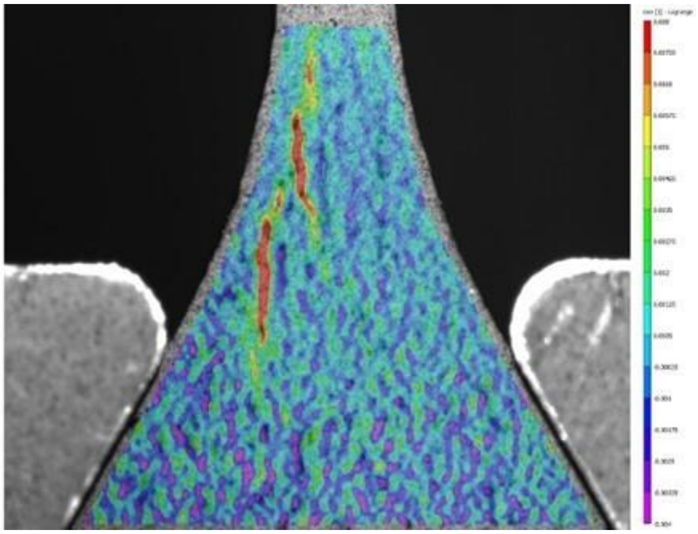

Figure 91. DIC Strain Map For Stepped Tension At 246 MPa (15-542)

The AE behavior of this specimen was thoroughly studied. The cumulative AE plot is shown below in Figure 92. In addition to being used to estimate the matrix cracking stress, the cumulative AE plot also highlights the relationship between increasing the applied stress and crack growth. During multiple loading cycles, there was minimal crack growth until the previous maximum stress is exceeded. For example, in Figure 92, the cumulative events for the 125 MPa cycle is shown in purple. The next cycle (150 MPa) shows cracks starting aroung 125 MPa and continuing up to 150 MPa. The result is the green curve appearing to be a continuation of the purple curve, which is expected during stable crack growth. However, as the stress continues to increase, the damage growth will eventually become unstable and cracks will occur before the previous stress is exceeded. The first indication of unstable crack growth can be observed during the 175 MPa cycle (cyan curve). Instead of being a continuation of the green curve, the cyan curve is shifted slightly left, indicating crack growth started before the previous maximum stress was exceeded. This effect is exagerated in the subsequent cycles.

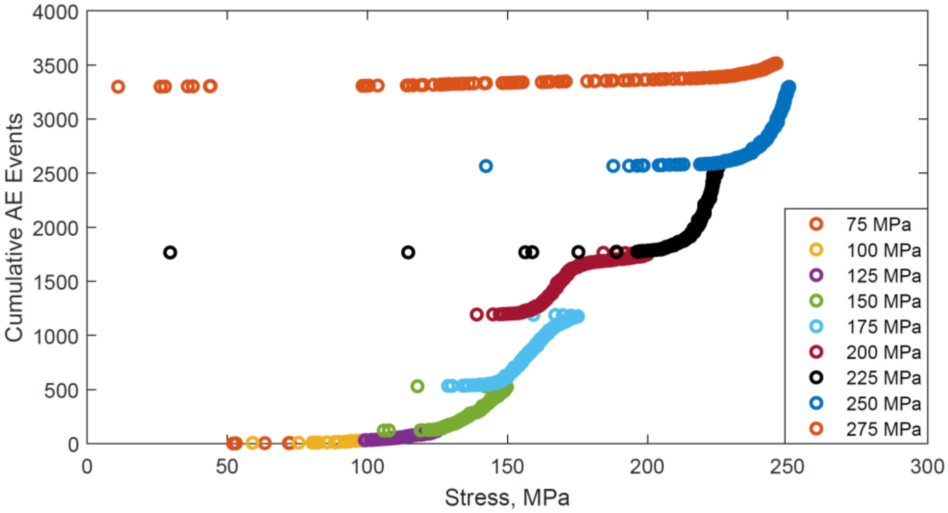

Figure 92. Cumulative AE Energy Plot for Stepped Tensile Cycles 2-10

The fracture features were characterize using optical microscopy. The failed subelement is shown in Figure 93. One can see that the crack path perfectly matches the cracks observed in the DIC strain maps. The dovetail section of the failed subelement was mounted and polished in order to study and identify matrix cracks. For this failed subelement the DIC edge was mounted and polished, and is presented as Figure 94. The visible matrix cracks are shown as heavy white lines. The one large crack penetrating deep into the dovetail closely matches the crack observed in the DIC strain map taken at 246 MPa just before failure.

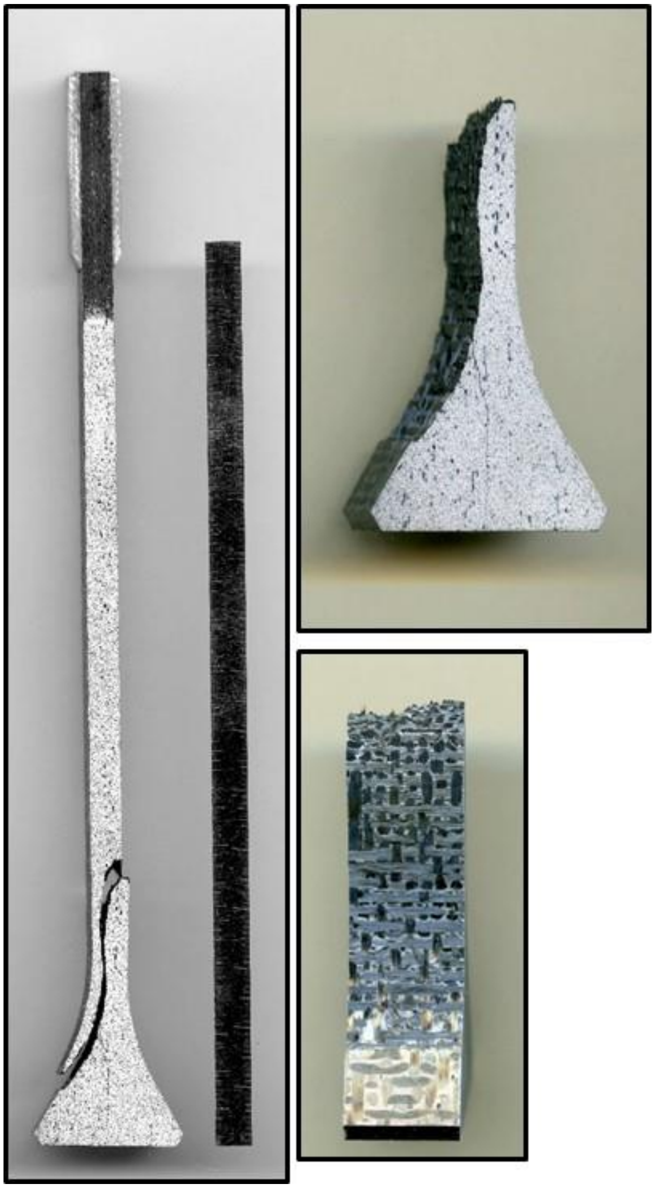

Figure 93. Optical Photographs Of Failed Stepped Tension Specimen (15-542)

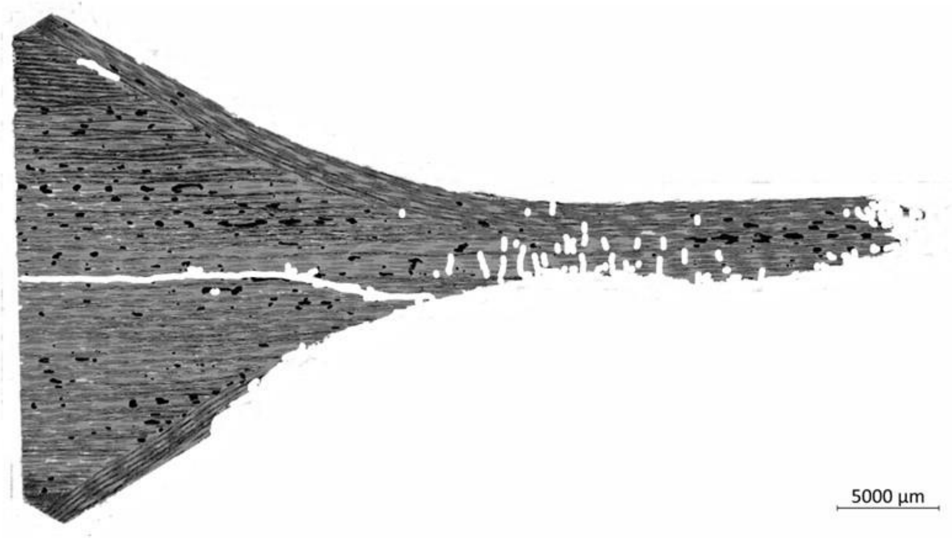

Figure 94. Micrograph Of Failed Stepped Subelement Tension Test (15-542)

5.2.3 **Subelement Stepped Fatigue at 23°C (15-544)**

Tension testing was followed by fatigue testing, as airfoils experience significant fatigue loading conditions during operation. To efficiently study fatigue behavior, it was decided that the first fatigue test would involve running a set number of fatigue cycles, then increasing the stress and running another set of cycles, until the specimen fails. This type of loading is referred to as a stepped fatigue test. Figure 95 provides a schematic that the details the loading process. The testing at each stress level was conducted in three phases: 1) the subelement was loaded to the target stress, 2) the subelement was fatigue loaded for 1,000 cycles at R=0. 1 and then unloaded, followed by a slow ramp up to the applied stress value to allow DIC images to be taken (this sub-cycling was done ten times within each block), 3) and the subelement was unloaded. This sequence was repeated 10 times to produce 10,000 cycles at each stress level. Once the block of 10,000 cycles was complete, the stress level was increased by 25 MPa and the ten sub-cycles repeated. The block of cycles and corresponding stress levels used for this stepped fatigue testing were as follows: block 1 = 125 MPa, block 2 = 150 MPa, block 3 = 175 MPa, block 4 = 200 MPa, and block 5 = 225 MPa. The specimen failoed during block 5 at 225 MPa after experiencing 3151 fatigue cycles at 225 MPa.

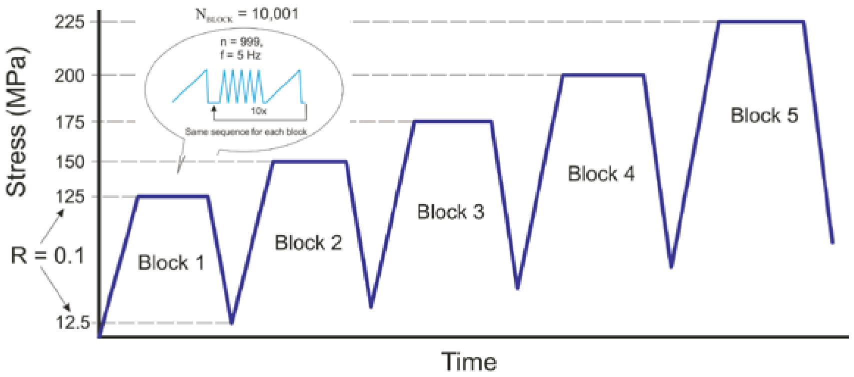

Figure 95. Schematic Showing Sequential Loading Blocks For Stepped Fatigue

As mentioned above, each sub-block allowed multiple extensometer and DIC images to be captured within each block. This provided multiple data points to monitor how the modulus, strain, and damage evolved as a function of the number of cycles. DIC images were acquired during the ramp up portion of each block and sub-block. No cracks were observed through block 3, which was at a maximum stress of 175 MPa. DIC strain maps were only able to first identify an observable crack during the middle of Block 4 (200 MPa) at cycle 36,003. DIC strain maps from block 4 are presented in Figure 96 and show the strain maps captured at cycles 36,003, 37,003, and 38,003. From these three DIC strain maps one can observe that an ILT crack has formed. After appearing, the crack essentially stabilized, and did not grow between 36,003 cycles and 39,999 cycles. It is important to note that the crack morphology is almost identical to that of the fast fracture test, signifying that the same damage mechanism had occurred.

Block 5 was conducted at 225 MPa, and the subelement failed at 4151 cycles at this stress level (44,151 total cycles). DIC strain maps for cycles 40,004, 41004, and 44,004 are presented in Figure 97. In these images it is clear that the initial ILT crack grows and that multiple ILT cracks from and appear to link up. It is this formation and linking up of multiple ILT cracks that leads to failure.

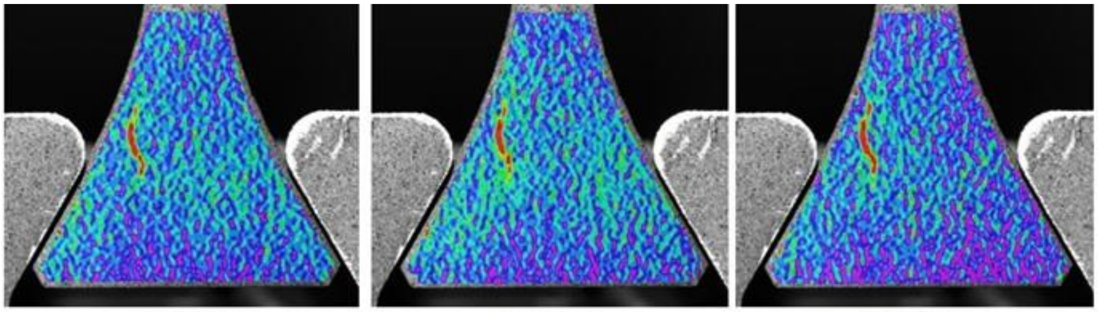

N = 36,003
Max Stress = 200 MPa

N = 37,003
Max Stress = 200 MPa

N = 38,003
Max Stress = 200 MPa

Figure 96. DIC Images For Stepped Fatigue at 200 MPa 15-544))

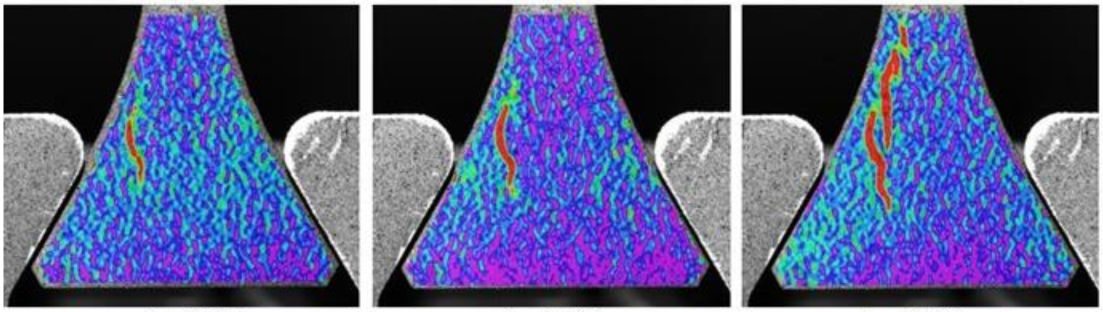

N = 40,004
Max Stress = 200 MPa

N = 41,004
Max Stress = 225 MPa

N = 44,004
Max Stress = 225 MPa

Figure 97. DIC Images For Stepped Fatigue at 225 MPa (15-544)

The acoustic emission data for the first sub-blocks of Blocks 1, 3, 4, and 5 are shown below in Figure 98. Since each sub-block began with a ramp up before cycling, the AE onset stress (i.e. “matrix cracking stress”) can be captured by extrapolating the linear portion of the ramp up curve through the x-axis. The onset stresses for Blocks 1, 3, 4, and 5 are 100, 150, 190, and 205 MPa, respectively. The y-axis is the number of cumulative events and with each block exhibiting different cracking rates, the total number of measured events varies. Using the cumulative curves below, it appears that there was more crack growth during Blocks 1 and 5 during “ramp up” than there was for Block 4. Figure 99 shows a cumulative AE energy curve for all five blocks. Within Block 1, a high rate of events was seen during the ramp up and lower rate during the rest of the block. Minimal events were captured during Blocks 2 and 3, which lead to a plateau in the curve. Sudden increases in the energy curve are seen in the beginning of Blocks 4 and 5, which signifies damage growth. The plateau at the end of Block 4 signifies a stable damage region. However, the damage region becomes unstable during Block 5 and the subelement failed during cyclic loading at this stress level.

Using the DIC strain map images, one can approximate the length of the multiple ILT cracks. Figure 100 presents the total observed length of the ILT crack as a function of cycles. At 200 MPa the length of the damage zone grows but then appears to stabilize. However, once the stress level is increased to 225 MPa the damage zone continues to increase in length with continued cycling.

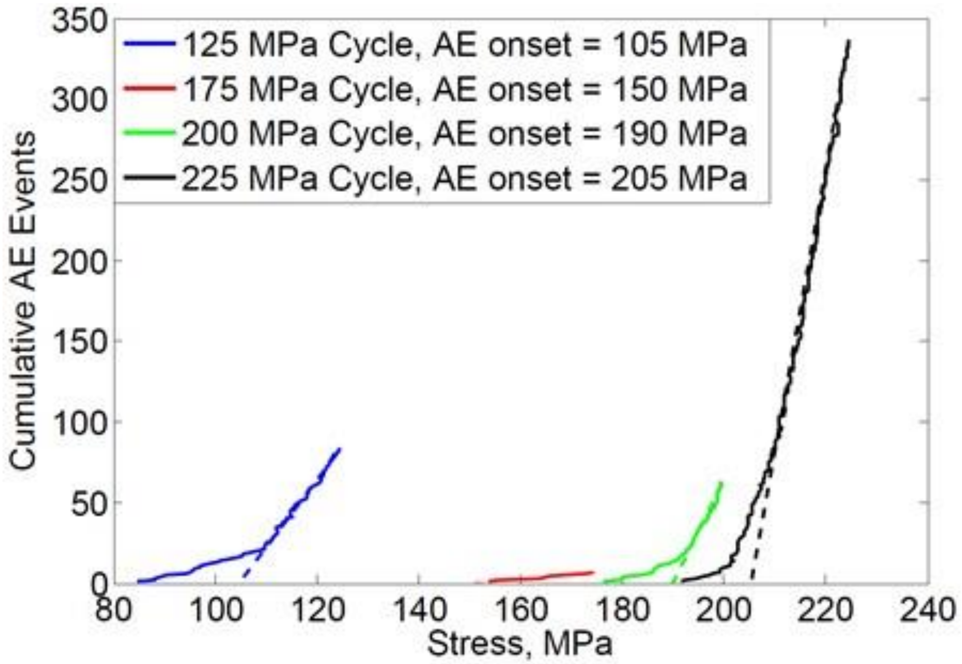

Figure 98. AE Events For The Stepped Fatigue Test

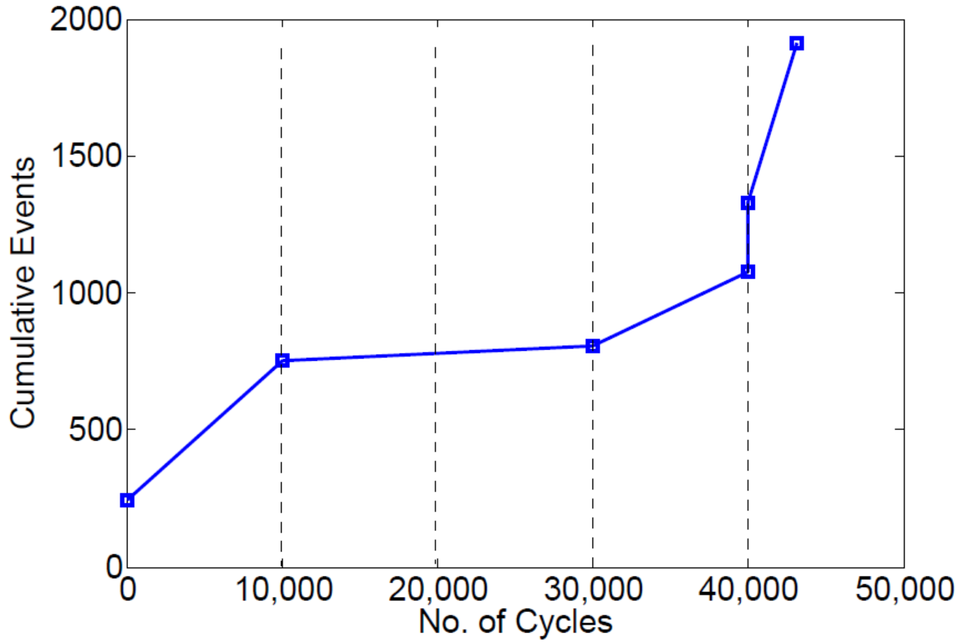

Figure 99. Cumulative AE Events Versus Number of Total Fatigue Cycles

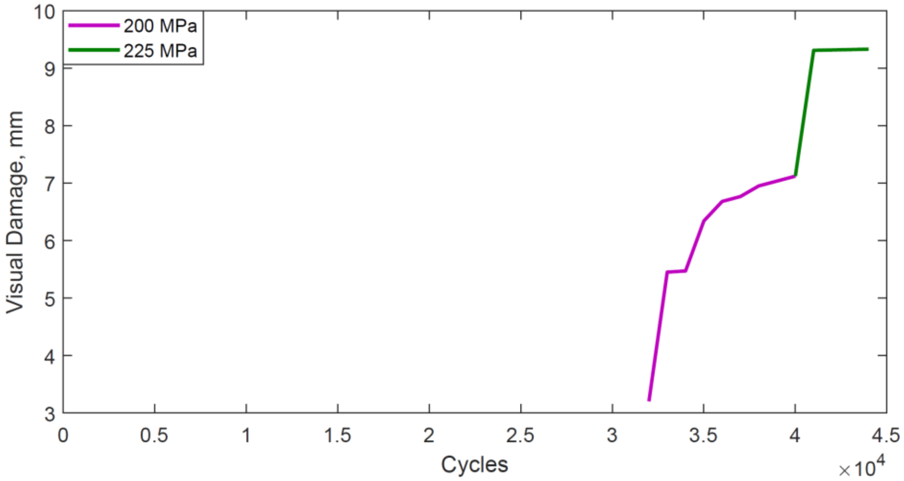

Figure 100. Length of Visual Cracks (From DIC) Versus Number Of Fatigue Cycles

The dovetail section of the failed subelement was studied using CT. Figure 101 is a 3-dimensional CT reconstruction of the failed dovetail section. Careful study of these reconstructions documented that there was no concentration of porosity along the fracture path. The observed ILT cracks formed because of the stress state and unique plie geometry and not because of porosity.

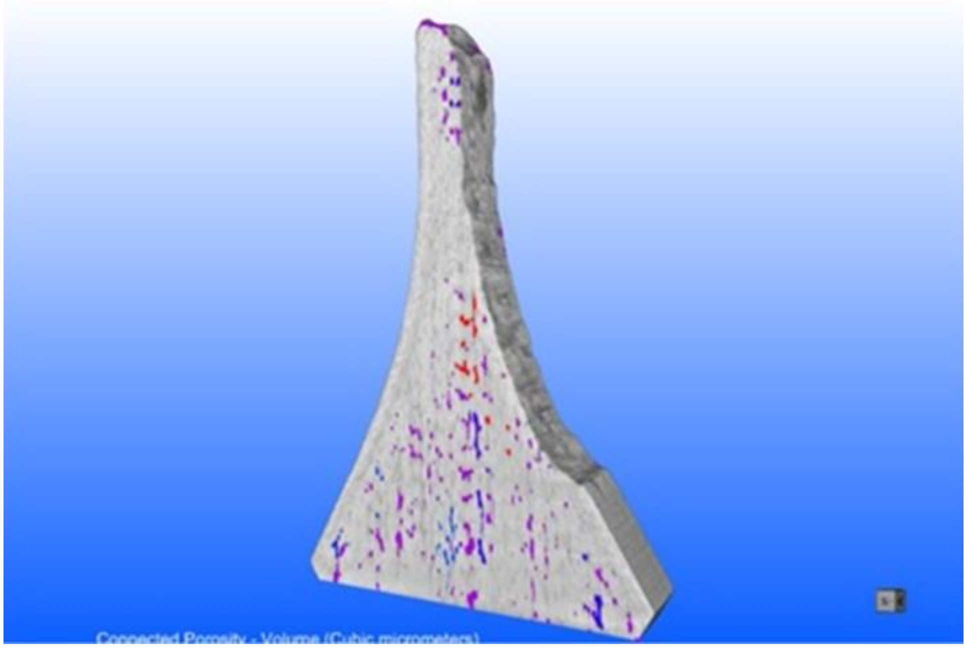

Figure 101. CT Image of Failed Stepped Fatigue Subelement (15-544)

The fracture surfaces of the failed specimen were documented using optical microscopy. Figure 102 presents three images of the failed subelement, and images of the failed dovetail region are shown in Figure 103. It is clear from these images that the cracks observed in the DIC image linked up and failed the specimen. These cracks traveled along the interface between the ten outer continuous plies and the wedge inserts. Once the expanding crack reached the straight sided stem section of the subelement the test specimen failed across the remaining portion of the shank. The bottom end of the crack penetrated through the 10 outer plies well before reaching the end of the specimen

Detailed microscopy was performed on the failed stepped fatigue subelement to document actual matrix cracks on the edge of the specimen as well as in the center of the specimen. In order to do this characterization the dovetail section of the subelement was first sectioned into two pieces as shown in Figure 104. The sectioning cut was down the centerline of the test specimen. For one half, the centerline face was polished, while for the second half the edge face that had the DIC speckle pattern on it was polished. The two halves were mounted and polished using standard ceramography techniques. The resulting image for each half is shown in Figure 104. Cracking in the stem is dominated by transverse matrix cracks, similar to what was observed in the flat dogbone test specimens. In the transition region, cracks are concentrated at the interface between the continuous plies and wedge insert. Cracks appear to originate at the interface and propagate downward into the wedge insert of dovetail section and follow the interfaces between the plies that make up the wedge insert. It is very important to point out that the crack pattern at the centerline of the subelement is almost an exact match to the cracks observed on the surface, and that these cracks closely match what is observed from the strain map data from DIC. It is also important to note that detailed microscopy revealed that essentially all observable cracks are on one side of the specimen, and there were not matrix cracks on the other side. This may indicate that once the ILT cracks initiate, there is a shift in the stress state. Much more work would be required to understand this observed cracking.

Figure 102. Photographs of Failed Subelement From Stepped Fatigue (15-544)

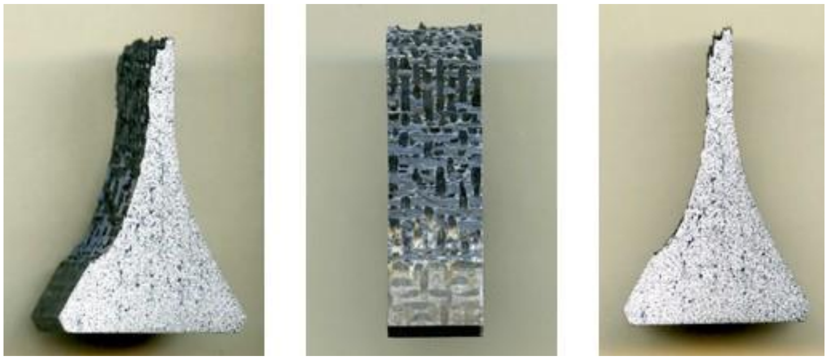

Figure 103. Photographs of Failed Subelement Dovetail Section For Stepped Fatigue (15-544)

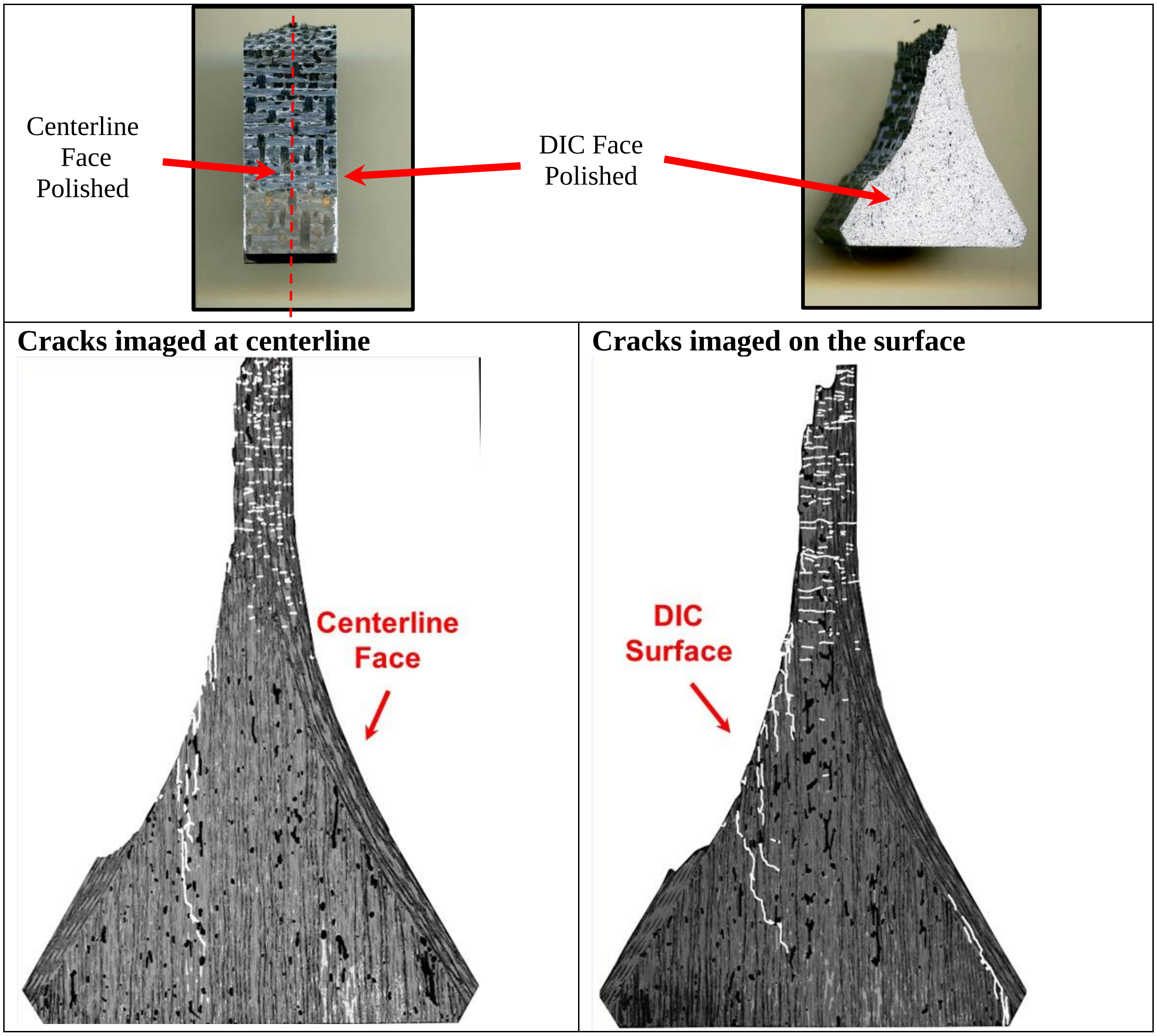

Figure 104. Microscopy of Failed Subelement Stepped Fatigue Test At Surface And Center Of Dovetail (15-544)

The stepped fatigue test provided very important information about the development of damage and damage propagation during fatigue loading of the subelement test specimen. ILT cracks were not observed until the fatigue stress level was increased to 200 MPa. However, this initial damage appeared to stabilize with continued cycling at 200 MPa. It was only at an applied stress level of 225 MPa that the ILT cracks extended, and multiple ILT cracks formed. The identification of the ILT cracks using DIC was backed up using detailed high resolution microscopy. Figure 105 is a diagram showing the excellent link between FEA and DIC and microscopy. FEA predicted that ILT cracks would form in the dovetail and that these cracks would form between the 10 continuous plies and the wedge inserts. FEA analysis indicated that ILT cracks would be the predominant damage mechanism. However, there is still much work to be done to relate FEA to damage. The main issue is that the FEA predicted ILT cracks to occur at approximately 90 MPa, but they were not observed until 200 MPa.

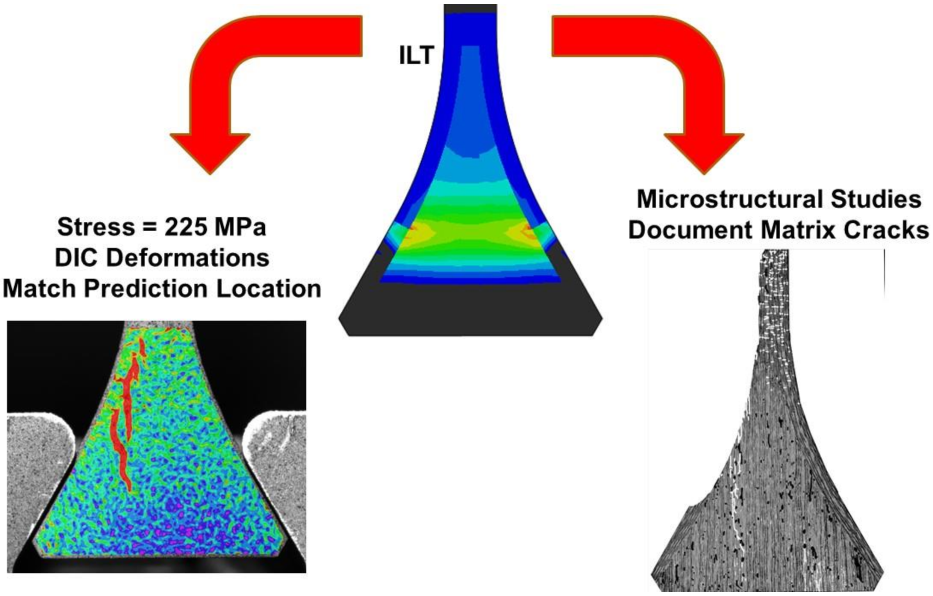

Figure 105. Diagram Demonstrating That ILT Predictions Match Location of ILT Induced Cracks Identified by DIC and Microscopy

5.2.4 **Subelement Fatigue at 23°C & 200 MPa (15-545)**

A tension-tension fatigue test was run at 200 MPa (R=0.1) using specimen 15-545. This stress level was selected as the previous stepped fatigue test identified that damage formed and stabilized at approximately 200 MPa. The subelement was fatigue tested at 200 MPa for 302,005 cycles without failure. The test was then halted.

Strain data was recorded on the stem of subelement by a clip-on extensometer. Percent strain versus cycles as well as modulus versus cycles is shown in Figure 106. The modulus was initially measured to be around 240 MPa but after only a few cycles, it dropped to 145 MPa. After 10,000 cycles it decreased to approximately 120 MPa and from there it stabilized. Strain accumulation increases up to approximately 50,000 cycles and then only increases 0.02% out to 302,005 cycles. A strain value of 0.8% was measured after 10,000 cycles. The strain starts to level off at 0.12% after 50,000 cycles and only slightly increased up until the test was stopped at 302,005 cycles. In both cases, damage occurs very quickly and then appears to stabilize after approximately 10,000 cycles.

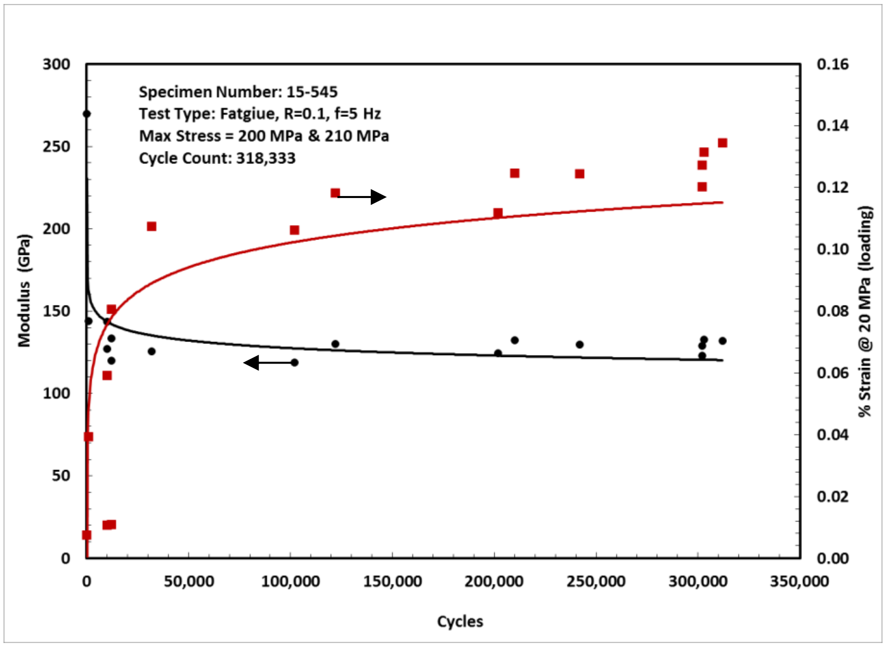

Figure 106. Modulus and % Strain Versus Cycles For A Fatigue Test of Subelement Tested at 200 MPa (15-545)

With the specimen being loaded above the proportional limit of 120 MPa, damage occurred within the first 1000 cycles and essentially stabilized after only approximately 10,000 cycles. After stabilization, no appreciable crack growth was detected and the damage length vs cycles curve reached a plateau. DIC strain maps taken at 200 MPa are shown in Figure 107 for cycles 1, 1001, and 5000 cycles, Figure 108 for cycles 62,003, 92,003, and 122,004, and Figure 109 for cycles 10,000, 152,000, and 302,005. At cycle 1 there is no sign of any cracks. However, by cycle 1,001 there is a significant ILT crack present, and this crack remains stable up to 60,003 cycles. By cycle 92,003 the damage zone appears to have slightly increased. However, from 92,003 cycles out to 302,005 cycles the damage appears to remain constant and does not increase with increasing cycle count..

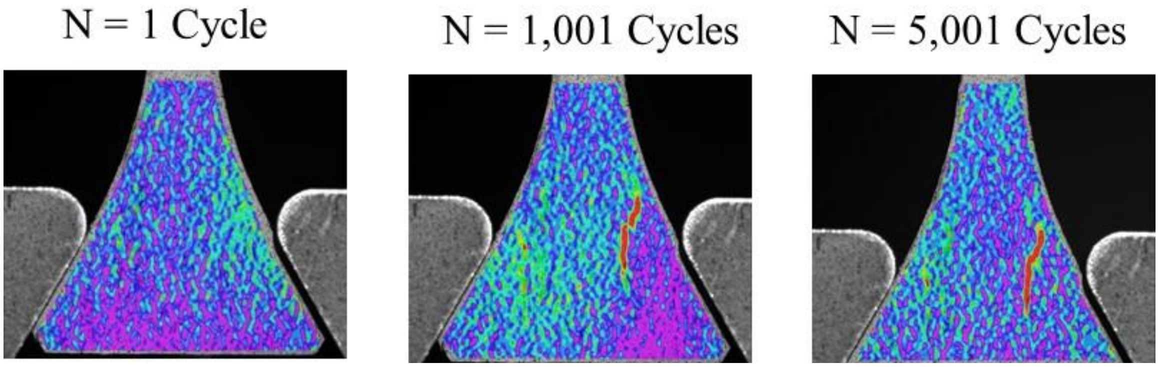

Figure 107. DIC Strain Maps At 200 MPa and 1, 1001, and 5001 Cycles (15-545)

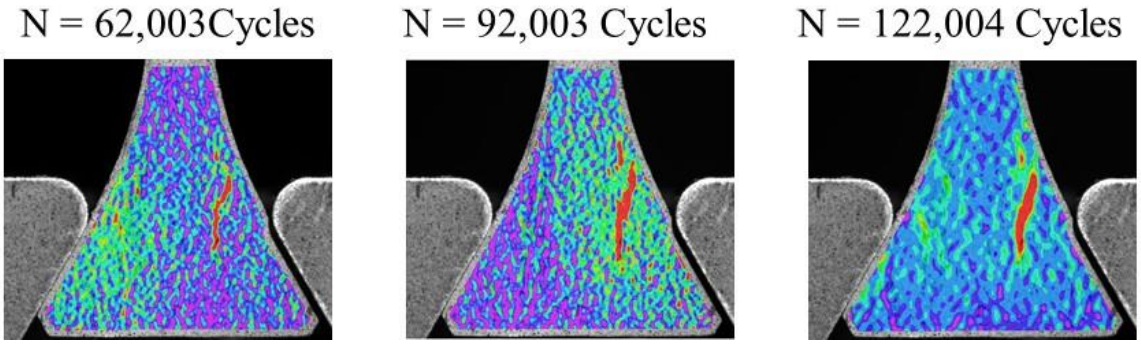

Figure 108. DIC Strain Maps At 200 MPa and 1, 1001, and 5001 Cycles (15-545)

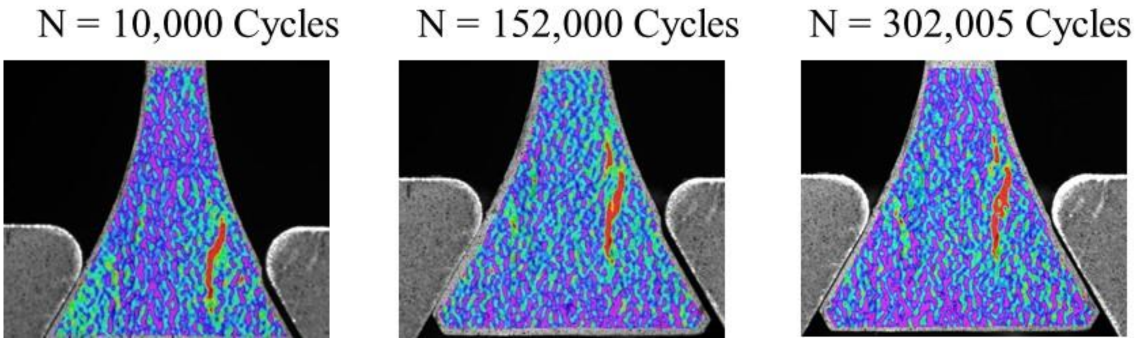

Figure 109. DIC Strain Maps At 200 MPa and 10,000, 152,000, and 302,005 Cycles (15-545)

5.2.5 **Subelement Fatigue at 23°C and 210 MPa (15-545a)**

It was decided to continue testing subelement 15-545 at a higher stress level. The initial test at 200 MPa was stopped, and the stress level was increased from 200 MPa to 210 MPa. The specimen then ran 16,325 cycles before failing, and unfortunately failure occurred in the straight sided stem 122 mm down from the top of the specimen. This demonstrates how finely balanced the design of the subelement was. The goal was to develop high ILT stress levels in the dovetail and then have the subelement fail in the dovetail region. The test team did not want the subelement to fail in the straight sided stem region. It appears that the room temperature fatigue limit for the stem region of the subelement is approximately 210 MPa to 225 MPa.

A DIC strain map taken at 9,995 cycles at 210 MPa (312,000 total cycles) is shown in Figure 110. In the image the crack length appears to be very similar to the strain map shown for cycle 302,005 indicating at this cycle count the ILT cracks had not grown and had remained relatively stable. Only at near the very end of the test did the crack damage zone begin to grow.

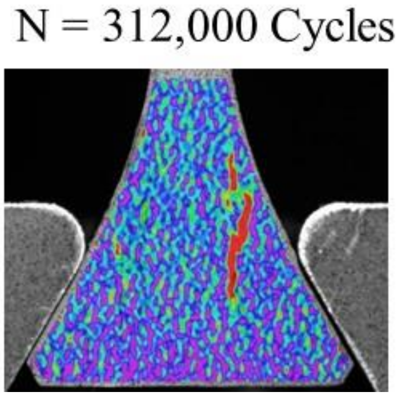

Figure 110. DIC Strain Maps At 210 MPa and Total Cycle Count Of 312,000 Cycles (15-545a)

The cumulative AE energy curve is presented in Figure 111 and shows the AE events quickly stabilized and remained constant for the remainder of the fatigue test at 200 MPa out to 302,005 cycles. Then when the stress was raise to 210 MPa the AE event first leveled off but then near the very end of the test the number of AE events accelerated. A damage zone length could be calculated from the DIC strain map images. Figure 112 presents damage zone length versus cycles. This plot mirrors the cumulative AE event plot.

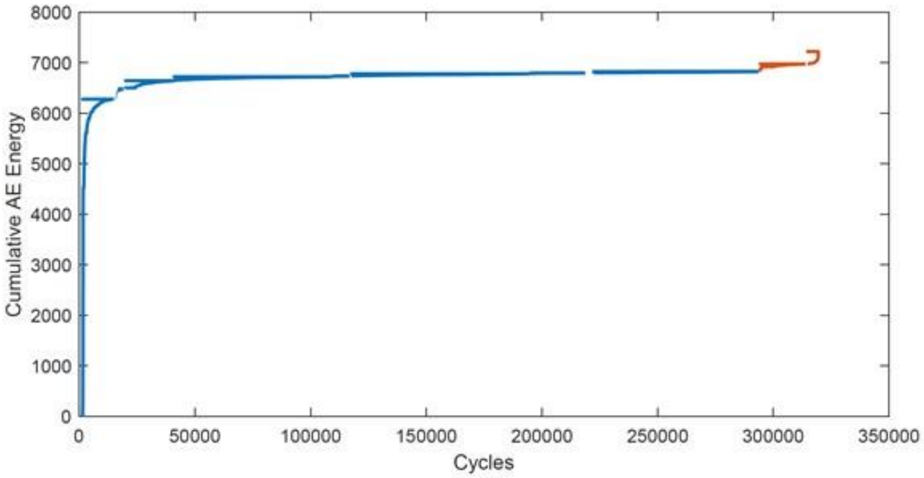

Figure 111. Cumulative AE Events For Fatigue Test of Subelement (15-545a)

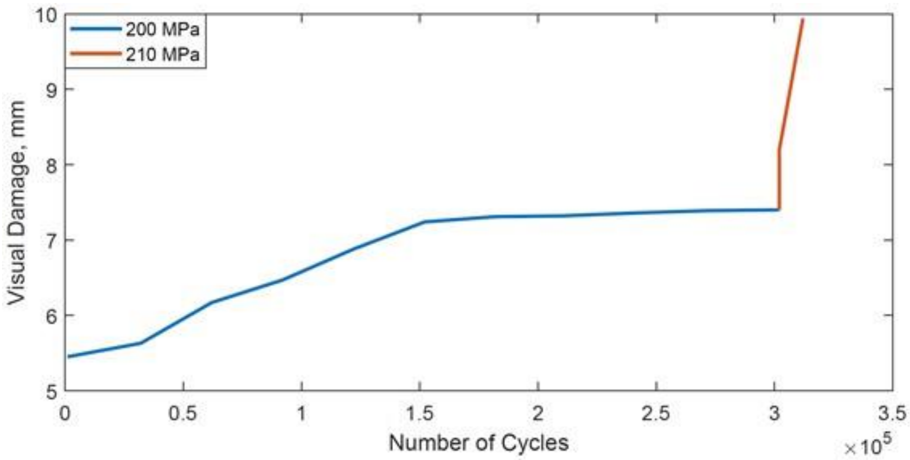

Figure 112. Damage Length vs Cycles For Subelement Fatigue Test (15-545a)

Failure of the subelement in the stem section and not the dovetail was frustrating because the stepped fatigue test did fail in the dovetail. However, the specimen was still very useful. The bottom portion of the failed specimen, which included the dovetail, was mounted and polished to identify matrix cracks. All observable cracks were highlighted using a solid white line. The polished image with the highlighted cracks is presented in Figure 113. It was surprising that very little cracking was observed in the dovetail region. There is only one significant crack, and it does match the DIC strain map nicely. However, it was thought that more cracks would have been observed. DIC strain maps indicated that there were multiple ILT cracks that formed. This suggests that some of the matrix cracks may have completely closed and are no longer visible after the load has been removed. Such behavior is common for SMI SiC/SiC CMCs.

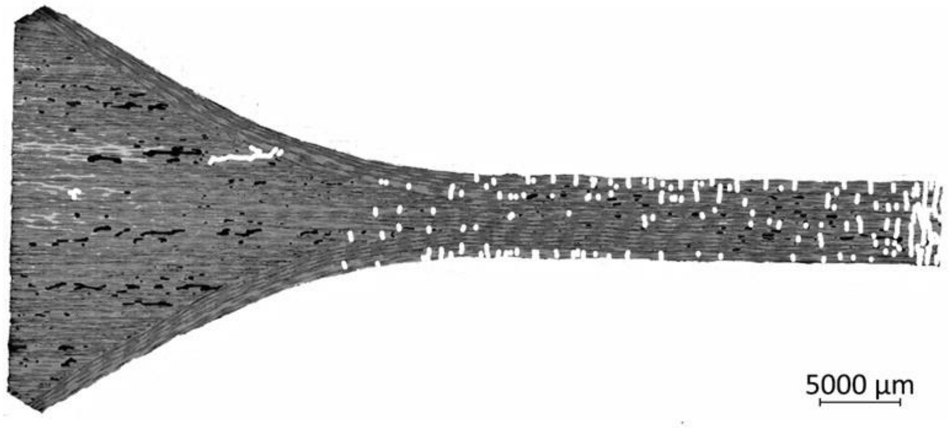

Figure 113. Micrograph of Polished Edge of Subelement 15-545a Fatigued at 23°C and 210 MPa, With Cracks Highlighted in White

5.2.6 Subelement Fatigue At 23°C & 200 MPa (15-548)

This specimen was to be a repeat test at 200 MPa with the goal of having the subelement failed in the dovetail section. Unfortunately, the subelement failed at 90,216 cycles in the straight sided stem section 82 mm down from the top of the specimen. This failure again highlighted the fine balance between initiating ILT damage and having failure occur in the stem.

5.2.7 Subelement Stepped Fatigue At 23°C (15-548a)

Failed subelement test specimen 15-548 was mounted with new tabs and placed back in the test frame. The goal was to continue fatigue testing with the goal of producing a failure in the dovetail. The subelement was fatigue tested as several stress level for 1000 cycles. If the specimen survived the 1000 cycles, the stress was increased and another 1000 cycles were applied. The subelement survived fatigue tested at 200 MPa, 210 MPa, and 220 MPa. However, the subelement failed once again in the stem section of the subelement during loading to 230 MPa. The failure was located slightly inside the MTS-647 wedge grips.

5.2.8 Subelement Fatigue At 23°C & 200 MPa (15-550)

This subelement test was to be a third test at 200 MPa with the goal of having the subelement fail in the dovetail. The subelement failed at 314,975 cycles. However, this specimen once again failed in the straight sided stem approximately 87 mm down from the top of the specimen. This failure once again highlighted the fine balance between initiating ILT damage and having failure occur in the stem. Only the stepped fatigue test failed in the dovetail. The four fatigue tests started at 200 MPa or higher all failed in the stem. These results are very encouraging as the results suggest that this particular airfoil design with high ILT stress levels in the dovetail, it is very unlikely to failure the subelement in the dovetail section.

5.2.9 Subelement Burner Rig At 800°C & 200 MPa (15-547)

This was the first burner rig test and the intent was to run at 200 MPa for 10,000 cycles. It was judged from the earlier stepped fatigue testing that damage would stabilize at this cycle count. Unfortunately, the subelement failed after only 1150 cycles and failed in the center of the hot zone area in the straight sided stem 133 mm down from the top. A failure in the straight sided region at such a low cycle count indicated that rapid embrittlement had occurred. Such rapid embrittlement mirrored that observed during the creep rupture test. This required significantly redesigning the burner rig test matrix. The test team made the decision to lower the test temperature to a temperature where oxidative degradation would occur at a much slower rate. A temperature of 600°C was selected, and the stress level was kept at 200 MPa.

5.2.10 Subelement Burner Rig At 600°C & 200 MPa (15-546)

For this test the temperature was lowered to 600°C and the stress was kept at 200 MPa. The cycle count limit was set at 10,000 cycles. The specimen failed in the dovetail section of the subelement at only 79 cycles. A photograph of the failed test specimen is shown in Figure 114. The specimen failed in the dovetail section between the outer plies and the interior wedge filler plies in a manor very similar to the earlier test specimens that failed. Figure 115 is an expanded view of where the failure occurred in the straight sided stem region. The specimen failed on the side that appears to have slightly more porosity in the stem as can be observed in the photograph. There appears to be a one ply in the stem that appears to have stringer type porosity, and this porosity is observed along the entire length of the subelement and is located a few plies deep from the surface. The specimen failed with the crack forming in the dovetail between the 10 outer plies and the wedge inserts. Failure was identical to the other subelements that failed in the dovetail region, so it was suspected that the porosity in the stem did not cause the early failure.

This was considered a successful test, and the result suggests that the thermal gradient stresses introduced by the burner rig significantly changed the stress state in the dovetail region of the subelement and contributed to an ILT induced fatigue failure. In contrast, four room temperature fatigue tests at 200-230 MPa all failed in the straight sided stem section of the subelement.

After failure, the dovetail was sectioned down the centerline as described earlier. One half was used to polish the edge of the specimen that had the DIC speckle patter on it as shown in Figure 116. The other half was used to polish the surface that was at the center of the test specimen as shown in Figure 117. This allowed for direct comparison of the cracking patter at the surface to the cracking patter in the middle of the dovetail. It was important to document if the cracks at the surface match the cracking pattern in the middle of the specimen. If they match, and if they agree with the DIC strain map, then it provides documentation that the DIC strain maps accurately capture cracking and damage development in the dovetail of the subelement.

In Figure 116 and Figure 117 all of the cracks that were visible at very high magnification are highlighted by thick red lines. For this specimen there are a substantial amount of long cracks that penetrate into the dovetail section and precisely align with the wedge plies that make up the dovetail. These cracks are in exactly the same location as those observed in the DIC strain maps for the other fatigue tested subelements. The cracks at the surface also match those in the center of the dovetail. There are clearly only cracks on one side of the specimen, and this also closely matches what was observed in previous DIC strain maps and previous micrographs of the failed stepped fatigue specimen (15-544).

Figure 114. Photograph Of Failed Subelement Stem And Dovetail For Burner Rig Tested at 600°C And 200 MPa (15-546)

Figure 115. Photograph Of Failed Subelement Burner Rig Tested at 600°C And 200 MPa (15-546)

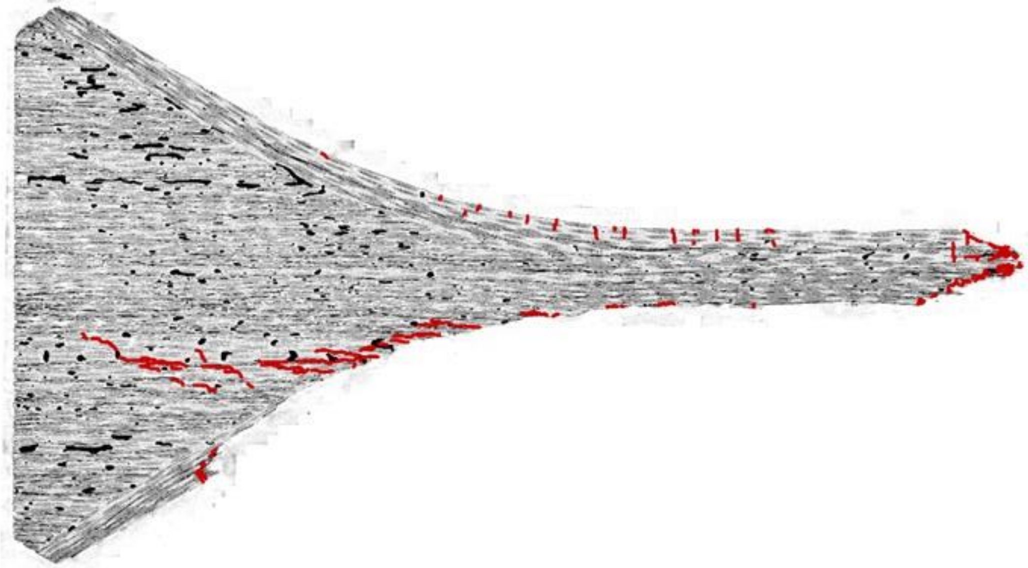

Figure 116. Micrograph of Polished Surface Edge Micrograph Of Subelement Burner Rig Tested at 600°C And 200 MPa (15-546)

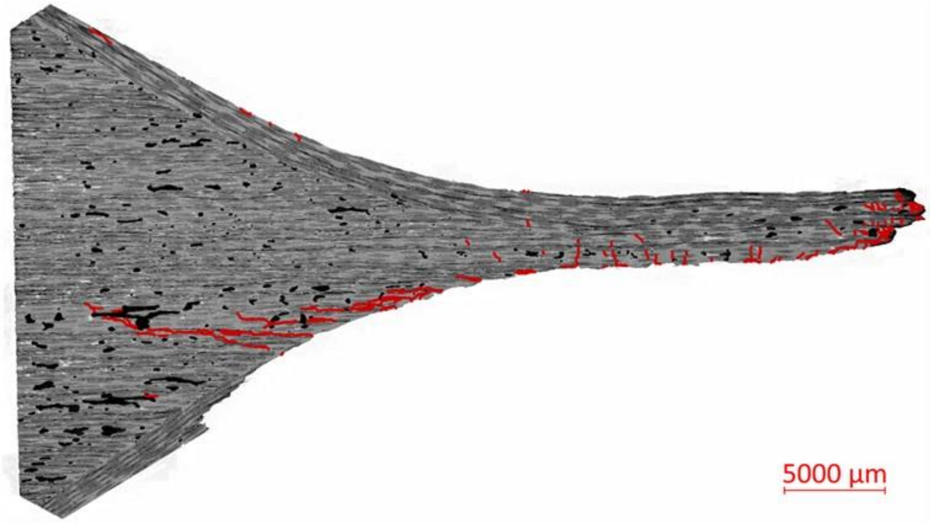

Figure 117. Micrograph Of Polished Center Section Of Subelement Burner Rig Tested at 600°C And 200 MPa (15-546)

5.2.11 Subelement Burner Rig At 600°C & 175 MPa (15-549)

With the burner rig test conducted at 600°C and 200 MPa failing in only 79 cycles, the team decided to run a second test at 600°C and reduce the stress to 175 MPa in order to allow for more cycles with the goal of not failing the test specimen. The cycle limit was set for 1000 cycles with the hope that the specimen would not fail in the stem from oxidative degradation. The specimen survived the 1000 fatigue cycles in the burner rig, and taken back to the servo-hydraulic testing laboratory for further testing.

The subelement was mounted in a servo-hydraulic test frame and one load and unload cycle at room temperature was applied using a maximum stress of 175 MPa. Prior to loading, a speckle pattern was applied to the subelement edge so that DIC images could be recorded. A clip-on extensometer was mounted to the edge of the specimen in the straight sided stem region and recorded displacement/strain. The subelement survived the one load cycle to 175 MPa and remained in one piece.

The DIC data was analyzed and strain maps were generate for stress levels during loading to 175 MPa. The stress levels were 75 MPa, 100 MPa, 125 MPa, 150 MPa, and 175 MPa. The stress versus strain was plotted for the load and unload cycle. Figure 118 compares the load and unload stress-strain trace along with the DIC strain map for an applied stress of 75 MPa. The strain map shows no sign of any cracking in the dovetail. Figure 119 shows the same trace with the DIC strain map at 100 MPa. Again no sign of any cracking in dovetail. Figure 120 shows the same trace and the DIC strain map at a stress of 125 MPa, while Figure 121 shows the same figures for a stress of 150 MPa. Neither DIC image shows any indication of any cracks forming in the dovetail. The last DIC strain map was generated at a stress of 175 MPa and is presented in Figure 122. Even at this stress level there is no indication of any cracks in the dovetail region. It is not surprising that no cracks were observed by the DIC. The room temperature tension test reached an applied stress value of 210 MPa before there was any noticeable damage from the DIC images. It is suggested that the burner rig temperature of 600°C was too low to alter the stress state in the subelement dovetail region. Therefore, the specimen exhibited behavior similar to room temperature tests.

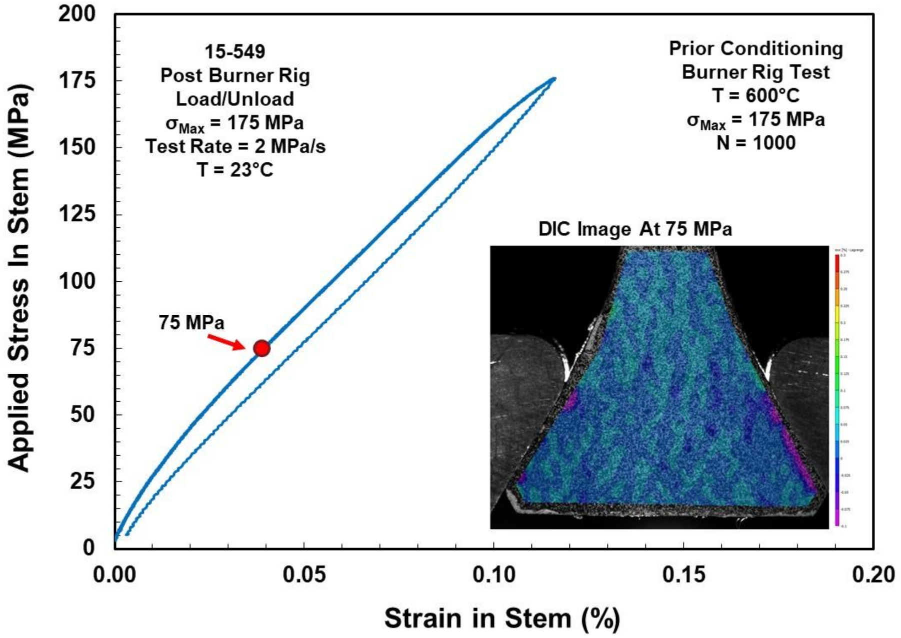

Figure 118. Stress-Strain Trace And DIC Strain Map For Prior Exposed Burner Rig Exposed Subelement At A Stress of 75 MPa (15-549)

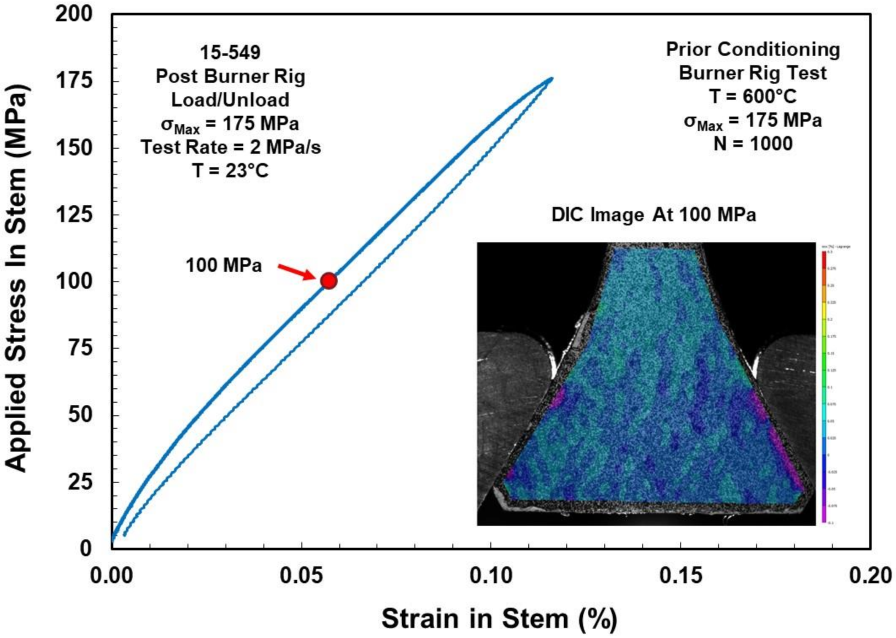

Figure 119. Stress-Strain Trace And DIC Strain Map For Prior Exposed Burner Rig Exposed Subelement At A Stress of 100 MPa (15-549)

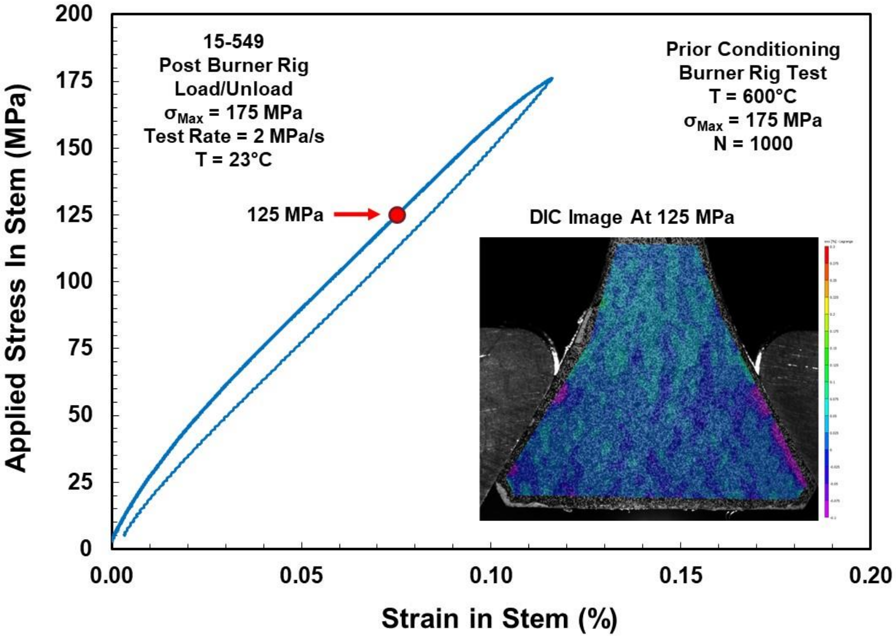

Figure 120. Stress-Strain Trace And DIC Strain Map For Prior Exposed Burner Rig Exposed Subelement At A Stress of 125 MPa (15-549)

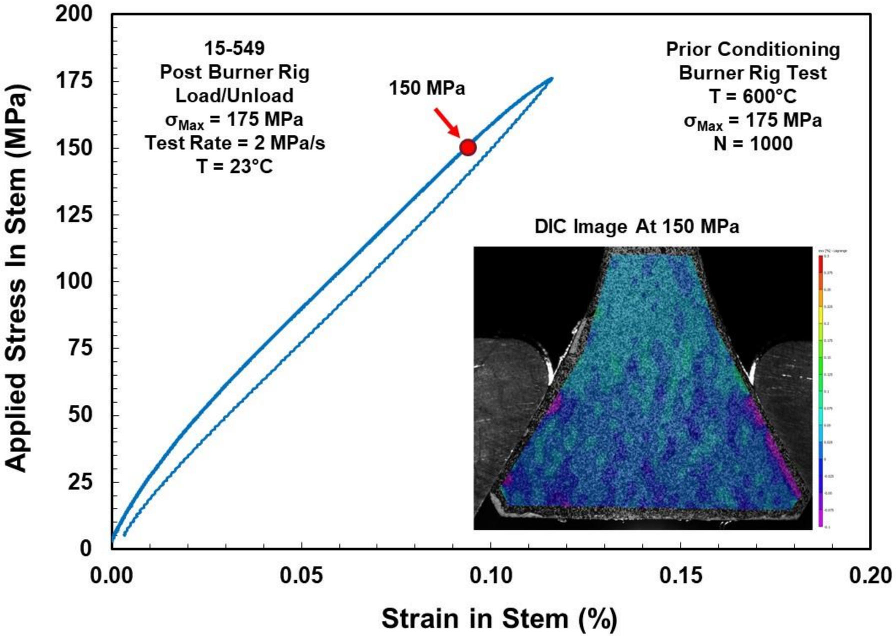

Figure 121. Stress-Strain Trace And DIC Strain Map For Prior Exposed Burner Rig Exposed Subelement At A Stress of 75 MPa (15-549)

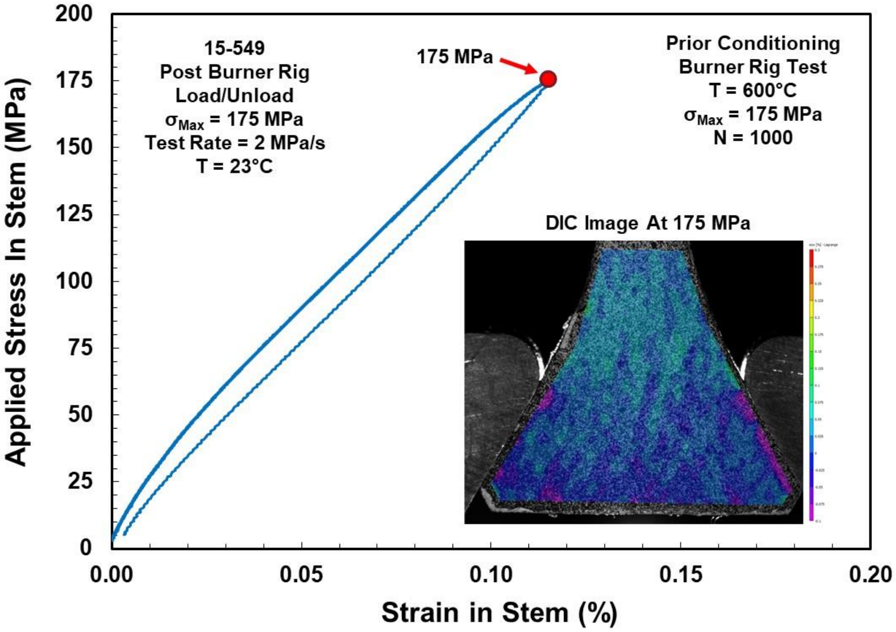

Figure 122. Stress-Strain Trace And DIC Strain Map For Prior Exposed Burner Rig Exposed Subelement At A Stress of 175 MPa (15-549)

5.2.12 Subelement Burner Rig At 1000°C & 175 MPa (15-541)

After the successful burn rig test at 600°C and 175 MPa for 1000 cycles, it was decided to run a final test using the last subelement at a much higher temperature of 1000°C. The objective was to determine if a substantially higher temperature would influence the amount of ILT cracking compared to the lower temperature of 600°C. The stress was kept at 175 MPa and the test team decided to run only one load and unload cycle. It was estimated that the subelement would not fail on only one cycle. Only one loading cycle was selected because previous creep rupture tests on flat dogbone test specimens and burner rig fatigue experiments on the subelements indicated that rapid embrittlement occurs in this CMC at temperatures of 800°C and above.

The specimen survived the one loading and unloading cycle to 175 MPa at 1000°C. After allowing the specimen to cool, it was taken back to the servo-hydraulic testing laboratory for further study. The subelement was placed in the servo-hydraulic test frame and was loaded and unloaded to 175 MPa while being monitored with DIC. After loading the specimen remained in one piece.

The resulting stress-strain data was plotted up, and DIC strain maps were generated at 75, 100, 125, 150, and 175 MPa. Figure 123 presents the stress-strain trace and the DIC strain map at 75 MPa. There is no indication of any cracking in the dovetail section of the subelement. The DIC stain map at a stress of 100 MPa is compared to the stress-strain trace in Figure 124 and again there is only a slight indication that cracking may have started. However, Figure 125 presents the strain map at 125 MPa and one can clearly see evidence of damage on the right side of the dovetail section indicating that significant cracking in the dovetail has occurred. Figure 126 presents the DIC strain map at 150 MPa while Figure 127 presents the DIC strain map at 175 MPa. At 175 MPa it is clear that a significant crack and several secondary cracks have developed in the dovetail creating a significantly large damage zone.

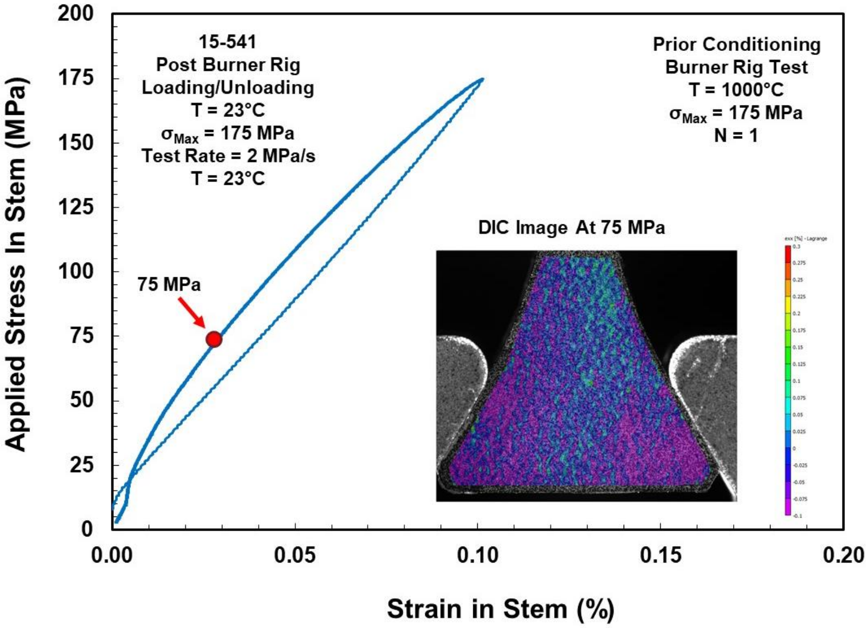

Figure 123. Stress-Strain Trace And DIC Strain Map For Prior Exposed Burner Rig Exposed Subelement At A Stress of 75 MPa (15-541)

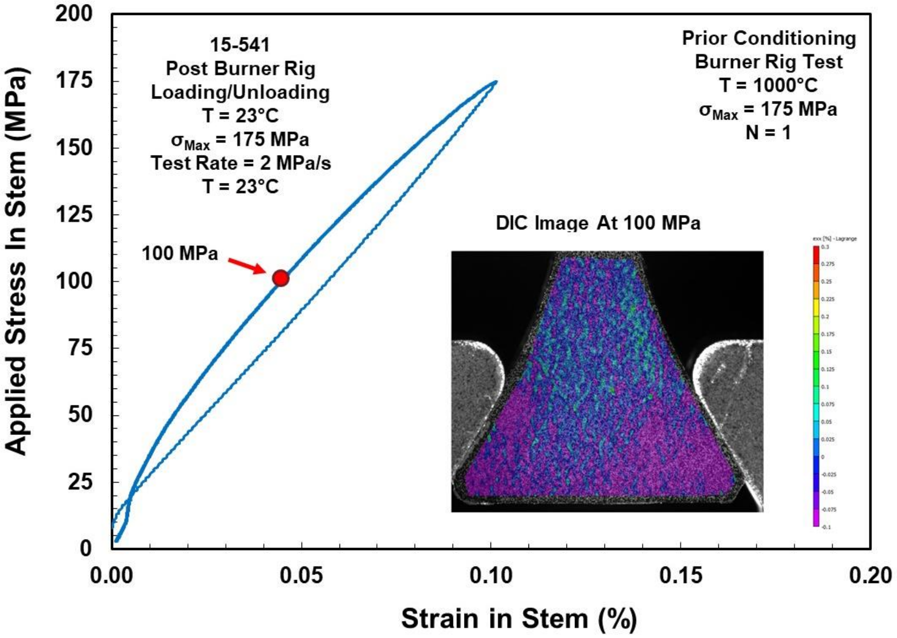

Figure 124. Stress-Strain Trace And DIC Strain Map For Prior Exposed Burner Rig Exposed Subelement At A Stress of 100 MPa (15-541)

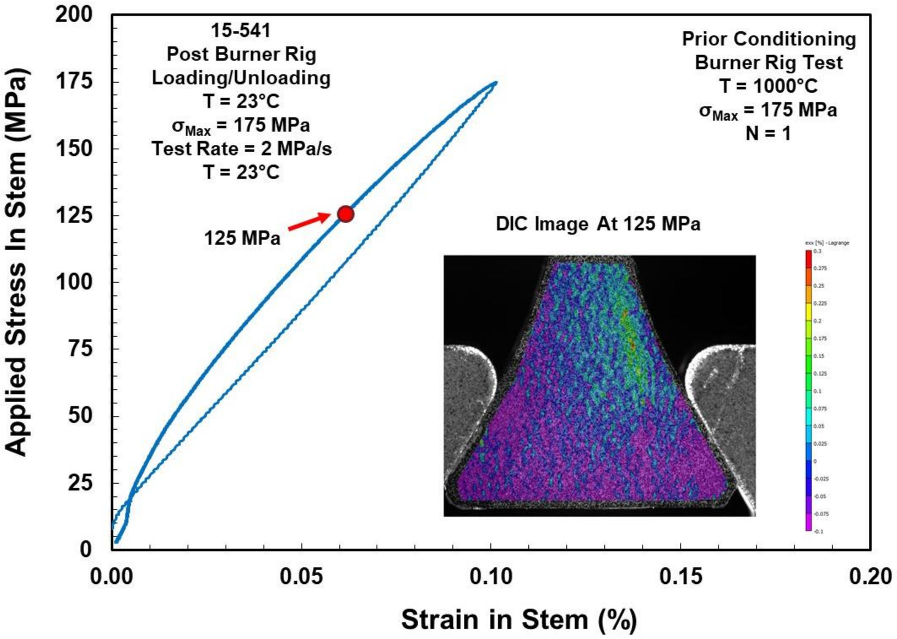

Figure 125. Stress-Strain Trace And DIC Strain Map For Prior Exposed Burner Rig Exposed Subelement At A Stress of 125 MPa (15-541)

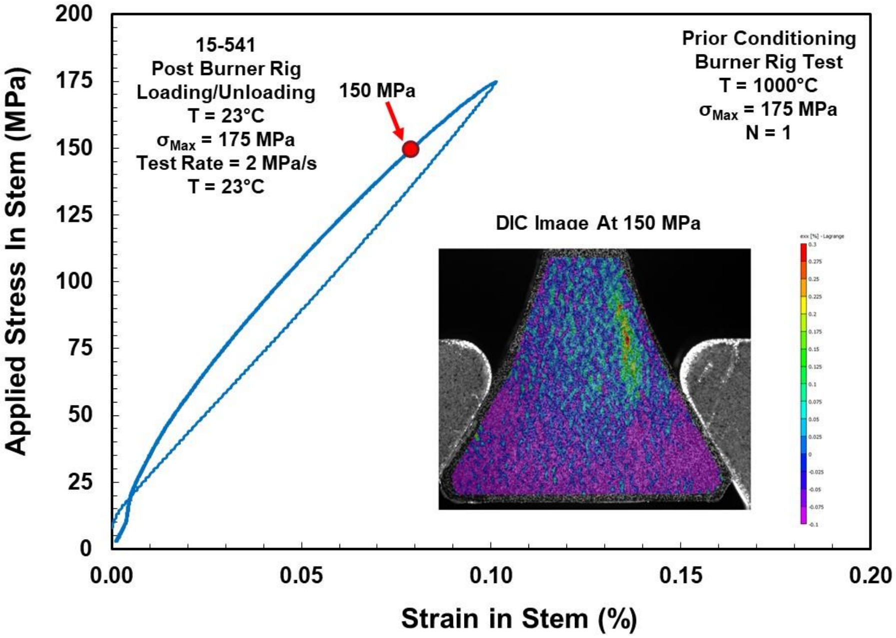

Figure 126. Stress-Strain Trace And DIC Strain Map For Prior Exposed Burner Rig Exposed Subelement At A Stress of 150 MPa (15-541)

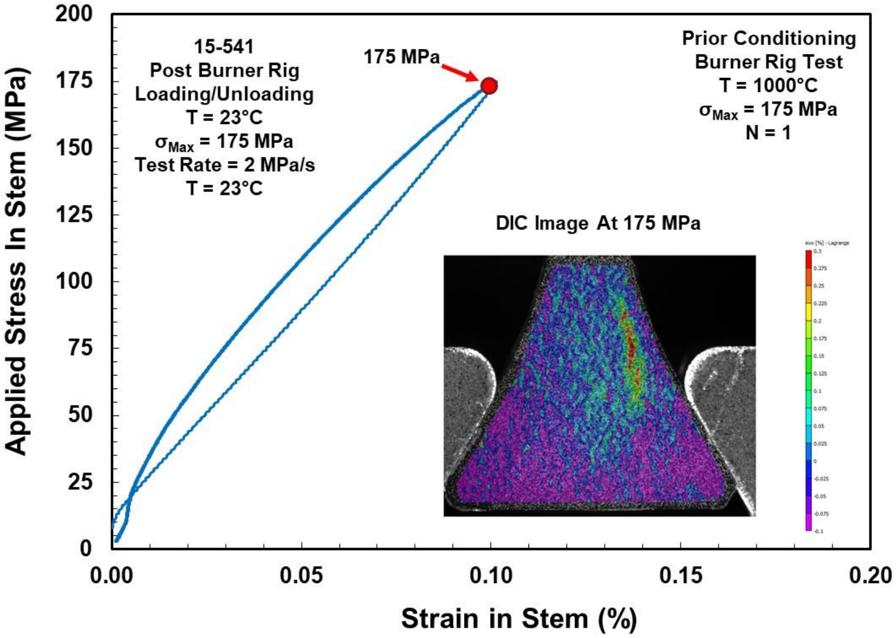

Figure 127. Stress-Strain Trace And DIC Strain Map For Prior Exposed Burner Rig Exposed Subelement At A Stress of 175 MPa (15-541)

The team was able to analyze the DIC strain maps and calculate a length to the damage zone. As shown earlier, the damage zone indicated in the DIC strain maps is comprised of many matrix cracks. It has already been documented that the damage always originates at the interface of the outer sub-laminate and the insert. The burner rig specimen did not definitively show damage until the applied stress was between 100 MPa and 125 MPa. In comparison, the room temperature tension test reached 210 MPa before there was any noticeable damage. The team was able to study all of the DIC strain maps and calculate a damage zone length versus applied stress. This was also done for the tension test that was conducted at room temperature (15-543). The data is presented in Figure 128. The burner rig exposed specimen exhibited a damage length of ~7 mm at 175 MPa, whereas the corresponding room temperature tension test specimen had to be loaded to 230 MPa before exhibiting the same damage length.

After the load and unload, the subelement was sectioned and the DIC side of the dovetail section was mounted and polished. A micrograph of the polished subelement is shown in Figure 129. No cracks could be observed in the image, indicating they had all closed up. This indicates that there is significant residual stress in the dovetail section of the subelement and that cracks did not remain open and could not be detected as they could in failed test specimens.

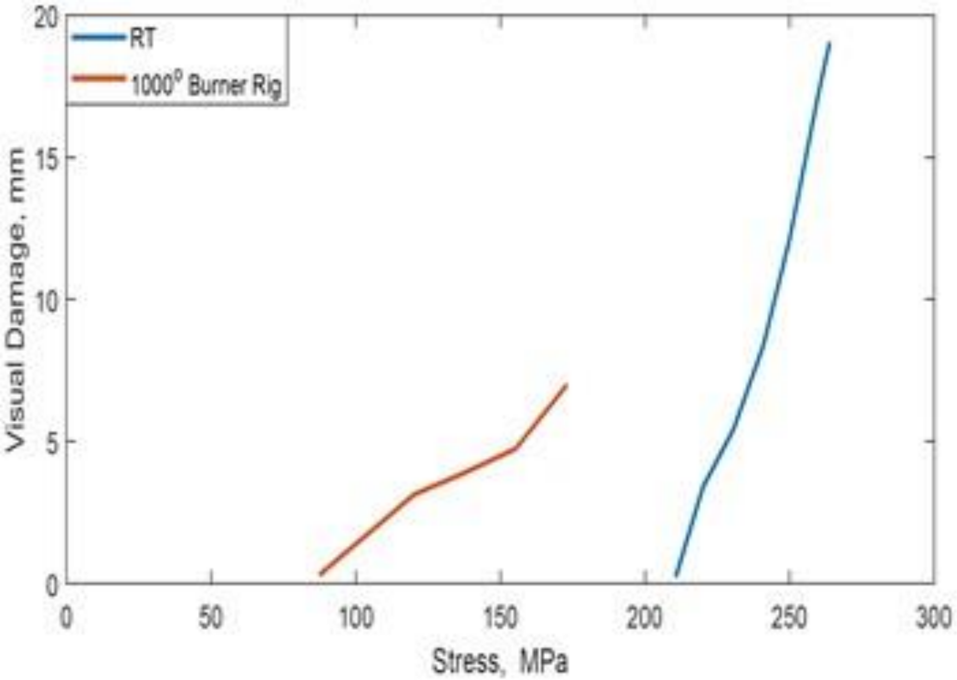

Figure 128. Comparison Of Damage Length In Dovetail Versus Applied Stress For The 23°C Tension Test And The Burn Rig Loaded To 175 MPa At 1000°C.

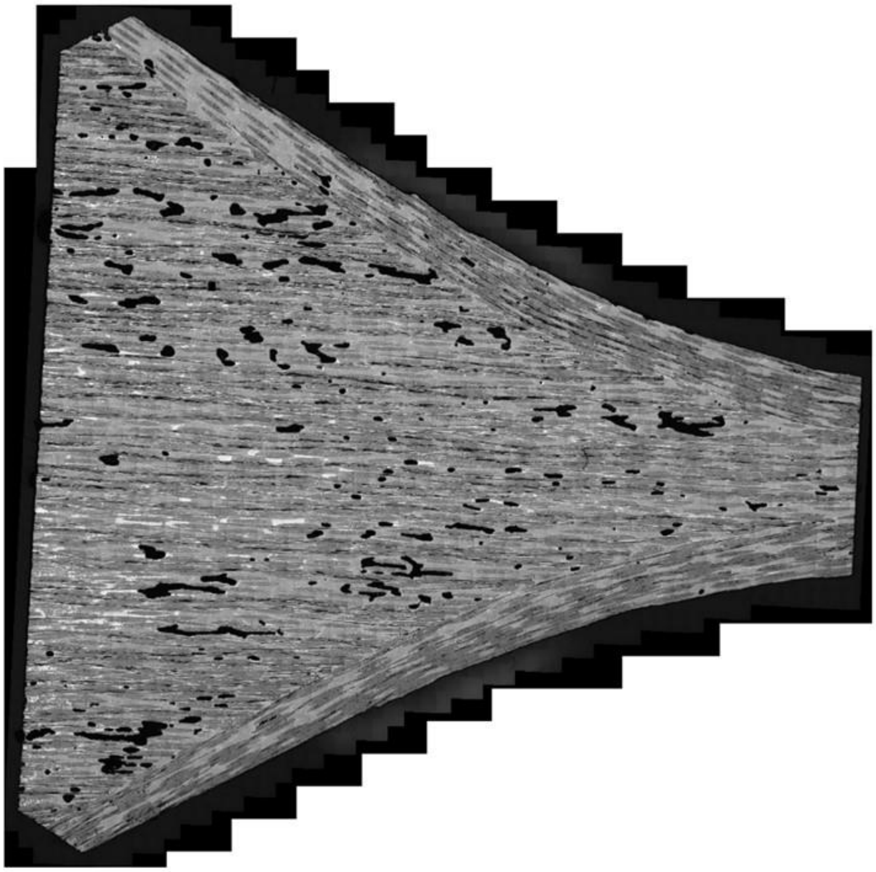

Figure 129. Polished Cross-Section of Burner Rig Specimen Tested At 1000°C and 175 MPa For One Cycle (15-541)

6.0 CONCLUSIONS AND OBSERVATIONS

Advanced materials characterization methods were employed on a slurry melt-infiltrated SiC/SiC CMC. The objective of this study was to evaluate how damage develops in simulated airfoil shaped subelements. The test specimen was carefully designed using FEA to maximize ILT stresses in the dovetails section of the subelement.

Baseline material property characterization was conducted to generate input for model calibration. Double notch compression tests yielded interlaminar shear strengths between 60-75 MPa. Interlaminar tension tests on flat round button test specimens produced strengths of 18 and 21 MPa. For tension tests at 23°C and 800°C, the effect of temperature seems to increase the strength, PL, and strain resistance. A single creep test at 1200°C under 175 MPa stress showed roughly 0.22% strain after 30 to 40 minutes. The creep test also revealed that this CMC system experienced rapid oxidative embrittlement and therefore failed after exhibiting limited creep strain.

For subelement testing, loading consisted of monotonic tension, stepped tension, stepped fatigue, and fatigue loading. Room-temperature in-situ monitoring experiments utilized extensometry, digital image correlation, and acoustic emission to monitor damage evolution during testing. The effect of thermal gradients on damage initiation was also explored using a burner rig. The use of DIC proved to be extremely useful in documenting damage evolution in the dovetail section of the subelement. This was especially true for the various types of tests conducted.

Observation of matrix cracks using high resolution microscopy proved difficult at best because of the residual stress state in the CMC. This residual stress state caused the cracks formed during loading to completely close once load was removed, making detection of those cracks hard to identify. Microscopy on specimens that did not fail exhibited very few cracks while there was substantial deformation observed on the DIC strain maps at maximum load. However, the damage in the DIC strain maps would decrease and disappear as the applied load was removed. Microscopy of failed specimens exhibited similar cracks to those observed on the DIC strain map images. It appears that at failure some of the existing crack remain open and do not fully close.

Tension Test Of Subelement

Tension testing of the subelement proved to be very informative. DIC images were recorded throughout the entire tension test. DIC strain maps indicated that cracks were observed in the dovetail section of the subelement until the applied stress reached 220 MPa. This was a bit surprising as the FEA analysis identified that the ILT stress is in the dovetail would exceed the measured ILT strength of 19.6 MPa once the applied tensile stress exceeded 90 MPa. This difference may simply be dependent on the resolution of the DIC, but more work in the form of interrupting tests and performing detailed high resolution microscopy would be required to quantify at exactly what stress level ILT cracks first initiate.

The team was able to document that the first cracks appeared precisely where FEA had predicted. As the stress level increased the existing cracks grew and new cracks formed creating an extended damage zone. Just before failure at 263 MPa, one could observe four distinct cracks. These cracks then linked up resulting in failure of the test specimen. It is very important to point out that the crack pattern from the sectioning and microscopy work closely match what was observed from the DIC strain map data. It is also important to note that detailed microscopy revealed that all observable cracks are on one side of the specimen, and there were not matrix cracks on the other side. This was a surprising result and may indicate that once the ILT cracks initiate, there is a shift in the stress state. Much more work would be required to understand this observed cracking.

Stepped Tensile Of Subelement

A tensile load-unload test with sequentially increasing stress revealed that once cracking occurs it did not continue until the previous maximum stress was exceeded or an unstable damage condition was reached. This type of test was very useful in tracking permanent damage in the subelement. For a stress of 250 MPa there were multiple cracks in the DIC image, however upon unloading and reloading, there were no cracks observed at 110 MPa. This clearly documents that the cracks often close back up and do not reopen until a specific stress level in reached. It was only after reaching160 MPa that the cracks are again visible by DIC.

Stepped Fatigue Of Subelement

This testing provided very important information about the development of damage and damage propagation during fatigue of the subelement. ILT cracks were not observed until the fatigue stress level was increased to 200 MPa. However, this initial damage was stable with continued cycling at 200 MPa. It was only at an applied stress level of 225 MPa that the ILT crack exhibited grow, and multiple ILT cracks formed. The identification of the ILT cracks using DIC was backed up using detailed high resolution microscopy. Detailed FEA analysis indicated that ILT cracks would be the predominant damage mechanism. However, FEA predicted ILT cracks to occur at approximately 90 MPa, but they were not observed until 200 MPa. Much work remains to be performed to understand this difference.

Fatigue Of Subelement

All four room temperature fatigue tests failed in the straight sided stem section of the subelement. However, the fatigue loading did provide useful information. The testing highlighted that the majority of damage occurred within the first few fatigue cycles. DIC and AE confirmed this finding with full-field strain measurement and cumulative crack events, respectively.

Extensive microscopy was performed on failed test specimen. The bottom portion of the failed specimen, which included the dovetail region, was mounted and polished to identify matrix cracks. It is surprising that very little cracking was observed in the dovetail region. There was only one significant crack, and it did match the DIC strain map exactly. However, it was thought that more cracks should have been observed, as the DIC strain maps suggest that multiple ILT cracks have formed. This suggests that some of the matrix cracks may have completely closed and are no longer visible after the load has been removed.

The four fatigue tests started at 200 MPa or higher all failed in the stem. These results are very encouraging as the results suggest that this particular airfoil design with high ILT stress levels in the dovetail, it is very unlikely to failure the subelement in the dovetail section.

Burner Rig Of Subelement

Burner rig fatigue testing proved to be very valuable. A total of four standard fatigue tests at 23°C and 200 MPa all ended up with failures in the straight sided stem section of the subelement. However, burner rig fatigue testing at 600°C and 200 MPa resulted in failure in the dovetail attachment region. This strongly suggests that the thermal gradient induced stresses influence failure. However, resources did not allow for a detailed thermos-mechanical analysis of the subelement.

Burner rig fatigue testing was hampered by rapid oxidation and embrittlement of the SMI SiC/SiC CMC. This limited the number of fatigue cycles that could be applied to the test specimen and also limited the maximum stress level that could be studied in fatigue.

For the burner rig tested subelement at 600°C and then loaded at 23°C in the servo-hydraulic lab with DIC exhibited a unique finding in that the first indication of damage during loading at 23°C appeared around 100-125 MPa. For comparison, the room temperature subelement tension test reached an applied stress value of 210 MPa before there was any noticeable damage from the DIC images. For subelements fatigue tested at 23°C, evidence of damage in the dovetail section of the subelement was only observed after the applied stress level has been increased to 200 MPa.

General Observations From This Study

Cracks located in the dovetail section of failed subelement test specimens align with the wedge plies that make up the dovetail an also occur between the 10 outer continuous plies and the wedge inserts. These cracks are in exactly the same location as those observed in the DIC strain maps for the subelement test specimens.

It is clear that the cracks observed in the DIC strain map images linked up and failed the specimen. These cracks traveled along the interface between the ten outer continuous plies and the wedge inserts. Once the expanding crack reached the straight sided stem section of the subelement the test specimen failed across the remaining portion of the stem. The bottom end of the crack always appears to be dominated by shear and the crack penetrates through the 10 outer plies well before reaching the end of the specimen. So the architecture of the test specimen in the dovetail region definitely contributes to the progression of damage and the ultimate failure mechanism.

Cracks observed on the surface of the specimen using DIC also appeared at the center of the specimen. This documents that DIC is a powerful tool for studying failure behavior in these types of subelements, as the damage observed occurs uniformly throughout the thickness of the subelement dovetail section.

For all testing, cracks in the dovetail only appeared on one side of the test specimen, and this was documented with DIC strain field maps as well as high resolution microscopy. Not once did cracks or damage zones appear on both sides of the subelement

The room temperature fatigue limit in this SMI SiC/SiC CMC was approximately 210-225 MPa, as determined from failures of the straight sided stem section of the subelement test specimens.

The primary damage mechanism is the formation cracks in the dovetail that are driven by high interlaminar stresses, and that multiple cracks form and link up resulting in failure.

This work showed good correlation between FEA model predictions of the damage initiation location due to interlaminar stresses and actual locations of observed damage. However, FEA predicted cracking to initiate at 90 MPa, and cracks were not observed using DIC Strain Field Mapping until the applied stress was increased to approximately 200 MPa.

ILT cracks appeared at approximately 200 MPa. These cracks popped in and were relatively stable for testing from cycle 60,000 up to 300,000 cycles. It was only at the highest stress of 225 MPa that crack propagation and coalescence of multiple cracks was observed.

Surface damage detected by DIC was shown to precisely match sub-surface (0.25”) damage, and this was documented using high resolution microscopy.

Only the stepped fatigue test failed in the dovetail. The four fatigue tests started at 200 MPa or higher all failed in the stem. These results are very encouraging as it is very unlikely to failure the subelement in the dovetail section.

Burner rig testing had a significant impact on the damage state of the subelement. Subelement test specimens that were loaded in the burner rig and then tested at room temperature using DIC exhibited cracking in the dovetail section at lower stress levels those subelement test specimens that were only tested at room temperature. This may be a result of relaxation of the residual stress state in the dovetail region. However, much more work would need to be performed to fully understand this observation.

7.0 REFERENCES

1. https://www.ge.com/news/reports/space-age-cmcs-aviations-new-cup-of-tea\
2. https://www.ge.com/news/reports/hotter-air-ceramics-are-the-secret-to-lighter-faster-jet-engines, 2020
3. Nakamura, T., Oka, T., Imanari, K., Shinohara, K., Ishizaki M., Development of CMC Turbine Parts for Aero Engines, IHI Engineering Review, Vol . 47 No. 1, 2014,
4. T. Tamura, T. Nakamura, K. Takahashi, T. Araki and T. Natsumura, “Research of CMC Application to Turbine Components,” IHI Engineering Review, Vol. 38 No. 2 (2005) pp. 58-62
5. Kumar, R., Srinivasan, G., Rugg, K., Yuan, Z., and Fish, J., “Progress On Damage and Delamination Modeling in SiC/SiC Ceramic matrix Composites,” Presented at 39th annual Conference on Composites, Materials, and Structures, Cocao Beach/Cape Canaveral, Florida, January 26-29, 2015.
6. Engle, T., “Ceramic matrix Composite Low Pressure Turbine Blade Development, SBIR Phase II Program, Contract No. FA8650-11-C-2109, 2011.
7. Kim, T., Mall, S, and Zawada, L.P., Fatigue Behavior of Hi-Nicalon Type-S™/BN/SiC Ceramic Matrix Composites in a Combustion Environment, International Journal of Applied Ceramic Technology 8.2 (2011): 261-72.
8. Kim, T. T., Mall, S., Zawada, L. P., and Jefferson, G., Simultaneous Fatigue and Combustion Exposure of a SiC/SiC Ceramic Matrix Composite, Journal of Composite Materials 44.25 (2010): 2991-3016
9. Tracy J, Daly S, Sevener K. Multiscale damage characterization in continuous fiber ceramic matrix composites using digital image correlation. J Material Science, 2015, 50, pp 5286–99.
10. Rajan VP, Rossol M, Zok F.W., Optimization of Digital Image Correlation for high-resolution strain mapping of ceramic composites. Environmental Mechanics, 2012, 52, pp. 1407–21
11. Novak, M.D. and Zok, F.W., High-temperature materials testing with full-field strain measurement: Experimental design and practice. Review of Scientific Instruments, 2011, 82(11), pp. 115101
12. Whitlow, T., E. Jones, and C. Przybyla, In-situ damage monitoring of a SiC/SiC ceramic matrix composite using acoustic emission and digital image correlation. Composite Structures, 2016, 158, pp. 245-251.
13. Maillet, E. and Morscher, G., Waveform-based selection of acoustic emission events generated by damage in composite materials. Mechanical Systems and Signal Processing, 2015. 52-53: p. 217-227
14. Choi, S. and Bansal, N., Interlaminar Tension/Shear Properties and Stress Rupture In Shear Of Various Continuous Fiber-Reinforced Ceramic Matrix Composites, Ceramic Transactions, Volume 175, pp. 119-134, 2006

LIST OF SYMBOLS, ABBREVIATIONS, AND ACRONYMS

AE	Acoustic Emission
AFIT	Air Force Institute Of Technology
AFRL	Air Force Research Laboratory
ASTM	American Society For Testing And Materials
CMC	Ceramic Matrix Composite
CT	Computed Tomography
DIC	Digital Image Correlation
FEA	Finite Element Analysis
FLIR	Forward Looking Infrared
FVF	Fiber Volume Fraction
HVOF	High Velocity Oxygen Fuel
ICMSE	Integrated Computational Materials Science and Engineering
ILT	Interlaminar Tension
ILS	Interlaminar Shear
μCT	Micro-Computed Tomography
RXCC	Materials and Manufacturing Directorate Composites Branch
RXCCP	Materials and Manufacturing Directorate Composites Performance Research Team
RX	Materials and Manufacturing Directorate System Support Division
SE	Scanning Electron Microscope
SMI	Silicon Melt-Infiltrated
UDRI	University of Dayton Research Institute
USAF	United States Air Force
UTS	Ultimate Tensile Strength